

THESIS
2
2006



This is to certify that the
thesis entitled

**PISTON DESIGN AND ANALYSIS: PARAMETERIZED AND
COMPLETE FINITE ELEMENT ANALYSIS APPROACH FOR
THE ASSESSMENT OF PISTON PERFORMANCE**

presented by

ANDREAS PETROU PANAYI

has been accepted towards fulfillment
of the requirements for the

 M.S. degree in Mechanical Engineering

 Harold J. Schrock
Major Professor's Signature

 April 26, 2006
Date

PLACE IN RETURN BOX to remove this checkout from your record.
TO AVOID FINES return on or before date due.
MAY BE RECALLED with earlier due date if requested.

| DATE DUE | DATE DUE | DATE DUE |
|-----------------|-----------------|-----------------|
| | | |
| | | |
| | | |
| | | |
| | | |
| | | |
| | | |
| | | |
| | | |
| | | |
| | | |

**PISTON DESIGN AND ANALYSIS: PARAMETERIZED AND
COMPLETE FINITE ELEMENT ANALYSIS APPROACH FOR THE
ASSESSMENT OF PISTON PERFORMANCE**

By

Andreas Petrou Panayi

A THESIS

**Submitted to
Michigan State University
in partial fulfillment of the requirements
for the degree of**

MASTER OF SCIENCE

Department of Mechanical Engineering

2006

ABSTRACT

PISTON DESIGN AND ANALYSIS: PARAMETERIZED AND COMPLETE FINITE ELEMENT ANALYSIS APPROACH FOR THE ASSESSMENT OF PISTON PERFORMANCE

By

Andreas Petrou Panayi

Modeling the thermal and mechanical behavior of a piston is crucial, as it allows for the prediction of piston characteristics such as dynamics and friction. These characteristics directly affect the efficiency of an internal combustion engine. In this thesis, two studies are conducted; an evaluation of the parameterized piston modeling method and a development of a finite element program for a full piston model analysis.

For the first study, a parameterized piston model is generated using a set of selected geometrical parameters from the production piston model according to the standard of CASE, a cylinder-kit simulation software. A finite element analysis is conducted for both the parameterized piston model and the production piston model using the software COSMOSDesignSTAR. A comparison of the two models shows good agreement in both thermal and mechanical characteristics. CASE is used to demonstrate the advantages of the parameterized model in the assessment of piston performance.

For the second study, a piston finite element analysis program is developed. The capabilities of the program are demonstrated using a full piston CAD model. The meshed geometry of the CAD model is imported and an analysis is performed over a full four-stroke cycle. The piston's elastic behavior under thermal and mechanical loads is verified with COSMOSDesignSTAR and the elastohydrodynamic lubrication analysis results show that this model is capable of predicting the piston behavior and performance.

**Copyright by
ANDREAS PETROU PANAYI
2006**

to my parents...
and to my Darioulla...

ACKNOWLEDGEMENTS

First I would like to give sincere thanks to my advisor, Dr. Harold J. Schock, for giving me the opportunity to work with him, first as his teaching assistant and then as his research assistant at the Automotive Research Experiment Station here at Michigan State University. I would also like to extend my thanks to him for his guidance and faith in me through my studies and my research.

Special thanks go to Dr. Andre Benard and Dr. Ronald Averill, the members of my guidance committee. They both provided me with valuable information on finite element methods, thus strengthening my understanding of the methods and consequently enabling me to develop the piston finite element analysis program. I would like to thank Dr. Giles Brereton as well for providing me with invaluable literature references and for discussing and suggesting solutions to problems I was encountering with numerical modeling.

I would also like to express my gratitude to Dr. Boon-Keat Chui of Mid Michigan Research, first for encouraging me to have my first publication and second for all his guidance in understanding the piston modeling techniques and CASE.

Dr. Mikhail Ejakov of Ford Motor Company deserves special recognition for providing me with the piston solid models, as well as for his willingness to discuss the development of the piston finite element analysis program.

I would like to thank Andrew Fedewa of Mid Michigan Research for sharing his experiences with CASE and piston modeling and for providing me with the experimental

oil film thickness measurements. Also I thank Mulyanto Poort of Mid Michigan Research for his invaluable programming tips and advice.

Special recognition goes to the people of the Automotive Research Experiment Station: Dr. Murad Ismailov, Ed Timm, Tom Stuecken, Josh Bedford, Jia Ma, Kim Sarbo and Melissa Jopke for making it a fun workplace.

Also I would like to thank my dear friend Chandra Romel for sharing our thesis experiences and racing with me against time.

Finally I would like to thank and express my gratitude to my parents, Petros and Panayiota, and to my Darioulla, for their love, support and patience, even when I am so far and away.

PREFACE

Computer simulations are becoming more popular by the day as advances in electronics decrease computation time. One of the most widely used computational methods in engineering now is finite element methods. By now this method is well understood, and because of its robustness it allows for the solution of complex as well as nonlinear systems. This thesis presents the finite element method as applied to the analysis of a piston model. Commercial software is utilized, as well as a piston finite element analysis code developed by the author.

The thesis starts by introducing the basics of finite element methods. The Finite Element Theory chapter explains the methods used within this work. The aim of this chapter is to develop an understanding of the theories upon which finite element codes are built, thus enabling a confidence in using them. The author assumes the reader has some previous knowledge in calculus, linear algebra, solid mechanics, heat transfer and fluid mechanics as well as in numerical methods. The theories do not go in depth; thus, with the assumed knowledge mentioned above, they can be very easily understood.

Also this thesis introduces the use of commercial software, which is a very important tool for the engineer of today. A parameterized modeling method is presented which significantly speeds up simulations. A finite element analysis of a parameterized piston model as well as of a full piston model is conducted with COSMOSDesignSTAR. A cyclic analysis is performed in CASE.

Furthermore the thesis shows how a custom finite element code can be developed to meet specific needs. The last chapter clearly explains the steps required in the

development of a piston finite element analysis code. Although the code itself is not provided, detailed flowcharts are shown.

The images in this thesis are presented in color.

TABLE OF CONTENTS

| | |
|---|--------------|
| LIST OF TABLES | xi |
| LIST OF FIGURES | xii |
| KEY TO SYMBOLS AND ABBREVIATIONS | xviii |
| CHAPTER 1 INTRODUCTION | 1 |
| 1.1 Motivation..... | 1 |
| 1.2 Previous Efforts in Piston Modeling..... | 2 |
| 1.3 Objective | 4 |
| CHAPTER 2 THE FINITE ELEMENT METHOD | 6 |
| 2.1 Introduction..... | 6 |
| 2.2 Approximate Solutions | 8 |
| 2.2.1 Galerkin’s Method | 8 |
| 2.2.2 Variational Method | 9 |
| 2.3 Elements and their Shape Functions | 9 |
| 2.3.1 Linear Triangular Element..... | 9 |
| 2.3.2 Linear Tetrahedral Element | 14 |
| 2.4 Finite Element Formulation | 21 |
| 2.4.1 Heat Equation..... | 21 |
| 2.4.2 Static Analysis | 26 |
| 2.4.3 Reynolds Lubrication Equation | 37 |
| 2.4.4 Incorporation of Boundary Conditions | 43 |
| 2.4.5 Guyan Reduction | 44 |
| 2.4.6 Conjugate Gradient Method..... | 46 |
| CHAPTER 3 ENGINE OPERATING PARAMETERS | 50 |
| 3.1 Introduction..... | 50 |
| 3.2 Time Step..... | 51 |
| 3.3 Angular Speed..... | 51 |
| 3.4 Piston Motion..... | 51 |
| 3.4.1 Sample results | 55 |
| CHAPTER 4 PARAMETERIZATION AND FEA APPROACH FOR THE ASSESSMENT OF PISTON CHARACTERISTICS | 58 |
| 4.1 Introduction..... | 58 |
| 4.2 Piston model FE analysis | 59 |

| | |
|---|------------|
| 4.2.1 Thermal Loading..... | 61 |
| 4.2.2 Thermal Loading Deformation | 68 |
| 4.2.3 Mechanical Loading..... | 70 |
| 4.2.4 Combined Thermal and Mechanical Loading..... | 71 |
| 4.2.5 Computation Time | 80 |
| 4.3 CASE Analysis | 81 |
| 4.3.1 Finite Element Analysis..... | 81 |
| 4.3.2 Piston Characteristics..... | 82 |
| 4.4 Experimental Results | 87 |
| | |
| CHAPTER 5 PISTON FINITE ELEMENT ANALYSIS: THE FULL MODEL | |
| APPROACH | 89 |
| 5.1 Introduction..... | 89 |
| 5.2 Preprocessing | 89 |
| 5.2.1 CAD Model..... | 90 |
| 5.2.2 Mesh and boundary conditions | 91 |
| 5.3 Piston Finite Element Analysis (π - <i>fea</i>) program | 92 |
| 5.4 π - <i>fea</i> Verification | 103 |
| | |
| CHAPTER 6 RESULTS A..... | 105 |
| 6.1 Introduction..... | 105 |
| 6.2 Engine geometry and operating conditions..... | 105 |
| 6.3 Piston geometry and properties..... | 106 |
| 6.4 Mesh Refinement | 108 |
| 6.5 Periodicity and convergence | 112 |
| 6.6 Simulation Results | 114 |
| 6.6.1 Temperature | 115 |
| 6.6.2 Deformation | 115 |
| 6.6.3 Strain | 116 |
| 6.6.4 Stress..... | 117 |
| 6.6.5 Lubrication Pressure | 118 |
| 6.6.6 Oil Film Thickness..... | 122 |
| 6.6.7 Forces and Moments..... | 123 |
| | |
| CHAPTER 7 CONCLUSIONS AND RECOMMENDATIONS | 128 |
| 7.1 Conclusions..... | 128 |
| 7.2 Recommendations..... | 132 |
| | |
| APPENDIX A..... | 135 |
| | |
| APPENDIX B..... | 146 |
| | |
| REFERENCES..... | 162 |

LIST OF TABLES

| | |
|---|-----|
| Table 2.1: Values for Eq. (2.23) | 14 |
| Table 2.2: Face to node assignment for linear | 15 |
| Table 2.3: Values for Eq. (2.47) | 21 |
| Table 3.1: Engine geometry and operating conditions | 55 |
| Table 4.1: Parameterized piston model feature labels | 60 |
| Table 4.2: Heat transfer coefficient and ambient temperature values for parameterized piston..... | 64 |
| Table 4.3: Maximum and minimum temperature for the three sets of heat transfer coefficients..... | 68 |
| Table 4.4: Maximum and mean deformations on skirt..... | 80 |
| Table 4.5: Mesh and computation time comparison..... | 80 |
| Table 5.1: Flags for thermal analysis..... | 91 |
| Table 5.2: Flags for static analysis..... | 92 |
| Table 6.1: Engine geometry and operating conditions | 105 |
| Table 6.2: Piston properties | 106 |
| Table 6.3: Material properties for aluminum alloy 1345..... | 107 |
| Table 6.4: Thermal boundary conditions..... | 108 |
| Table 6.5: Mesh sizes..... | 110 |

LIST OF FIGURES

| | |
|--|----|
| Figure 2.1: Piston CAD model, (a) top side, (b) underside | 6 |
| Figure 2.2: Finite element mesh of piston, (a) top side, (b) underside | 7 |
| Figure 2.3: Linear triangular element | 11 |
| Figure 2.4: Triangular element in its natural coordinates | 13 |
| Figure 2.5: Linear tetrahedral element..... | 14 |
| Figure 2.6: Nodal degrees of freedom for displacement analysis..... | 18 |
| Figure 2.7: Tetrahedron natural coordinates | 19 |
| Figure 2.8: 3D arbitrary body | 22 |
| Figure 2.9: Body and coordinate system for Reynolds lubrication equation..... | 38 |
| Figure 2.10: 2D arbitrary body | 39 |
| Figure 2.11: Graphical representation of the population of a sparse matrix..... | 46 |
| Figure 2.12: Conjugate gradient method flowchart | 49 |
| Figure 3.1: Piston terminology | 50 |
| Figure 3.2: Piston assembly | 52 |
| Figure 3.3: Piston position extremities: bottom dead center and top dead center | 53 |
| Figure 3.4: Piston position | 55 |
| Figure 3.5: Piston velocity | 56 |
| Figure 3.6: Piston acceleration..... | 56 |
| Figure 3.7: Angle φ | 57 |
| Figure 4.1: Full piston model mesh in COSMOSDesignSTAR, (a) top side, (b) underside | 59 |
| Figure 4.2: Parameterized piston model mesh in CASE, (a) top side, (b) underside | 59 |

| | |
|---|----|
| Figure 4.3: Parameterized piston dimensions | 60 |
| Figure 4.4: Pressure trace of optical engine..... | 61 |
| Figure 4.5: In-cylinder air temperature for optical engine..... | 62 |
| Figure 4.6: Heat transfer coefficient above piston crown using Annand and Woschni correlations..... | 62 |
| Figure 4.7: Heat transfer coefficients for parameterized piston | 64 |
| Figure 4.8: Full piston model temperature distribution with boundary conditions of Table 4.2 (temperature in Kelvin)..... | 65 |
| Figure 4.9: Full piston model temperature distribution with heat transfer coefficient values increased by 15% (temperature in Kelvin) | 65 |
| Figure 4.10: Full piston model temperature distribution with heat transfer coefficient values decreased by 15% (temperature in Kelvin) | 66 |
| Figure 4.11: Parameterized piston model temperature distribution with boundary conditions of Table 4.2 (temperature in Kelvin)..... | 66 |
| Figure 4.12: Parameterized piston model temperature distribution with heat transfer coefficient values increased by 15% (temperature in Kelvin)..... | 67 |
| Figure 4.13: Parameterized piston model temperature distribution with heat transfer coefficient values decreased by 15% (temperature in Kelvin) | 67 |
| Figure 4.14: Full piston model deformation due to thermal loading (URES: resultant deformation in mm, deformation scale 1:50) | 69 |
| Figure 4.15: Parameterized piston model deformation due to thermal loading (URES: resultant deformation in mm, deformation scale 1:50) | 69 |
| Figure 4.16: Mechanical loading, red arrows: atmospheric pressure, green arrows: constraint, body load not shown | 70 |
| Figure 4.17: Full piston model deformation due to mechanical loading (URES: resultant deformation in mm, deformation scale 1:50) | 71 |
| Figure 4.18: Parameterized piston model deformation due to mechanical loading (URES: resultant deformation in mm, deformation scale 1:50) | 71 |
| Figure 4.19: Pressure loads on skirt..... | 73 |
| Figure 4.20: Full piston model deformation due to load case 1..... | 73 |
| Figure 4.21: Parameterized piston model deformation due to load case 1 | 74 |

| | |
|---|----|
| Figure 4.22: Full piston model deformation due to load case 2..... | 74 |
| Figure 4.23: Parameterized piston model deformation due to load case 2 | 75 |
| Figure 4.24: Full piston model deformation due to load case 3..... | 75 |
| Figure 4.25: Parameterized piston model deformation due to load case 3 | 76 |
| Figure 4.26: Full piston model deformation due to load case 4..... | 76 |
| Figure 4.27: Parameterized piston model deformation due to load case 4 | 77 |
| Figure 4.28: Full piston model deformation due to load case 5..... | 77 |
| Figure 4.29: Parameterized piston model deformation due to load case 5 | 78 |
| Figure 4.30: Full piston model deformation due to load case 6..... | 78 |
| Figure 4.31: Parameterized piston model deformation due to load case 6 | 79 |
| Figure 4.32: Parameterized piston model temperature distribution from CASE (temperature in degrees Celsius)..... | 81 |
| Figure 4.33: Parameterized piston model deformation obtained from CASE (deformation in mm)..... | 82 |
| Figure 4.34: Skirt oil film thickness on thrust side at 33 CAD | 83 |
| Figure 4.35: Skirt oil film thickness on anti-thrust side at 33 CAD | 84 |
| Figure 4.36: Friction force between piston and cylinder liner..... | 84 |
| Figure 4.37: Contact points of piston with cylinder wall..... | 85 |
| Figure 4.38: Cyclic piston rotation about pin | 86 |
| Figure 4.39: Cyclic piston pin lateral motion | 86 |
| Figure 4.40: Experimental oil film thickness measurement at TDC of intake stroke..... | 88 |
| Figure 4.41: Simulated oil film thickness prediction at TDC of intake stroke | 88 |
| Figure 5.1: Piston orientation..... | 90 |
| Figure 5.2: Overview of the π - <i>fea</i> program flow | 93 |
| Figure 5.3: 2D skirt profile | 95 |
| Figure 5.4: Forces and moments acting on piston | 98 |

| | |
|---|-----|
| Figure 5.5: Nodal temperature as predicted by π - <i>fea</i> and COSMOSDesignSTAR..... | 104 |
| Figure 5.6: Nodal resultant deformation as predicted by π - <i>fea</i> and COSMOSDesignSTAR | 104 |
| Figure 6.1: Pressure trace used for simulation..... | 106 |
| Figure 6.2: Piston CAD model, (a) isometric view, anti-thrust side shown, (b) underside, (c) front view, anti-thrust side shown, (d) side view, red: thrust side..... | 107 |
| Figure 6.3: Imported piston meshed geometry, global element size: 9.2502 mm, skirt element size: 3 mm | 109 |
| Figure 6.4: Skirt mesh, (a) thrust side, (b) anti-thrust side | 109 |
| Figure 6.5: Hydrodynamic force on thrust side for meshes of Table 6.5 | 110 |
| Figure 6.6: Hydrodynamic force on anti-thrust side for meshes of Table 6.5 | 111 |
| Figure 6.7: Total hydrodynamic friction force for meshes of Table 6.5..... | 111 |
| Figure 6.8: Hydrodynamic force over three cycles, $C = 100 \mu\text{m}$ | 112 |
| Figure 6.9: Hydrodynamic force over three cycles, $C = 50 \mu\text{m}$ | 113 |
| Figure 6.10: Hydrodynamic pressure convergence at 3 rd cycle, $C = 100 \mu\text{m}$ | 113 |
| Figure 6.11: Hydrodynamic pressure convergence at 3 rd cycle, $C = 50 \mu\text{m}$ | 114 |
| Figure 6.12: Temperature distribution | 115 |
| Figure 6.13: Deformation at 405 deg.: x -component, (a) $C = 100 \mu\text{m}$, (b) $C = 50 \mu\text{m}$.. | 116 |
| Figure 6.14: Equivalent strain at 405 deg., $C = 100 \mu\text{m}$ | 116 |
| Figure 6.15: von Mises stress at 405 deg., $C = 100 \mu\text{m}$ | 117 |
| Figure 6.16: 3D von Mises yield criterion at 405 deg., $C = 100 \mu\text{m}$ | 118 |
| Figure 6.17: Hydrodynamic pressure on thrust side at 315 deg., $C = 100 \mu\text{m}$ | 119 |
| Figure 6.18: Hydrodynamic pressure on anti-thrust side at 315 deg., $C = 100 \mu\text{m}$ | 119 |
| Figure 6.19: Hydrodynamic pressure on thrust side at 405 deg., $C = 100 \mu\text{m}$ | 120 |
| Figure 6.20: Hydrodynamic pressure on anti-thrust side at 405 deg., $C = 100 \mu\text{m}$ | 120 |
| Figure 6.21: Hydrodynamic pressure on thrust side at 405 deg., $C = 50 \mu\text{m}$ | 121 |

| | |
|---|-----|
| Figure 6.22: Hydrodynamic pressure on thrust side at 405 deg., $C = 50 \mu\text{m}$ | 121 |
| Figure 6.23: Oil film thickness on thrust side at 405 deg., $C = 100 \mu\text{m}$ | 122 |
| Figure 6.24: Oil film thickness on anti-thrust side at 405 deg., $C = 100 \mu\text{m}$ | 123 |
| Figure 6.25: Total hydrodynamic force on piston | 124 |
| Figure 6.26: Plane parallel to pinhole axis and coincident with piston axis..... | 124 |
| Figure 6.27: Histogram of resultant deformation on thrust and anti-thrust side due to thermal expansion only | 125 |
| Figure 6.28: Total contact force on piston | 126 |
| Figure 6.29: Total friction force on piston..... | 126 |
| Figure 6.30: Total moment on piston..... | 127 |
| Figure A.1: Flow chart for the main program of π - <i>fea</i> (Part 1 of 2)..... | 135 |
| Figure A.2: Flow chart for the main program of π - <i>fea</i> (Part 2 of 2)..... | 136 |
| Figure A.3: Flowchart for <i>FEMmeshread</i> subroutine..... | 137 |
| Figure A.4: Flowchart for <i>FEMthermal</i> subroutine..... | 138 |
| Figure A.5: Flowchart for <i>FEMstatic</i> subroutine (Part 1 of 2) | 139 |
| Figure A.6: Flowchart for <i>FEMstatic</i> subroutine (Part 2 of 2) | 140 |
| Figure A.7: Flowchart for <i>FEMGuyan</i> subroutine | 141 |
| Figure A.8: Flowchart for <i>FEMstaticLUB</i> subroutine | 142 |
| Figure A.9: Flowchart for <i>ReEq</i> subroutine..... | 143 |
| Figure A.10: Flowchart for <i>FEMstrain</i> subroutine..... | 144 |
| Figure B.1: Temperature distribution | 146 |
| Figure B.2: Deformation: x-component..... | 147 |
| Figure B.3: Deformation: y-component..... | 147 |
| Figure B.4: Deformation: z-component | 148 |
| Figure B.5: Deformation: resultant | 148 |
| Figure B.6: Deformation: resultant, scale 1:800..... | 149 |

| | |
|--|-----|
| Figure B.7: Normal strain: x -component | 149 |
| Figure B.8: Normal strain: y -component | 150 |
| Figure B.9: Normal strain: z -component | 150 |
| Figure B.10: Shear strain: xy -component..... | 151 |
| Figure B.11: Shear strain: xz -component..... | 151 |
| Figure B.12: Shear strain: yz -component..... | 152 |
| Figure B.13: Equivalent strain | 152 |
| Figure B.14: Normal stress: x -component | 153 |
| Figure B.15: Normal stress: y -component | 153 |
| Figure B.16: Normal stress: z -component | 154 |
| Figure B.17: Shear stress: xy -component..... | 154 |
| Figure B.18: Shear stress: xz -component..... | 155 |
| Figure B.19: Shear stress: yz -component..... | 155 |
| Figure B.20: Principle stress: 1 st principal direction..... | 156 |
| Figure B.21: Principle stress: 2 nd principal direction..... | 156 |
| Figure B.22: Principle stress: 3 rd principal direction | 157 |
| Figure B.23: von Mises stress | 157 |
| Figure B.24: Stress intensity | 158 |
| Figure B.25: 3D von Mises yield criterion | 158 |
| Figure B.26: Hydrodynamic pressure: thrust side | 159 |
| Figure B.27: Hydrodynamic pressure: anti-thrust side | 159 |
| Figure B.28: Oil film thickness: thrust side..... | 160 |
| Figure B.29: Oil film thickness: anti-thrust side..... | 160 |

KEY TO SYMBOLS AND ABBREVIATIONS

| | |
|----------------------|--|
| ∇ | gradient, divergence |
| 2D | two dimensional |
| 3D | three dimensional |
| A | element area |
| a_1, a_2, a_3 | shape function constant for triangular element |
| a_1, a_2, a_3, a_4 | shape function constant for tetrahedral element |
| a_p | piston acceleration |
| A_s | skirt area |
| b_1, b_2, b_3 | shape function x -coefficient for triangular element |
| b_1, b_2, b_3, b_4 | shape function x -coefficient for tetrahedral element |
| $[B]$ | matrix of shape function derivatives |
| BDC | bottom dead center |
| b_l | body load |
| c_1, c_2, c_3 | shape function y -coefficient for triangular element |
| c_1, c_2, c_3, c_4 | shape function y -coefficient for tetrahedral element |
| C | nominal piston to cylinder bore clearance, compliance matrix |
| CAD | Computer Aided Design |
| CAE | Computer Aided Engineering |
| CASE | Cylinder-kit Analysis System for Engines |
| const | constant |
| d | pin offset, total deformation |

| | |
|-------------------|---|
| d_b | piston deformation due to body load |
| d_{bu} | piston deformation due to unit body load |
| $deg.$ | degrees |
| d_g | piston deformation due to combustion gas pressure |
| d_{gu} | piston deformation due to unit pressure on crown |
| d_r | resultant deformation |
| $d_{s,m}$ | total deformation on skirt side m |
| d_{sh} | deformation on skirt due to hydrodynamic pressure loading |
| d_t | deformation due to thermal strain |
| E | modulus of elasticity |
| f | function |
| F | function |
| F_c | contact force |
| FEA | Finite Element Analysis |
| FEM | Finite Element Method |
| F_f | total friction force |
| F_{fc} | contact friction force |
| F_{fh} | hydrodynamic friction force |
| F_h | hydrodynamic force |
| F_t | total force |
| \bar{F}_v | load vector due to physical wedge |
| $\bar{F}_h^{(e)}$ | load vector of element 'e' due to squeeze film |

| | |
|----------------------|--|
| \bar{F}_h | load vector due to squeeze film |
| $\bar{F}_v^{(e)}$ | load vector of element e due to physical wedge |
| h | heat transfer coefficient, oil film thickness |
| h_1 | heat transfer coefficient of piston ring-pack |
| h_2 | heat transfer coefficient of piston skirt |
| h_3 | heat transfer coefficient of piston underside |
| h_g | combustion gas heat transfer coefficient |
| \dot{h} | squeeze film velocity |
| I | functional |
| i | i^{th} node |
| j | j^{th} node |
| $[K]$ | global stiffness matrix |
| $[K^{(e)}]$ | stiffness matrix of element e |
| \bar{k} | thermal conductivity vector |
| k | thermal conductivity |
| k_x, k_y, k_z | thermal conductivities along x, y, z axes |
| $[K_{red}]$ | reduced global stiffness matrix |
| l | connecting rod length |
| L_1, L_2, L_3 | natural coordinates for triangular element |
| L_1, L_2, L_3, L_4 | natural coordinates for tetrahedral element |
| m | number of matrix entries |
| M | total moment |

| | |
|----------------------|--|
| M_c | contact moment |
| M_{fc} | moment due to contact friction force |
| M_{fh} | moment due to hydrodynamic friction |
| M_h | hydrodynamic moment |
| min | minute |
| N | engine speed |
| $[N]$ | shape function matrix |
| n | index number |
| N_1, N_2, N_3 | shape functions for triangular element |
| N_1, N_2, N_3, N_4 | shape functions for tetrahedral element |
| nel | number of elements |
| n_x, n_y, n_z | direction cosines |
| P | pressure |
| $\bar{P}^{(e)}$ | load vector of element e |
| \bar{P} | load vector, pressure vector |
| $\bar{P}_b^{(e)}$ | load vector of element e due to body forces |
| \bar{P}_b | load vector due to body forces |
| P_c | contact pressure |
| P_g | combustion gas pressure |
| P_h | hydrodynamic pressure |
| P_{res} | pressure residual |
| $\bar{P}_s^{(e)}$ | load vector of element e due to surface forces |

| | |
|-------------------|---|
| \bar{P}_s | load vector due to surface forces |
| $\bar{P}_t^{(e)}$ | load vector of element e due to thermal strains |
| \bar{P}_t | load vector due to thermal strains |
| P_t | total pressure |
| P_u | uniform pressure |
| \bar{Q} | vector of nodal displacements |
| $[R]$ | elasticity matrix |
| R | residual |
| r | residual, crankshaft radius |
| rev | revolution |
| \bar{s} | search direction |
| subscript m | skirt side m |
| superscript e | element e |
| T_∞ | ambient temperature |
| T_1 | ambient temperature of piston ring-pack |
| T_2 | ambient temperature of piston skirt |
| T_3 | ambient temperature of piston underside |
| T | temperature |
| $T_{avg}^{(e)}$ | average temperature of element 'e' |
| T_{ref} | reference temperature |
| TDC | top dead center |
| T_g | combustion gas temperature |

| | |
|-----------|---|
| \vec{U} | displacement vector |
| u, v, w | components of displacement parallel to x, y, z axes |
| V | element volume |
| V | relative velocity |
| V_a | velocity of body a |
| V_b | velocity of body b |
| v_p | piston velocity |
| x | x -axis, x -direction, x -coordinate |
| x_s | local skirt x -coordinate |
| y | variable, y -axis, y -direction, y -coordinate |
| y_p | piston position |
| y_s | local skirt y -coordinate |
| z | z -axis, z -direction, z -coordinate |

| | |
|---------------------------------|--|
| α | coefficient of thermal expansion |
| α, β, γ | shape function power for triangular element |
| $\alpha, \beta, \gamma, \delta$ | shape function power for tetrahedral element |
| β | constant for conjugate gradient |
| γ | shear strain |
| Γ | surface boundary |
| δ_m | wavy deformation |
| ΔT | change in temperature |
| Δt | time step |
| ε | normal strain |
| ε_{eq} | equivalent strain |
| ε_o | initial thermal strain |
| η_i | i^{th} generalized coefficient |
| θ | engine crank angle |
| λ | step length |
| A | strain energy |
| μ | lubricant viscosity |
| ν | Poisson's ratio |
| E | variable |
| Π | potential energy |
| σ | normal stress |
| $\sigma_1, \sigma_2, \sigma_3$ | principal stresses |
| σ_{int} | stress intensity |

| | |
|----------------|--|
| σ_{von} | von Mises stress |
| τ | shear stress |
| φ | angle of connecting rod with piston axis, body force |
| Φ_j^* | prescribed boundary condition |
| $\bar{\Phi}$ | surface force vector |
| Φ | element behavior |
| χ | switch function |
| Ψ | work done on a body by external forces |
| ω | weight function, angular speed |
| Ω | domain, waviness |
| ω_r | underrelaxation factor |

CHAPTER 1

INTRODUCTION

1.1 Motivation

As the oil prices increase, the emission standards tighten, and the competition in the automotive market strengthens, the search for a more efficient reciprocating internal combustion engine becomes vital. The prime “navigators” in this search are computational tools. Such tools allow for a fast and relatively cheap course for a prototype design, but can also be utilized for troubleshooting and optimization of existing designs.

The internal combustion engine has been around for more than a century but its physics are still not well understood. Its cyclic behavior represents an unsteady complex system with multiple physical processes occurring simultaneously. The system then is a multidisciplinary one which can be described by combustion [21, 41], thermodynamics [3, 39], heat transfer [27, 29], solid mechanics [2, 53], fluid mechanics [43, 46], dynamics [22, 26], and tribology [32, 38].

The “heart” of a reciprocating internal combustion engine is the piston. The function of the piston is to convert the thermal energy of the combustion gases into the mechanical energy that drives the engine. It is generally believed that about half of the mechanical energy is lost just at the piston assembly. Therefore piston design is a very important factor in engine efficiency.

The piston is confined within a cylinder bore, which acts as a guide to the piston’s reciprocating motion. The piston skirt slides on the cylinder’s surface, thus providing the

support for the whole piston body. Under favorable operating conditions an oil film separates the two surfaces. During a cycle the piston is exposed to sharp temperature and pressure gradients due to the combustion gases just above its crown. The reciprocating motion also exposes the piston to inertial loads. These gradients and loads affect the mechanical behavior of the piston skirt, which directly affects the thickness of the oil film, which in turn, determines the piston dynamics and the interaction of the piston with the cylinder wall. If the oil film thickness is too low, then piston scuffing can be a problem. If the thickness is too high, piston slap can be a problem. Therefore piston quality depends on optimal geometrical design, body mass and material selection, that ensure minimal energy loss due to inertia, heat transfer and piston-bore interaction. However finding the optimal set of design characteristics that would yield optimal piston quality is a very challenging job. Consequently computational tools become very important in piston design.

1.2 Previous Efforts in Piston Modeling

Piston modeling can be divided into four subcategories: thermal modeling, solid modeling, elastohydrodynamic lubrication modeling, and dynamic modeling. Over the years several research efforts have been made in these areas.

Annand [1] and Woschni [55] proposed correlations to calculate the heat transfer coefficient of the combustion gases above the piston crown. Woschni [56] did some further work for the evaluation of the heat transfer coefficients for a high speed diesel engine piston. He used the electrolytic tank analogue to obtain temperature measurements to calculate the heat transfer coefficients. He proposed ranges for heat transfer

coefficients describing the different surfaces of the piston. Wu et al. [57] modified Annand's correlation to include radiation effects, and they developed a numerical model for the calculation of the temperature distribution. Their analytical results showed reasonable agreement with experimental ones.

Li [35] considered the piston's thermoelastic behavior. He assumed that temperature fluctuations during a cycle affect a piston layer only about 2 mm thick. Beyond this layer the temperature is steady, given enough operating time for the engine. Consequently he treated the piston's thermoelastic behavior as a steady state problem. He used experimental temperature measurements to propose a range of heat transfer coefficients for an aluminum gasoline piston. He used these results and a finite element model of a quarter of the piston to investigate the thermoelastic behavior of the piston over a cycle.

Li et al. [37] developed an automotive piston lubrication model to study the effects of piston pin location, piston-to-cylinder clearances and lubricant viscosities on piston dynamics and friction. They solved for particular solutions of the Reynolds equation using finite differences, and used the Newton-Raphson method to solve for the nonlinear equations of motion for the piston. In their model they assumed a rigid piston model. Li [36] considered the elastic deformation of the piston skirt; integrating this with hydrodynamic lubrication has formed the elastohydrodynamic lubrication analysis which is considered by most of the recent efforts [9, 10, 11, 18, 30, 31, 40, 45, 54, 58, 59]. All these have contributed in solving the elastic deformation of the piston using the finite element method. Oh et al. [40] used the finite element method to solve for the Reynolds equation; however they linearized it, thus solving for a set of linear equations. The rest of

the efforts use finite differences to solve for the Reynolds equation. This method however requires mapping of nodal information, back and forth, from the finite element mesh to the finite difference grid. This can result in the loss of crucial numerical information, especially where sharp gradients exist between two nodes. Zhu et al. [58, 59] were the first to consider the elastic deformation of the cylinder bore. They also proposed a formula for the asperity contact pressure of an aluminum piston against a cast iron cylinder according to Johnson's model (1985). They also used the Reynolds equation developed by Patir and Cheng (1978) which accounts for the effect of surface texture on hydrodynamic lubrication. Duyar et al. [11] coupled the Reynolds equation with the mass-conserving Reynolds equation to solve for the hydrodynamic pressure using finite volumes. Computer aided engineering (CAE) tools for piston analysis have been introduced in recent years, such as CASE [4], PISDYN [11] and GLIDE [24].

1.3 Objective

In this thesis, the author joins the disciplines of heat transfer, solid mechanics, fluid mechanics and tribology to develop a computational model for the assessment of piston quality. The Cylinder-kit Analysis System for Engines (CASE) is a comprehensive cylinder-kit simulation software that is being widely used to predict piston dynamics, ring-pack dynamics, oil film thickness and friction [6, 7, 12, 13, 14, 15, 16, 42]. Currently CASE uses a parameterized piston model which is generated using a set of selected geometrical parameters from the full piston model. The main advantage of the parameterized model is its relatively simple geometry. This allows for the construction of a simple small mesh where the governing equations can be solved very fast. Another

advantage of the parameterized model is its self-generation. This allows CASE, when coupled with optimization software, to perform an optimization simulation very quickly without the need of external computer-aided design (CAD) software to change the piston's geometry. The author develops a piston finite element analysis program to supplement the existing one of CASE. This program is capable of importing the meshed geometry of a full CAD piston model and performs a cyclic analysis to assess the piston quality. The parameterized approach has proven to be a less expensive approach in piston quality assessment in terms of cost, time and effort. The objective then is to be able to assess the optimal piston design characteristics like piston-pin location, skirt profile and piston ovality from the parameterized piston model and use them to update the CAD full piston model. Then a simulation for the modified CAD full piston model can be conducted to verify if the selection of optimal design characteristics can improve the performance.

In this thesis only the finite element part of the program is presented. At this stage piston secondary dynamics are ignored. The piston is assumed to be moving right in the centre of the cylinder bore, with no transverse movement or tilting. Viscosity variations along the length of the cylinder bore and cylinder bore deformation are ignored.

CHAPTER 2

THE FINITE ELEMENT METHOD

2.1 Introduction

This chapter introduces the reader to the finite element method, from hereon referred to as FEM, used in the preparation of this work. The philosophy of FEM is to find the solution of a complicated problem by replacing it by a simpler one. Consider the piston shown in Figure 2.1; it has a very complex geometry. The existing mathematical tools are not sufficient to find an exact solution for its behavior (temperature distribution, displacement distribution) under thermal and mechanical loading.

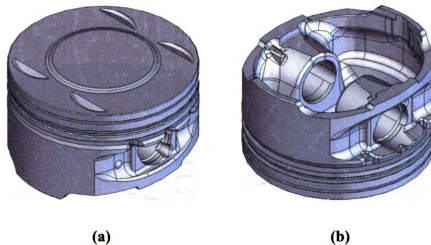


Figure 2.1: Piston CAD model, (a) top side, (b) underside

However an approximate solution can be obtained using FEM. The complex geometry of the piston can be divided into an assembly of many small sub-geometries called finite elements (Figure 2.2). These elements are interconnected at specified joints

called nodes or nodal points. These nodes are usually found on the element boundaries where adjacent elements are connected. Again the behavior of these finite elements is not known, however it is assumed that it can be approximated by simple functions. These approximating functions, also known as shape functions, are defined by the element behavior at the nodes. Equilibrium equations can be readily developed to describe the behavior of these finite elements. The unknowns arising from the development of these equations are the nodal values of the element behavior. The simultaneous solution of these equations describes the approximate behavior of the whole geometry. One advantage of FEM is that the approximate solution can be improved by refining the mesh. Of course however this would require more computational time. All of the theories introduced in this chapter are extracted from literature [5, 20, 23, 28, 32, 33, 34, 38, 44, 47, 48, 49, 50, 51, 52,].

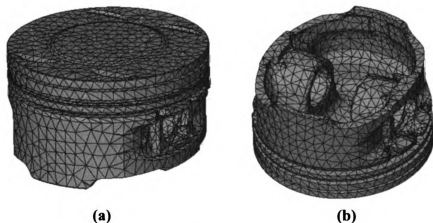


Figure 2.2: Finite element mesh of piston, (a) top side, (b) underside

2.2 Approximate Solutions

Consider the function given in Eq. (2.1)

$$f(\Omega) = y''(\Omega) + y'(\Omega) + y(\Omega) \quad (2.1)$$

The residual, R , is given by

$$R = y''(\Omega) + y'(\Omega) + y(\Omega) - f(\Omega) \quad (2.2)$$

The exact solution of Eq. (2.1) would yield $R = 0$. With approximate solutions, if R cannot be made zero, it is brought as close to zero as possible.

2.2.1 Galerkin's Method

This method, also known as the method of weighted residuals, tries to reduce the residual over the entire domain by making its weighted average zero with respect to as many independent weighting functions, ω , as there are unknown parameters. Assume that Eq. (2.1) is approximated by n unknown parameters, Ξ . Thus,

$$R = R(\Omega, \Xi_0, \Xi_1, \dots, \Xi_n) \quad (2.3)$$

This results in,

$$\begin{aligned} \int_{\Omega} \omega_1 R(\Omega, \Xi_1, \Xi_2, \dots, \Xi_n) d\Omega &= 0 \\ \int_{\Omega} \omega_2 R(\Omega, \Xi_1, \Xi_2, \dots, \Xi_n) d\Omega &= 0 \\ &\vdots \\ \int_{\Omega} \omega_n R(\Omega, \Xi_1, \Xi_2, \dots, \Xi_n) d\Omega &= 0 \end{aligned} \quad (2.4)$$

Galerkin's method uses the element shape functions as the weighting functions. This ensures that the weighting functions are independent of each other and consequently the resulting algebraic equations are independent.

2.2.2 Variational Method

This method arises from calculus of variations. The main idea behind calculus of variations is to determine the extreme (maximum and minimum) or stationary values of functionals. A functional, I , is defined as function of other functions. Functionals of equilibrium equations have been derived and are found in literature. Considering Eq. (2.1) again approximated by n unknown parameters, Ξ , its functional can be given by,

$$I = \int_{\Omega} F(\Omega, \Xi_0, \Xi_1, \dots, \Xi_n) d\Omega \quad (2.5)$$

Values of Ξ_i , for $i = 1, 2, \dots, n$, are sought which will minimize I , that is,

$$\frac{\partial I}{\partial \Xi_1} = \frac{\partial I}{\partial \Xi_2} = \dots = \frac{\partial I}{\partial \Xi_n} = 0 \quad (2.6)$$

Equation (2.6) will result in n equations with n unknowns.

2.3 Elements and their Shape Functions

2.3.1 Linear Triangular Element

A linear triangular element (Figure 2.3) is a three-node element with straight edges. The nodes are numbered in a counter-clockwise order. Node 1 can be specified arbitrarily. Let the element behavior (temperature, displacement) be Φ . Inside the element Φ is assumed to vary linearly, Eq. (2.7), and Φ_1 , Φ_2 , Φ_3 , Eq. (2.8), denote the behavior value at the respective nodes.

$$\Phi(x, y) = \eta_1 + \eta_2 x + \eta_3 y \quad (2.7)$$

$$\begin{aligned}
\Phi_1 &= \eta_1 + \eta_2 x_1 + \eta_3 y_1 \\
\Phi_2 &= \eta_1 + \eta_2 x_2 + \eta_3 y_2 \\
\Phi_3 &= \eta_1 + \eta_2 x_3 + \eta_3 y_3
\end{aligned} \tag{2.8}$$

The solution of Eqs. (2.8) leads to

$$\begin{aligned}
\eta_1 &= \frac{1}{2A}(a_1\Phi_1 + a_2\Phi_2 + a_3\Phi_3) \\
\eta_2 &= \frac{1}{2A}(b_1\Phi_1 + b_2\Phi_2 + b_3\Phi_3) \\
\eta_3 &= \frac{1}{2A}(c_1\Phi_1 + c_2\Phi_2 + c_3\Phi_3)
\end{aligned} \tag{2.9}$$

where A is the area of triangle 1-2-3. The area is given by

$$A = \frac{1}{2} \begin{vmatrix} 1 & x_1 & y_1 \\ 1 & x_2 & y_2 \\ 1 & x_3 & y_3 \end{vmatrix} \tag{2.10}$$

and

$$\begin{aligned}
a_1 &= x_2 y_3 - x_3 y_2 \\
a_2 &= x_3 y_1 - x_1 y_2 \\
a_3 &= x_1 y_2 - x_2 y_1 \\
b_1 &= y_2 - y_3 \\
b_2 &= y_3 - y_1 \\
b_3 &= y_1 - y_2 \\
c_1 &= x_3 - x_2 \\
c_2 &= x_1 - x_3 \\
c_3 &= x_2 - x_1
\end{aligned} \tag{2.11}$$

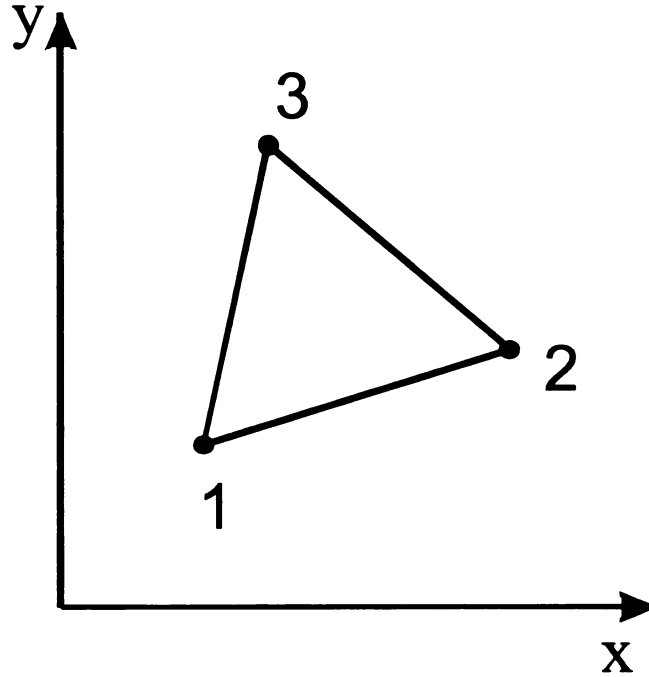


Figure 2.3: Linear triangular element

Substituting Eq. (2.9) into Eq. (2.7) and rearranging leads to

$$\Phi(x, y) = N_1(x, y)\Phi_1 + N_2(x, y)\Phi_2 + N_3(x, y)\Phi_3 \quad (2.12)$$

where,

$$\begin{aligned} N_1 &= \frac{1}{2A}(a_1 + b_1x + c_1y) \\ N_2 &= \frac{1}{2A}(a_2 + b_2x + c_2y) \\ N_3 &= \frac{1}{2A}(a_3 + b_3x + c_3y) \end{aligned} \quad (2.13)$$

N_1 , N_2 , and N_3 are the element shape functions. It can be shown that evaluating the shape functions at x_i, y_i , $N_i = 1$, whereas $N_i = 0$, at nodes 2 and 3. Similarly the shape function N_2 and N_3 have a value of 1 at nodes 2 and 3 respectively and 0 at the other nodes.

Now let,

$$[N] = [N_1 \quad N_2 \quad N_3] \quad (2.14)$$

and

$$\bar{\Phi}^{(e)} = \begin{Bmatrix} \Phi_1 \\ \Phi_2 \\ \Phi_3 \end{Bmatrix} \quad (2.15)$$

where, $\bar{\Phi}^{(e)}$ is the vector of nodal unknowns of element e . Thus,

$$\Phi = [N] \bar{\Phi}^{(e)} \quad (2.16)$$

Since the functions are linear, their derivative with respect to x or y is constant. This suggests a constant derivative of Φ within the element, Eq. (2.17). Consequently very small elements have to be used where sharp gradients are expected in the value of Φ .

$$\frac{\partial \Phi}{\partial x} = \frac{\partial N_1}{\partial x} \Phi_1 + \frac{\partial N_2}{\partial x} \Phi_2 + \frac{\partial N_3}{\partial x} \Phi_3 \quad (2.17)$$

Now consider a triangular element in its natural coordinates (Figure 2.4), L_1 , L_2 , L_3 . These three coordinates define a point P in terms of the areas, Eq. (2.18),

$$L_1 = \frac{A_1}{A}, \quad L_2 = \frac{A_2}{A}, \quad L_3 = \frac{A_3}{A} \quad (2.18)$$

and

$$A_1 + A_2 + A_3 = A \quad (2.19)$$

thus,

$$L_1 + L_2 + L_3 = 1 \quad (2.20)$$

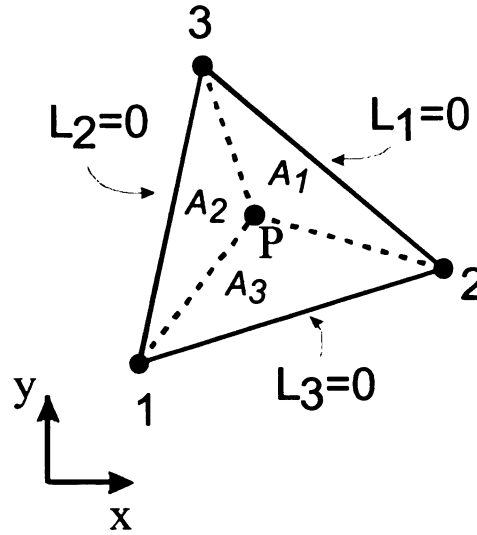


Figure 2.4: Triangular element in its natural coordinates

It can readily be shown that

$$L_1 = N_1, \quad L_2 = N_2, \quad L_3 = N_3 \quad (2.21)$$

The Cartesian coordinates of P are related to the natural ones by,

$$\begin{aligned} x &= x_1 L_1 + x_2 L_2 + x_3 L_3 \\ y &= y_1 L_1 + y_2 L_2 + y_3 L_3 \end{aligned} \quad (2.22)$$

For integrating polynomial terms in area coordinates Eq. (2.23) can be used,

$$\iint_A L_1^\alpha L_2^\beta L_3^\gamma dA = \frac{\alpha! \beta! \gamma!}{(\alpha + \beta + \gamma + 2)!} 2A \quad (2.23)$$

and since Eq. (2.21) is true, then

$$\iint_A N_1^\alpha N_2^\beta N_3^\gamma dA = \frac{\alpha! \beta! \gamma!}{(\alpha + \beta + \gamma + 2)!} 2A \quad (2.24)$$

Table 2.1 gives some common values for the integral of Eq. (2.23).

Table 2.1: Values for Eq. (2.23)

| α | Value of | | Value of integral in Eq. (2.23)/4 |
|----------|----------|----------|-----------------------------------|
| | β | γ | |
| 0 | 0 | 0 | 1 |
| 1 | 0 | 0 | 1/3 |
| 2 | 0 | 0 | 1/6 |
| 1 | 1 | 0 | 1/12 |
| 3 | 0 | 0 | 1/10 |
| 2 | 1 | 0 | 1/30 |
| 1 | 1 | 1 | 1/60 |
| 4 | 0 | 0 | 1/15 |
| 3 | 1 | 0 | 1/60 |

2.3.2 Linear Tetrahedral Element

The linear tetrahedron element is made of four flat triangular elements or faces, interconnected at the four corners, nodes 1, 2, 3 and 4. The nodes on any face are numbered in a counter-clockwise manner as seen from the vertex opposite the face. Table 2.2 shows the faces with their respective nodes as used in this work.

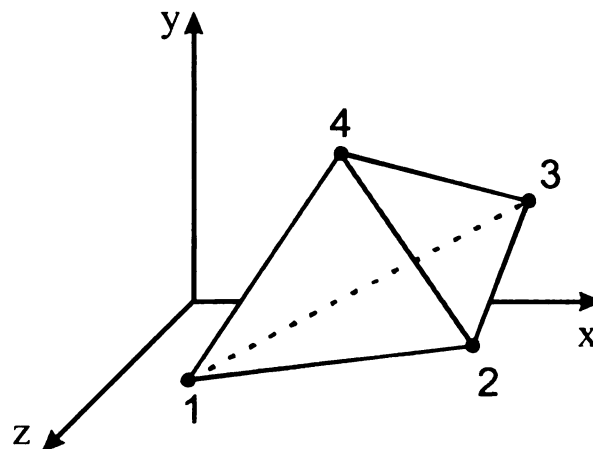


Figure 2.5: Linear tetrahedral element

Table 2.2: Face to node assignment for linear tetrahedral element

| <i>Face</i> | <i>Nodes</i> |
|-------------|--------------|
| 1 | 1-2-3 |
| 2 | 1-4-2 |
| 3 | 2-4-3 |
| 4 | 1-3-4 |

The derivation of the element shape functions is very similar as for the triangular element. Again here the element behavior, Φ , is assumed to vary linearly within the element,

$$\Phi(x, y, z) = \eta_1 + \eta_2 x + \eta_3 y + \eta_4 z \quad (2.25)$$

$$\begin{aligned} \Phi_1 &= \eta_1 + \eta_2 x_1 + \eta_3 y_1 + \eta_4 z_1 \\ \Phi_2 &= \eta_1 + \eta_2 x_2 + \eta_3 y_2 + \eta_4 z_2 \\ \Phi_3 &= \eta_1 + \eta_2 x_3 + \eta_3 y_3 + \eta_4 z_3 \\ \Phi_4 &= \eta_1 + \eta_2 x_4 + \eta_3 y_4 + \eta_4 z_4 \end{aligned} \quad (2.26)$$

The solution of Eqs. (2.26) leads to

$$\begin{aligned} \eta_1 &= \frac{1}{2V} (a_1 \Phi_1 + a_2 \Phi_2 + a_3 \Phi_3 + a_4 \Phi_4) \\ \eta_2 &= \frac{1}{2V} (b_1 \Phi_1 + b_2 \Phi_2 + b_3 \Phi_3 + b_4 \Phi_4) \\ \eta_3 &= \frac{1}{2V} (c_1 \Phi_1 + c_2 \Phi_2 + c_3 \Phi_3 + c_4 \Phi_4) \\ \eta_4 &= \frac{1}{2V} (d_1 \Phi_1 + d_2 \Phi_2 + d_3 \Phi_3 + d_4 \Phi_4) \end{aligned} \quad (2.27)$$

where V is the volume of the tetrahedron 1-2-3-4. The volume is given by,

$$V = \frac{1}{6} \begin{vmatrix} 1 & x_1 & y_1 & z_1 \\ 1 & x_2 & y_2 & z_2 \\ 1 & x_3 & y_3 & z_3 \\ 1 & x_4 & y_4 & z_4 \end{vmatrix} \quad (2.28)$$

and,

$$a_i = (-1)^{i+1} \begin{vmatrix} x_2 & y_2 & z_2 \\ x_3 & y_3 & z_3 \\ x_4 & y_4 & z_4 \end{vmatrix}, \quad (2.29)$$

$$b_i = (-1)^i \begin{vmatrix} 1 & y_2 & z_2 \\ 1 & y_3 & z_3 \\ 1 & y_4 & z_4 \end{vmatrix}, \quad (2.30)$$

$$c_i = (-1)^i \begin{vmatrix} x_2 & 1 & z_2 \\ x_3 & 1 & z_3 \\ x_4 & 1 & z_4 \end{vmatrix}, \quad (2.31)$$

$$d_i = (-1)^i \begin{vmatrix} x_2 & y_2 & 1 \\ x_3 & y_3 & 1 \\ x_4 & y_4 & 1 \end{vmatrix} \quad (2.32)$$

for $i = 1, 2, \dots, 4$. The subscripts of x , y , and z , in Eqs. (2.29) to (2.32), are interchanged cyclically in the order 4, 1, 2, 3. These equations are valid for a tetrahedron numbered as in Figure 2.5.

Substituting Eqs. (2.27) into Eq. (2.25) leads to,

$$\Phi(x, y, z) = N_1(x, y, z)\Phi_1 + N_2(x, y, z)\Phi_2 + N_3(x, y, z)\Phi_3 + N_4(x, y, z)\Phi_4 \quad (2.33)$$

where,

$$\begin{aligned}
N_1 &= \frac{1}{6V}(a_1 + b_1 x + c_1 y + d_1 z) \\
N_2 &= \frac{1}{6V}(a_2 + b_2 x + c_2 y + d_2 z) \\
N_3 &= \frac{1}{6V}(a_3 + b_3 x + c_3 y + d_3 z) \\
N_4 &= \frac{1}{6V}(a_4 + b_4 x + c_4 y + d_4 z)
\end{aligned} \tag{2.34}$$

$N_1, N_2, N_3,$ and N_4 have a value of one at nodes 1, 2, 3, and 4 respectively and zero elsewhere.

Now letting

$$[N] = [N_1 \quad N_2 \quad N_3 \quad N_4] \tag{2.35}$$

and

$$\bar{\Phi}^{(e)} = \begin{Bmatrix} \Phi_1 \\ \Phi_2 \\ \Phi_3 \\ \Phi_4 \end{Bmatrix} \tag{2.36}$$

then

$$\Phi = [N] \bar{\Phi}^{(e)} \tag{2.37}$$

As in the case of the triangular element the derivative of Φ with respect to x, y or z , within the element is constant, Eq. (2.38).

$$\frac{\partial \Phi}{\partial x} = \frac{\partial N_1}{\partial x} \Phi_1 + \frac{\partial N_2}{\partial x} \Phi_2 + \frac{\partial N_3}{\partial x} \Phi_3 + \frac{\partial N_4}{\partial x} \Phi_4 \tag{2.38}$$

So far Φ is assumed to be a scalar quantity; however there are cases (displacement analysis) where Φ is a vector (Figure 2.6).

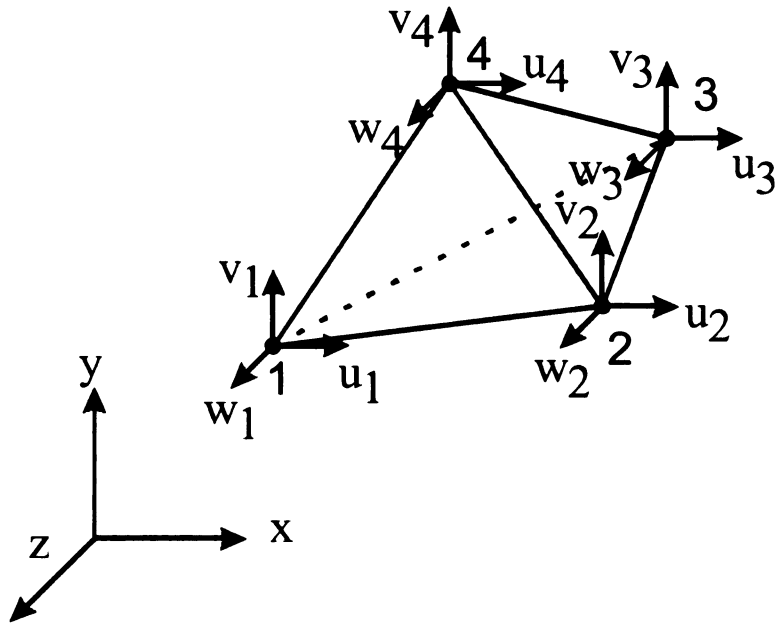


Figure 2.6: Nodal degrees of freedom for displacement analysis

In such a case $\bar{\Phi}^{(e)}$ becomes,

$$\bar{\Phi}^{(e)} = \begin{Bmatrix} u_1 \\ u_2 \\ u_3 \\ u_4 \\ v_1 \\ v_2 \\ v_3 \\ v_4 \\ w_1 \\ w_2 \\ w_3 \\ w_4 \end{Bmatrix} \quad (2.39)$$

and,

$$[N]^T = \begin{bmatrix} N_1 & 0 & 0 \\ N_2 & 0 & 0 \\ N_3 & 0 & 0 \\ N_4 & 0 & 0 \\ 0 & N_1 & 0 \\ 0 & N_2 & 0 \\ 0 & N_3 & 0 \\ 0 & N_4 & 0 \\ 0 & 0 & N_1 \\ 0 & 0 & N_2 \\ 0 & 0 & N_3 \\ 0 & 0 & N_4 \end{bmatrix} \quad (2.40)$$

so that,

$$\bar{\Phi} = \begin{Bmatrix} u \\ v \\ w \end{Bmatrix} = [N] \bar{\Phi}^{(e)} \quad (2.41)$$

Like the triangular element a tetrahedron can be described in its natural or volume coordinates, L_1, L_2, L_3, L_4 . These coordinates define a point P in terms of volumes (Figure 2.7).

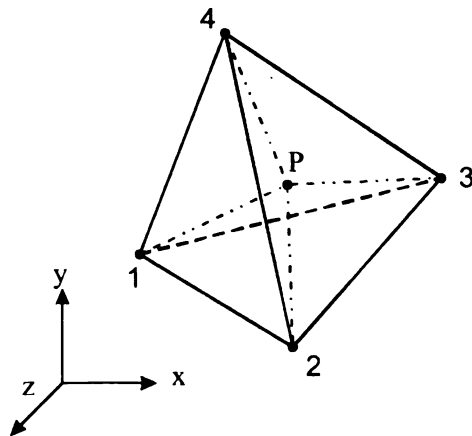


Figure 2.7: Tetrahedron natural coordinates

$$L_1 = \frac{V_1}{V}, L_2 = \frac{V_2}{V}, L_3 = \frac{V_3}{V}, L_4 = \frac{V_4}{V} \quad (2.42)$$

where,

V = Volume of 1-2-3-4

V_1 = Volume of P-2-3-4

V_2 = Volume of P-1-3-4

V_3 = Volume of P-1-2-4

V_4 = Volume of P-1-2-3

thus,

$$V_1 + V_2 + V_3 + V_4 = V \quad (2.43)$$

and

$$L_1 + L_2 + L_3 + L_4 = 1 \quad (2.44)$$

It can be readily shown that

$$L_1 = N_1, L_2 = N_2, L_3 = N_3, L_4 = N_4 \quad (2.45)$$

The Cartesian coordinates of P are related to the natural ones by,

$$\begin{aligned} x &= x_1 L_1 + x_2 L_2 + x_3 L_3 + x_4 L_4 \\ y &= y_1 L_1 + y_2 L_2 + y_3 L_3 + y_4 L_4 \\ z &= z_1 L_1 + z_2 L_2 + z_3 L_3 + z_4 L_4 \end{aligned} \quad (2.46)$$

For integrating polynomial terms in volume coordinates Eq.(2.47) can be used,

$$\iiint_V L_1^\alpha L_2^\beta L_3^\gamma L_4^\delta dV = \frac{\alpha! \beta! \gamma! \delta!}{(\alpha + \beta + \gamma + \delta + 3)!} 6V \quad (2.47)$$

and since Eq. (2.45) is true, then

$$\iiint_V N_1^\alpha N_2^\beta N_3^\gamma N_4^\delta dV = \frac{\alpha! \beta! \gamma! \delta!}{(\alpha + \beta + \gamma + \delta + 3)!} 6V \quad (2.48)$$

Table 2.3 gives some common values for the integral of Eq. (2.47)

Table 2.3: Values for Eq. (2.47)

| α | Value of | | | Value of integral in Eq. (2.47)/A |
|----------|----------|----------|----------|-----------------------------------|
| | β | γ | δ | |
| 0 | 0 | 0 | 0 | 1 |
| 1 | 0 | 0 | 0 | 1/4 |
| 2 | 0 | 0 | 0 | 1/10 |
| 1 | 1 | 0 | 0 | 1/20 |
| 3 | 0 | 0 | 0 | 1/20 |
| 2 | 1 | 0 | 0 | 1/60 |
| 1 | 1 | 1 | 0 | 1/120 |
| 4 | 0 | 0 | 0 | 1/35 |

2.4 Finite Element Formulation

2.4.1 Heat Equation

For a three-dimensional steady state problem with no heat generation (Figure 2.8) the governing differential equation is,

$$\nabla(\bar{k} \nabla T) = 0 \quad (2.49)$$

with a convective boundary,

$$k_x \frac{\partial T}{\partial x} n_x + k_y \frac{\partial T}{\partial y} n_y + k_z \frac{\partial T}{\partial z} n_z + h(T - T_\infty) = 0 \quad \text{on } \Gamma \quad (2.50)$$

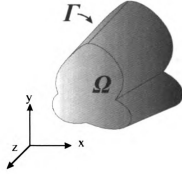


Figure 2.8: 3D arbitrary body

For an isotropic material where $k_x = k_y = k_z = k$, (2.49) reduces to,

$$\nabla^2 T = 0 \quad (2.51)$$

and (2.50) to,

$$\frac{\partial T}{\partial x} n_x + \frac{\partial T}{\partial y} n_y + \frac{\partial T}{\partial z} n_z + \frac{h}{k}(T - T_\infty) = 0 \quad (2.52)$$

Using Galerkin's method, multiplying by the weight function and integrating over the domain, Eq. (2.51) becomes

$$\int_{\Omega^{(e)}} \omega \nabla^2 T \, d\Omega^{(e)} = 0 \quad (2.53)$$

Using Green's first identity,

$$\int_{\Omega} (\nabla T \cdot \nabla \omega + \omega \nabla^2 T) \, d\Omega = \int_{\Gamma} \left(\frac{\partial T}{\partial x} n_x + \frac{\partial T}{\partial y} n_y + \frac{\partial T}{\partial z} n_z \right) \omega \, d\Gamma \quad (2.54)$$

Eq. (2.53) yields,

$$\int_{\Omega^{(e)}} \nabla T \cdot \nabla \omega \, d\Omega^{(e)} = \int_{\Gamma^{(e)}} \left(\frac{\partial T}{\partial x} n_x + \frac{\partial T}{\partial y} n_y + \frac{\partial T}{\partial z} n_z \right) \omega \, d\Gamma^{(e)} \quad (2.55)$$

From Eq. (2.52), Eq. (2.55) becomes,

$$\int_{\Omega^{(e)}} \nabla T \cdot \nabla \omega \, d\Omega^{(e)} = - \int_{\Gamma^{(e)}} \frac{h}{k} (T - T_{\infty}) \omega \, d\Gamma^{(e)} \quad (2.56)$$

Rearranging yields,

$$\int_{\Omega^{(e)}} \nabla T \cdot \nabla \omega \, d\Omega + \frac{h}{k} \int_{\Gamma^{(e)}} T \omega \, d\Gamma = \frac{hT_{\infty}}{k} \int_{\Gamma^{(e)}} \omega \, d\Gamma^{(e)} \quad (2.57)$$

By approximating T ,

$$T \approx N_i T_i \quad (2.58)$$

and,

$$\begin{aligned} \frac{\partial T}{\partial x} &\approx T_i \frac{\partial N_i}{\partial x} \\ \frac{\partial T}{\partial y} &\approx T_i \frac{\partial N_i}{\partial y} \\ \frac{\partial T}{\partial z} &\approx T_i \frac{\partial N_i}{\partial z} \end{aligned} \quad (2.59)$$

and,

$$\omega_j = N_j \quad (2.60)$$

Eq. (2.57) through (2.60) yield,

$$\begin{aligned} &\left[\int_{\Omega^{(e)}} \left(\frac{\partial N_i}{\partial x} \frac{\partial N_j}{\partial x} + \frac{\partial N_i}{\partial y} \frac{\partial N_j}{\partial y} + \frac{\partial N_i}{\partial z} \frac{\partial N_j}{\partial z} \right) d\Omega^{(e)} + \frac{h}{k} \int_{\Gamma^{(e)}} N_i N_j \, d\Gamma^{(e)} \right] \{T_i^{(e)}\} \\ &= \frac{hT_{\infty}}{k} \int_{\Gamma^{(e)}} N_i \, d\Gamma^{(e)} \end{aligned} \quad (2.61)$$

Equation (2.61) can be expressed as

$$\left(\left[K_1^{(e)} \right] + \left[K_2^{(e)} \right] \right) \bar{T}^{(e)} = \bar{P}^{(e)} \quad (2.62)$$

with,

$$\left[K_1^{(e)} \right] = \int_{\Omega^{(e)}} \left(\frac{\partial N_i}{\partial x} \frac{\partial N_j}{\partial x} + \frac{\partial N_i}{\partial y} \frac{\partial N_j}{\partial y} + \frac{\partial N_i}{\partial z} \frac{\partial N_j}{\partial z} \right) d\Omega^{(e)} \quad (2.63)$$

$$\left[K_2^{(e)} \right] = \frac{h}{k} \int_{\Gamma^{(e)}} N_i N_j d\Gamma^{(e)} \quad (2.64)$$

$$\bar{p}^{(e)} = \frac{h T_\infty}{k} \int_{\Gamma^{(e)}} N_i d\Gamma^{(e)} \quad (2.65)$$

Now recalling the shape functions for a tetrahedral element, Eq. (2.34), the shape function derivatives are given by,

$$\frac{\partial N_i}{\partial x} = \frac{b_i}{6V} \quad (2.66)$$

$$\frac{\partial N_i}{\partial y} = \frac{c_i}{6V} \quad (2.67)$$

$$\frac{\partial N_i}{\partial z} = \frac{d_i}{6V} \quad (2.68)$$

Thus considering the above equations, Eq. (2.63) becomes

$$\begin{aligned} \left[K_1^{(e)} \right] &= \int_{\Omega^{(e)}} \frac{1}{6V^2} (b_i b_j + c_i c_j + d_i d_j) d\Omega^{(e)} \\ &= \frac{1}{6V} (b_i b_j + c_i c_j + d_i d_j) \end{aligned} \quad (2.69)$$

Now considering Eq. (2.48) and assuming convection on face 1 of the tetrahedron

Eq. (2.64) becomes,

$$\begin{aligned}
[K_2^{(e)}] &= \frac{h}{k} \int_{\Gamma^{(e)}} N_i N_j d\Gamma^{(e)} \\
&= \frac{h_{123} A_{123}}{12k} \begin{bmatrix} 2 & 1 & 1 & 0 \\ 1 & 2 & 1 & 0 \\ 1 & 1 & 2 & 0 \\ 0 & 0 & 0 & 0 \end{bmatrix}
\end{aligned} \tag{2.70}$$

where h_{123} is the heat transfer coefficient on face 1 and A_{123} the area of face 1. The fourth row and column are all zeros as N_4 is zero on face 1. There are three other forms of Eq. (2.70) corresponding to faces 2, 3, and 4. Similarly the diagonal terms will be 2 and off-diagonal terms 1. The terms of the row and column associated with the node not lying on the face will be zero.

In a similar manner, for convection on face 1, Eq. (2.65) can be expressed as

$$\begin{aligned}
\bar{P}^{(e)} &= \frac{hT_\infty}{k} \int_{\Gamma^{(e)}} N_i d\Gamma^{(e)} \\
&= \frac{h_{123} T_\infty A_{123}}{3k} \begin{Bmatrix} 1 \\ 1 \\ 1 \\ 0 \end{Bmatrix}
\end{aligned} \tag{2.71}$$

Again there are three other forms of Eq. (2.71) corresponding to each face. Here the row corresponding to the node not lying on the face will be zero.

Eq. (2.69) to (2.71) represent the element matrices and vectors; assemblage of these leads to the global stiffness matrix, $[K]$, and global load vector \bar{P}

$$[K] = \sum_{e=1}^{nel} \left([K_1^{(e)}] + [K_2^{(e)}] \right) \tag{2.72}$$

$$\bar{P} = \sum_{e=1}^{nel} \bar{P}^{(e)} \tag{2.73}$$

thus,

$$[K]\bar{T} = \bar{P} \quad (2.74)$$

with \bar{T} being the vector of the unknown nodal temperatures.

2.4.2 Static Analysis

In this section the general equations governing solid and structural mechanics are presented. The principle of minimum potential energy, also known as displacement method, is used in deriving the finite element equations.

Equilibrium Equations

Consider the arbitrary body of Figure 2.8. If a load is applied on surface, Γ , and if an element of material is considered within the domain Ω , it must be in equilibrium due to the internal stresses developed. This leads to the internal equilibrium equations for a three-dimensional body,

$$\begin{aligned} \frac{\partial \sigma_{xx}}{\partial x} + \frac{\partial \tau_{xy}}{\partial y} + \frac{\partial \tau_{xz}}{\partial z} + \phi_x &= 0 \\ \frac{\partial \tau_{yx}}{\partial x} + \frac{\partial \sigma_{yy}}{\partial y} + \frac{\partial \tau_{yz}}{\partial z} + \phi_y &= 0 \\ \frac{\partial \tau_{zx}}{\partial x} + \frac{\partial \tau_{zy}}{\partial y} + \frac{\partial \sigma_{zz}}{\partial z} + \phi_z &= 0 \end{aligned} \quad (2.75)$$

where σ_{xx} , σ_{yy} , and σ_{zz} are the normal stresses, τ_{xy} , τ_{yx} , τ_{xz} , τ_{zx} , τ_{yz} , and τ_{zy} , are the shear stresses, and ϕ_x , ϕ_y , and ϕ_z are the body forces per unit volume acting along the x , y and z directions respectively. For an isotropic material,

$$\begin{aligned}
\tau_{xy} &= \tau_{yx} \\
\tau_{xz} &= \tau_{zx} \\
\tau_{yz} &= \tau_{zy}
\end{aligned}
\tag{2.76}$$

Thus for a three-dimensional isotropic problem there are only six independent terms,

σ_{xx} , σ_{yy} , σ_{zz} , τ_{xy} , τ_{xz} , and τ_{yz} .

Stress-strain Relations

Hooke's law gives the stress-strain relations for a linearly elastic isotropic three-dimensional solid as,

$$\bar{\sigma} = [R](\bar{\epsilon} - \bar{\epsilon}_o)
\tag{2.77}$$

where $\bar{\sigma}$ is the stress vector,

$$\bar{\sigma} = \begin{Bmatrix} \sigma_{xx} \\ \sigma_{yy} \\ \sigma_{zz} \\ \sigma_{xy} \\ \sigma_{xz} \\ \sigma_{yz} \end{Bmatrix}
\tag{2.78}$$

where $\bar{\epsilon}$ is the strain vector,

$$\bar{\epsilon} = \begin{Bmatrix} \epsilon_{xx} \\ \epsilon_{yy} \\ \epsilon_{zz} \\ \gamma_{xy} \\ \gamma_{xz} \\ \gamma_{yz} \end{Bmatrix}
\tag{2.79}$$

where $\bar{\epsilon}_o$ is the initial strain stress vector given by a temperature differential ΔT , and the coefficient of thermal expansion, α ,

$$\bar{\epsilon}_o = \begin{Bmatrix} \epsilon_{xx_o} \\ \epsilon_{yy_o} \\ \epsilon_{zz_o} \\ \gamma_{xy_o} \\ \gamma_{xz_o} \\ \gamma_{yz_o} \end{Bmatrix} = \alpha \Delta T \begin{Bmatrix} 1 \\ 1 \\ 1 \\ 0 \\ 0 \\ 0 \end{Bmatrix} \quad (2.80)$$

and the matrix $[R]$ is given by,

$$[R] = \begin{bmatrix} A & B & B & 0 & 0 & 0 \\ B & A & B & 0 & 0 & 0 \\ B & B & A & 0 & 0 & 0 \\ 0 & 0 & 0 & C & 0 & 0 \\ 0 & 0 & 0 & 0 & C & 0 \\ 0 & 0 & 0 & 0 & 0 & C \end{bmatrix} \quad (2.81)$$

where,

$$\begin{aligned} A &= \frac{E(1-\nu)}{(1+\nu)(1-2\nu)} \\ B &= \frac{\nu E}{(1+\nu)(1-2\nu)} \\ C &= \frac{E}{2(1+\nu)} \end{aligned} \quad (2.82)$$

E is the Young's modulus of elasticity, and ν is the Poisson's ratio.

Strain-displacement Relations

The deformation of any elastic body under any given loading can be described by three displacement components, u , v , and w , parallel to the x , y , and z directions respectively. The normal strains are given by,

$$\begin{aligned}\epsilon_{xx} &= \frac{\partial u}{\partial x} \\ \epsilon_{yy} &= \frac{\partial v}{\partial y} \\ \epsilon_{zz} &= \frac{\partial w}{\partial z}\end{aligned}\tag{2.83}$$

and the shear strains by,

$$\begin{aligned}\gamma_{xy} &= \frac{\partial u}{\partial y} + \frac{\partial v}{\partial x} \\ \gamma_{xz} &= \frac{\partial u}{\partial z} + \frac{\partial w}{\partial x} \\ \gamma_{yz} &= \frac{\partial v}{\partial z} + \frac{\partial w}{\partial y}\end{aligned}\tag{2.84}$$

Boundary Conditions

The boundary conditions can be either on displacements or on stresses. In this work only boundary conditions on displacements are considered. Displacements of nodes on boundary are set to zero.

Compatibility Equations

A body under a given loading should remain continuous, that is no cracks or gaps should appear in the body. Consequently the deformations field should be continuous and

single-valued. This requires a definite relation between normal and shear strains, the compatibility equations, Eq. (2.85).

$$\begin{aligned}
\frac{\partial^2 \varepsilon_{xx}}{\partial y^2} + \frac{\partial^2 \varepsilon_{yy}}{\partial x^2} &= \frac{\partial^2 \gamma_{xy}}{\partial x \partial y} \\
\frac{\partial^2 \varepsilon_{yy}}{\partial z^2} + \frac{\partial^2 \varepsilon_{zz}}{\partial y^2} &= \frac{\partial^2 \gamma_{yz}}{\partial y \partial z} \\
\frac{\partial^2 \varepsilon_{zz}}{\partial x^2} + \frac{\partial^2 \varepsilon_{xx}}{\partial z^2} &= \frac{\partial^2 \gamma_{xz}}{\partial x \partial z} \\
\frac{1}{2} \frac{\partial}{\partial x} \left(\frac{\partial \gamma_{xy}}{\partial z} - \frac{\partial \gamma_{yz}}{\partial x} + \frac{\partial \gamma_{xz}}{\partial y} \right) &= \frac{\partial^2 \varepsilon_{xx}}{\partial y \partial z} \\
\frac{1}{2} \frac{\partial}{\partial y} \left(\frac{\partial \gamma_{xy}}{\partial z} + \frac{\partial \gamma_{yz}}{\partial x} - \frac{\partial \gamma_{xz}}{\partial y} \right) &= \frac{\partial^2 \varepsilon_{yy}}{\partial x \partial z} \\
\frac{1}{2} \frac{\partial}{\partial z} \left(-\frac{\partial \gamma_{xy}}{\partial z} + \frac{\partial \gamma_{yz}}{\partial x} + \frac{\partial \gamma_{xz}}{\partial y} \right) &= \frac{\partial^2 \varepsilon_{zz}}{\partial x \partial y}
\end{aligned} \tag{2.85}$$

Principle of minimum potential energy

The principle of minimum potential energy states that: “Of all possible displacement states a body can assume which satisfy the compatibility equations and boundary conditions, the state which satisfies the equilibrium equations makes the potential energy assume a minimum value.”

The potential energy, Π , of an elastic body is given by,

$$\Pi = \Lambda - \Psi \tag{2.86}$$

where Λ is the strain energy and Ψ is the work done on the body by external forces.

If the energies are expressed as functions of u , v , and w , then at equilibrium the principle of the minimum potential energy yields,

$$\Pi(u, v, w) = \Lambda(u, v, w) - \Psi(u, v, w) = 0 \tag{2.87}$$

The strain energy of a linear elastic body is defined as

$$A = \frac{1}{2} \int_{\Omega} \bar{\epsilon}^T \bar{\sigma} d\Omega \quad (2.88)$$

where Ω designates the volume of the body. From the stress-strain relations of Eq. (2.77), and assuming initial strains are present, Eq. (2.88) yields,

$$A = \frac{1}{2} \int_{\Omega} \bar{\epsilon}^T [R] \bar{\epsilon} d\Omega - \int_{\Omega} \bar{\epsilon}^T [R] \bar{\epsilon}_o d\Omega \quad (2.89)$$

The work done by external forces is given by,

$$\Psi = \int_{\Omega} \bar{\phi}^T \bar{U} \cdot d\Omega + \int_{\Gamma} \bar{\Phi}^T \bar{U} \cdot d\Gamma \quad (2.90)$$

where $\bar{\phi}$ is the vector of known body forces, $\bar{\Phi}$ is the vector of surface forces or tractions, \bar{U} is the vector of displacements and Γ is the surface where the forces are applied. Thus,

$$\Pi = \frac{1}{2} \int_{\Omega} \bar{\epsilon}^T [R] (\bar{\epsilon} - 2\bar{\epsilon}_o) d\Omega - \int_{\Omega} \bar{\phi}^T \bar{U} \cdot d\Omega - \int_{\Gamma} \bar{\Phi}^T \bar{U} \cdot d\Gamma \quad (2.91)$$

Using the variational method, a simple form of the variation of the displacement field is assumed within each element and the conditions that will minimize the functional are derived. In this case the functional is given by Π .

Finite Element Equations

The displacement field within an element is given by,

$$\bar{U} = \begin{Bmatrix} u \\ v \\ w \end{Bmatrix} = [N] \bar{Q}^{(e)} \quad (2.92)$$

where $[N]$ is the matrix of shape functions given by Eq. (2.40), and $\bar{Q}^{(e)}$ is the vector of nodal displacement degrees of freedom of element 'e' given by Eq. (2.39).

The strain vector of Eq. (2.79), using Eqs. (2.83) and (2.84) can be given by,

$$\bar{\epsilon} = [B]\bar{Q}^{(e)} \quad (2.93)$$

where,

$$[B] = \begin{bmatrix} \frac{\partial}{\partial x} & 0 & 0 \\ 0 & \frac{\partial}{\partial y} & 0 \\ 0 & 0 & \frac{\partial}{\partial z} \\ \frac{\partial}{\partial y} & \frac{\partial}{\partial x} & 0 \\ \frac{\partial}{\partial z} & 0 & \frac{\partial}{\partial x} \\ 0 & \frac{\partial}{\partial z} & \frac{\partial}{\partial y} \end{bmatrix} [N] \quad (2.94)$$

thus,

$$[B]^T = \frac{1}{6V} \begin{bmatrix} b_1 & 0 & 0 & c_1 & d_1 & 0 \\ b_2 & 0 & 0 & c_2 & d_2 & 0 \\ b_3 & 0 & 0 & c_3 & d_3 & 0 \\ b_4 & 0 & 0 & c_4 & d_4 & 0 \\ 0 & c_1 & 0 & b_1 & 0 & d_1 \\ 0 & c_2 & 0 & b_2 & 0 & d_2 \\ 0 & c_3 & 0 & b_3 & 0 & d_3 \\ 0 & c_4 & 0 & b_4 & 0 & d_4 \\ 0 & 0 & d_1 & 0 & b_1 & c_1 \\ 0 & 0 & d_2 & 0 & b_2 & c_2 \\ 0 & 0 & d_3 & 0 & b_3 & c_3 \\ 0 & 0 & d_4 & 0 & b_4 & c_4 \end{bmatrix} \quad (2.95)$$

The stresses then can be expressed as

$$\bar{\sigma} = [R](\bar{\epsilon} - \bar{\epsilon}_o) = [R][B]\bar{Q}^{(e)} - [R]\bar{\epsilon}_o \quad (2.96)$$

The potential energy can be expressed in terms of the element potential energies as

$$\Pi = \sum_{e=1}^{nel} \Pi^{(e)} \quad (2.97)$$

where,

$$\begin{aligned} \Pi^{(e)} = & \frac{1}{2} \int_{\Omega^{(e)}} \bar{Q}^{(e)T} [B]^T [R][B]\bar{Q}^{(e)} d\Omega^{(e)} - \int_{\Omega^{(e)}} \bar{Q}^{(e)T} [B]^T [R]\bar{\epsilon}_o d\Omega^{(e)} \\ & - \int_{\Omega^{(e)}} \bar{Q}^{(e)T} [N]^T \bar{\phi} d\Omega^{(e)} - \int_{\Gamma^{(e)}} \bar{Q}^{(e)T} [N]^T \bar{\Phi} d\Gamma^{(e)} \end{aligned} \quad (2.98)$$

Thus,

$$\begin{aligned} \Pi = & \frac{1}{2} \bar{Q}^T \left(\sum_{e=1}^{nel} \int_{\Omega^{(e)}} [B]^T [R][B] d\Omega^{(e)} \right) \bar{Q} - \bar{Q}^T \sum_{e=1}^{nel} \left(\int_{\Omega^{(e)}} [B]^T [R]\bar{\epsilon}_o d\Omega^{(e)} \right. \\ & \left. - \int_{\Omega^{(e)}} [N]^T \bar{\phi} d\Omega^{(e)} - \int_{\Gamma^{(e)}} [N]^T \bar{\Phi} d\Gamma^{(e)} \right) \end{aligned} \quad (2.99)$$

where,

$$\bar{Q} = \begin{Bmatrix} Q_1 \\ Q_2 \\ \vdots \\ Q_m \end{Bmatrix} \quad (2.100)$$

and,

$$m = \text{degrees of freedom} \times \text{no. of nodes} \quad (2.101)$$

The static equilibrium configuration of the body is found by solving the following necessary condition for the minimization of the functional, Π ,

$$\frac{\partial \Pi}{\partial \bar{Q}} = \bar{0} \quad (2.102)$$

This leads to

$$[K]\bar{Q} = \bar{P} \quad (2.103)$$

where $[K]$ is the global stiffness matrix,

$$[K] = \sum_{e=1}^{nel} [K^{(e)}] \quad (2.104)$$

and \bar{P} is the global nodal vector

$$\bar{P} = \sum_{e=1}^{nel} \bar{P}_t^{(e)} + \sum_{e=1}^{nel} \bar{P}_s^{(e)} + \sum_{e=1}^{nel} \bar{P}_b^{(e)} \quad (2.105)$$

The element stiffness matrix, $[K^{(e)}]$, is given by

$$[K^{(e)}] = \int_{\Omega^{(e)}} [B]^T [R][B] d\Omega^{(e)} \quad (2.106)$$

The element load vector due to thermal strains, $\bar{P}_t^{(e)}$, is given by

$$\bar{P}_t^{(e)} = \int_{\Omega^{(e)}} [B]^T [R] \bar{\epsilon}_o d\Omega^{(e)} \quad (2.107)$$

The element load vector due to surface forces, $\bar{P}_s^{(e)}$, is given by

$$\bar{P}_s^{(e)} = \int_{\Gamma^{(e)}} [N]^T \bar{\Phi} d\Gamma^{(e)} \quad (2.108)$$

The element load vector due to body forces, $\bar{P}_b^{(e)}$, is given by

$$\bar{P}_b^{(e)} = \int_{\Omega^{(e)}} [N]^T \bar{\varphi} d\Omega^{(e)} \quad (2.109)$$

From the theories presented in Sections 2.3.1 and 2.3.2 it can be readily shown that,

$$[K^{(e)}] = V^{(e)} [B]^T [R] [B] \quad (2.110)$$

and

$$\bar{P}_t^{(e)} = \frac{E \alpha V^{(e)}}{(1-2\nu)} \cdot (T_{avg}^{(e)} - T_{ref}) \cdot [B]^T \cdot \begin{Bmatrix} 1 \\ 1 \\ 1 \\ 0 \\ 0 \\ 0 \end{Bmatrix} \quad (2.111)$$

where $V^{(e)}$ is the volume of element 'e', $T_{avg}^{(e)}$ is the average of the nodal temperatures of element 'e', and T_{ref} is the reference (strain-free) temperature.

Let the body force vector $\bar{\varphi} = \begin{Bmatrix} \varphi_x \\ \varphi_y \\ \varphi_z \end{Bmatrix}$, and the surface force vector $\bar{\Phi} = \begin{Bmatrix} p_x \\ p_y \\ p_z \end{Bmatrix}$, then

$$\bar{P}_b^{(e)} = \frac{V^{(e)}}{4} \begin{Bmatrix} \varphi_x \\ \varphi_x \\ \varphi_x \\ \varphi_x \\ \varphi_y \\ \varphi_y \\ \varphi_y \\ \varphi_y \\ \varphi_z \\ \varphi_z \\ \varphi_z \\ \varphi_z \end{Bmatrix} \quad (2.112)$$

and,

$$\bar{P}_s^{(e)} = \frac{A_{123}^{(e)}}{3} \begin{Bmatrix} p_x \\ p_x \\ p_x \\ 0 \\ p_y \\ p_y \\ p_y \\ 0 \\ p_z \\ p_z \\ p_z \\ 0 \end{Bmatrix} \quad (2.113)$$

$A_{123}^{(e)}$ is the area of face 1-2-3 of element 'e'. The fourth, eighth and twelfth entries of the vector in Eq. (2.113) are zero as they correspond N_4 which is zero on face 1-2-3. Eq. (2.113) takes another three forms corresponding to faces 2, 3, and 4.

2.4.3 Reynolds Lubrication Equation

The Reynolds lubrication equation is derived from the Navier-Stokes equations under the assumptions that:

- i. The fluid is assumed to be Newtonian, with direct proportionality between shear stress and shearing velocity
- ii. The fluid is incompressible
- iii. The flow is laminar
- iv. Inertia and body terms are assumed to be negligible compared to the viscous terms
- v. Variation of pressure across the film is assumed to be negligibly small so that $P = P(x, y)$ only
- vi. The curvature effects are negligible, that is the height of the lubricant film is much smaller than the length or the width of the body
- vii. The viscosity does not depend on pressure but can be affected by temperature
- viii. The motion of the lubricant fluid normal to the surface can be neglected compared to the motion parallel to the surface.

These assumptions yield the most commonly encountered form of the Reynolds equation,

$$\frac{\partial}{\partial x} \left(\frac{h^3}{12\mu} \frac{\partial P}{\partial x} \right) + \frac{\partial}{\partial y} \left(\frac{h^3}{12\mu} \frac{\partial P}{\partial y} \right) = \frac{1}{2} V \frac{\partial h}{\partial y} + \frac{\partial h}{\partial t} \quad (2.114)$$

This equation describes the pressure field of the flow between two bodies with impermeable walls as shown in Figure 2.9. The first term on the right hand side accounts

for the physical wedge and $\partial h/\partial t = \dot{h}$ accounts for the squeeze film. h is the separation of the two bodies and μ is the viscosity of the fluid.

V is the relative velocity given by

$$V = V_a - V_b \quad (2.115)$$

For a positive pressure field the right hand side of Eq. (2.114) must be less than zero.

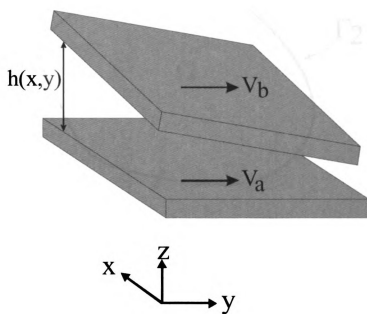


Figure 2.9: Body and coordinate system for Reynolds lubrication equation

Finite Element Equations

For the derivation of the finite element equations of the Reynolds lubrication equation the Galerkin method is used. Consider an arbitrary two-dimensional fluid film as in Figure 2.10, governed by Eq. (2.114), and with boundary conditions

$$P = \bar{P} \text{ on } \Gamma_1 \quad (2.116)$$

and

$$\left[\bar{V} h - \frac{h^3}{12\mu} \nabla P \right] \cdot \bar{n} = q \text{ on } \Gamma_2 \quad (2.117)$$

where \bar{P} is the prescribed pressure on Γ_1 , q is the normal flow across the boundary Γ_2 , \bar{n} is the unit outward normal to Γ_2 , and $\bar{V} = V \hat{j}$.

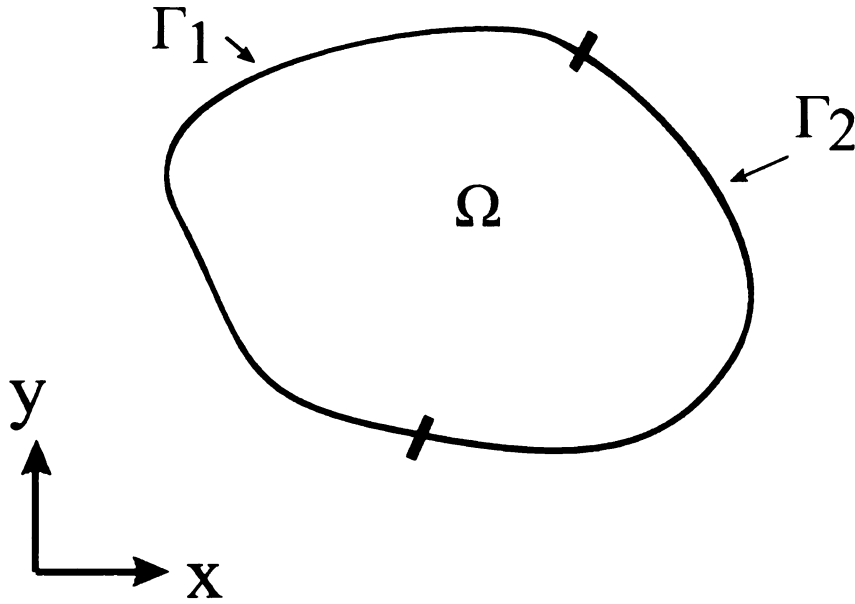


Figure 2.10: 2D arbitrary body

Eq. (2.114) can be rewritten as

$$\nabla \left(\frac{h^3}{12\mu} \nabla P \right) = \frac{1}{2} V \frac{\partial h}{\partial y} + \frac{\partial h}{\partial t} \quad (2.118)$$

From assumption (vi) above, Eq. (2.118) can be rewritten as

$$\frac{h^3}{12\mu} \nabla^2 P = \frac{1}{2} V \frac{\partial h}{\partial y} + \frac{\partial h}{\partial t} \quad (2.119)$$

Now multiplying by the weight function and integrating over the domain,

$$\int_{\Omega^{(e)}} \frac{h^3}{12\mu} \nabla^2 P \omega d\Omega^{(e)} = \int_{\Omega^{(e)}} \left(\frac{1}{2} V \frac{\partial h}{\partial y} + \frac{\partial h}{\partial t} \right) \omega d\Omega^{(e)} \quad (2.120)$$

Using Green's first identity,

$$\int_{\Omega} (\nabla P \cdot \nabla \omega + \omega \nabla^2 P) d\Omega = \int_{\Gamma} (\omega \nabla P) \cdot \bar{n} d\Gamma \quad (2.121)$$

and Green-Gauss theorem

$$\int_{\Omega} \frac{\partial h}{\partial y} \omega d\Omega = - \int_{\Omega} h \frac{\partial \omega}{\partial y} d\Omega + \int_{\Omega} h \omega n_y d\Omega \quad (2.122)$$

then Eq. (2.120) becomes

$$\begin{aligned} \int_{\Omega^{(e)}} \left(\frac{h^3}{12\mu} \nabla P \cdot \nabla \omega \right) d\Omega^{(e)} &= \int_{\Omega^{(e)}} \left(\frac{1}{2} V h \frac{\partial \omega}{\partial y} - \frac{\partial h}{\partial t} \omega \right) d\Omega^{(e)} \\ &\quad - \int_{\Gamma^{(e)}} q \omega d\Gamma^{(e)} \end{aligned} \quad (2.123)$$

If there is no flow across the boundary Γ_2 , that is $q = 0$, and only the prescribed pressure boundary condition is true, then $\int_{\Gamma^{(e)}} q \omega d\Gamma^{(e)} = 0$, thus Eq. (2.123) reduces to

$$\int_{\Omega^{(e)}} \left(\frac{h^3}{12\mu} \nabla P \cdot \nabla \omega \right) d\Omega^{(e)} = \frac{1}{2} V \int_{\Omega^{(e)}} h \frac{\partial \omega}{\partial y} d\Omega^{(e)} - \int_{\Omega^{(e)}} \frac{\partial h}{\partial t} \omega d\Omega^{(e)} \quad (2.124)$$

Now by approximating,

$$P = P_i N_i \quad (2.125)$$

$$h = h_i N_i \quad (2.126)$$

$$\frac{\partial h}{\partial t} = \dot{h} = \dot{h}_i N_i \quad (2.127)$$

and

$$\omega_j = N_j \quad (2.128)$$

leads to

$$\int_{\Omega^{(e)}} \left(\frac{(h_i N_i)^3}{12\mu} \nabla N_i \cdot \nabla N_j \right) d\Omega^{(e)} \bar{p}^{(e)} = \frac{1}{2} V \int_{\Omega^{(e)}} (h_i N_i) \frac{\partial N_j}{\partial y} d\Omega^{(e)} - \int_{\Omega^{(e)}} (\dot{h}_i N_i) \omega d\Omega^{(e)} \quad (2.129)$$

where $\bar{p}^{(e)}$ is the vector of nodal pressures of element 'e.' Eq. (2.129) can readily be written as

$$\left[K^{(e)} \right] \bar{p}^{(e)} = \bar{F}_v^{(e)} + \bar{F}_h^{(e)} \quad (2.130)$$

where,

$$\left[K^{(e)} \right] = \int_{\Omega^{(e)}} \left(\frac{(h_i N_i)^3}{12\mu} \left(\frac{\partial N_i}{\partial x} \frac{\partial N_j}{\partial x} + \frac{\partial N_i}{\partial x} \frac{\partial N_j}{\partial x} \right) \right) d\Omega^{(e)} \quad (2.131)$$

$$\bar{F}_v^{(e)} = \frac{1}{2} V \int_{\Omega^{(e)}} (h_i N_i) \frac{\partial N_j}{\partial y} d\Omega^{(e)} \quad (2.132)$$

and,

$$\bar{F}_h^{(e)} = - \int_{\Omega^{(e)}} (\dot{h}_i N_i) \omega d\Omega^{(e)} \quad (2.133)$$

Assemblage of the element equations leads to

$$[K]\bar{P} = \bar{F} \quad (2.134)$$

where the global stiffness matrix $[K]$ is

$$[K] = \sum_{e=1}^{nel} [K^{(e)}] \quad (2.135)$$

the global load vector \bar{F} is

$$\bar{F} = \sum_{e=1}^{nel} (\bar{F}_v^{(e)} + \bar{F}_h^{(e)}) \quad (2.136)$$

and,

$$\bar{P} = \begin{Bmatrix} P_1 \\ P_2 \\ \vdots \\ P_m \end{Bmatrix} \quad (2.137)$$

where

$$m = \text{no. of nodes}$$

Now from the theories developed in Section 2.3.1 for a linear triangular element, Eqs. (2.131) to (2.133) can be expressed as

$$[K^{(e)}] = \frac{A^{(e)}}{60 \times 12 \times \mu} (b_i b_j + c_i c_j) \begin{Bmatrix} h_1^3 \\ 3h_1^2 h_2 \\ 3h_1 h_2^2 \\ h_2^3 \\ 3h_1^2 h_3 \\ 6h_1 h_2 h_3 \\ 3h_2^2 h_3 \\ 3h_1 h_3^2 \\ 3h_2 h_3^2 \\ h_3^3 \end{Bmatrix}^T \cdot \begin{Bmatrix} 6 \\ 2 \\ 2 \\ 6 \\ 2 \\ 1 \\ 2 \\ 2 \\ 2 \\ 6 \end{Bmatrix} \quad (2.138)$$

$$\bar{F}_v^{(e)} = \frac{V A^{(e)}}{6} h_i c_j \begin{Bmatrix} 1 \\ 1 \\ 1 \end{Bmatrix} \quad (2.139)$$

$$\bar{F}_h^{(e)} = -\frac{A^{(e)}}{12} \begin{bmatrix} 2 & 1 & 1 \\ 1 & 2 & 1 \\ 1 & 1 & 2 \end{bmatrix} h_i \quad (2.140)$$

2.4.4 Incorporation of Boundary Conditions

After assembling the element stiffness matrix and the element load vectors the system of equations can be written as,

$$[K] \bar{\Phi} = \bar{P} \quad (2.141)$$

However $[K]$ will be singular hence its inverse does not exist and thus the system cannot be solved for $\bar{\Phi}$. In the case of static analysis, the physical meaning of this is that the body is free to undergo unlimited rigid body motion unless some support constraints

are provided to keep the body in equilibrium. Thus the prescribed boundary conditions for a given problem are applied to Eq. (2.141) before solving for $\bar{\Phi}$.

If Φ_j is prescribed as Φ_j^* , the load vector \bar{P} is modified as

$$P_i = P_i - K_{ij}\Phi_j^* \quad (2.142)$$

for $i = 1, 2, \dots, m$

The rows and columns of $[K]$ corresponding to Φ_j are made zero, and the diagonal term is set to one.

$$K_{ij} = K_{ji} = 0 \quad (2.143)$$

for $i = 1, 2, \dots, m$

and

$$K_{jj} = 1 \quad (2.144)$$

Finally the prescribed value of Φ_j^* is inserted into the load vector,

$$P_j = \Phi_j^* \quad (2.145)$$

2.4.5 Guyan Reduction

The Guyan reduction method [20], also known as static condensation, eliminates the unwanted degrees of freedom of a system, thus reducing its overall size and consequently decreasing solution time. Given a system,

$$\begin{matrix} [K] & \cdot & \bar{X} & = & \bar{P} \\ n \times n & & n \times 1 & & n \times 1 \end{matrix} \quad (2.146)$$

where n is the number of degrees of freedom, decomposing it,

$$\left[\begin{array}{c|c} K_{11} & K_{12} \\ \hline p \times p & p \times q \end{array} \right] \left\{ \begin{array}{c} \bar{X}_1 \\ \hline p \times 1 \\ \bar{X}_2 \\ \hline q \times 1 \end{array} \right\} = \left\{ \begin{array}{c} \bar{P}_1 \\ \hline p \times 1 \\ \bar{P}_2 \\ \hline q \times 1 \end{array} \right\} \quad (2.147)$$

where

$$q + p = n \quad (2.148)$$

Now if \bar{X}_2 is the vector of unwanted degrees of freedom, then the above system can be reduced to,

$$\left[K_{11} - K_{12}K_{22}^{-1}K_{21} \right] \bar{X}_1 = \bar{P}_1 \quad (2.149)$$

where the reduced matrix, $[K_{red}]$, is given by,

$$[K_{red}] = \left[K_{11} - K_{12}K_{22}^{-1}K_{21} \right] \quad (2.150)$$

The compliance matrix, $[C]$ is given by,

$$[C] = [K_{red}]^{-1} \quad (2.151)$$

Also if \bar{X}_2 , the deformation of the rest of the body, is needed then,

$$\bar{X}_2 = \left[-K_{22}^{-1}K_{21} \right] \bar{X}_1 \quad (2.152)$$

where the coordinate transformation matrix, $[T]$ is defined as,

$$[T] = \left[-K_{22}^{-1}K_{21} \right] \quad (2.153)$$

When the stiffness matrix of a static problem is reduced no information is lost. It can be seen from Eq. (2.150) that all the elements contribute to the reduced matrix.

2.4.6 Conjugate Gradient Method

The conjugate gradient method is an iterative method for the solution of systems of equations. The method cannot compete with direct methods, like solution by matrix inversion, for small systems. However its strength is revealed with large, sparse systems. A sparse system is one where most elements of the square matrix are zeros. For such matrices only the non-zero elements can be stored thus saving storage space. Typically a matrix is considered sparse if its density is less than 10%. Figure 2.11 shows a graphical representation of the population of a stiffness matrix obtained from a piston thermal analysis. The total size of the matrix is 1034^2 , with 11338 non-zero elements. The density of this matrix is 1.06%. Huge computational effort would be required to invert it, but a solution for the system can easily be obtained using the conjugate gradient method.

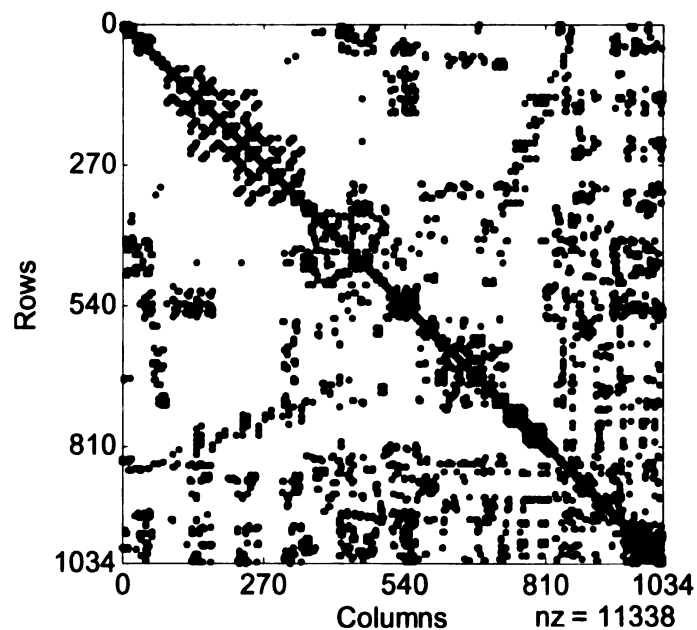


Figure 2.11: Graphical representation of the population of a sparse matrix.

Now consider the following function,

$$f(\bar{x}) = \frac{1}{2} \bar{x}^T [A] \bar{x} - \bar{x}^T \bar{b} \quad (2.154)$$

The imposed is to find a vector \bar{x} that minimizes the scalar function $f(\bar{x})$. The function is minimized when its gradient is equal to zero, that is

$$\nabla f = [A] \bar{x} - \bar{b} = 0 \quad (2.155)$$

This is equivalent to solving

$$[A] \bar{x} = \bar{b} \quad (2.156)$$

The gradient method achieves minimization by iteration. An initial guess for the vector \bar{x} is required, \bar{x}_1 , and each subsequent iteration computes a refined solution

$$\bar{x}_{i+1} = \bar{x}_i + \lambda_i \bar{s}_i \quad (2.157)$$

where i is the iteration number, λ is the step length and \bar{s} is the search direction. Eq. (2.157) must satisfy Eq. (2.156), that is

$$[A](\bar{x}_i + \lambda_i \bar{s}_i) = \bar{b} \quad (2.158)$$

Now let the residual of each iteration be

$$\bar{r}_i = \bar{b} - [A] \bar{x}_i \quad (2.159)$$

then Eq. (2.158) becomes

$$\lambda_i [A] \bar{s}_i = \bar{r}_i \quad (2.160)$$

which readily leads to

$$\lambda_i = \frac{\bar{s}_i^T \bar{r}_i}{\bar{s}_i^T [A] \bar{s}_i} \quad (2.161)$$

The search direction is chosen by intuition to be equal to the residual as it gives the largest negative change in $f(\bar{x})$,

$$\bar{s}_i = -\nabla f = \bar{r}_i \quad (2.162)$$

This is known as the method of steepest descent. It is not a very popular method as it converges relatively slowly. The faster conjugate gradient method utilizes a modified search direction given by

$$\bar{s}_{i+1} = \bar{r}_{i+1} + \beta_i \bar{s}_i \quad (2.163)$$

The constant β is chosen so that two successive search directions are conjugate to each other, that is

$$\bar{s}_{i+1}^T [A] \bar{s}_i = 0 \quad (2.164)$$

From Eq. (2.163)

$$\left(\bar{r}_{i+1}^T + \beta_i \bar{s}_i^T \right) [A] \bar{s}_i = 0 \quad (2.165)$$

which yields,

$$\beta_i = -\frac{\bar{r}_{i+1}^T [A] \bar{s}_i}{\bar{s}_i^T [A] \bar{s}_i} \quad (2.166)$$

The conjugate gradient method is a very efficient algorithm thus making it very popular for solving large systems. This method is used in this work for the solution of the systems of equations developed by the finite element formulation. Figure 2.12 outlines the conjugate gradient algorithm.

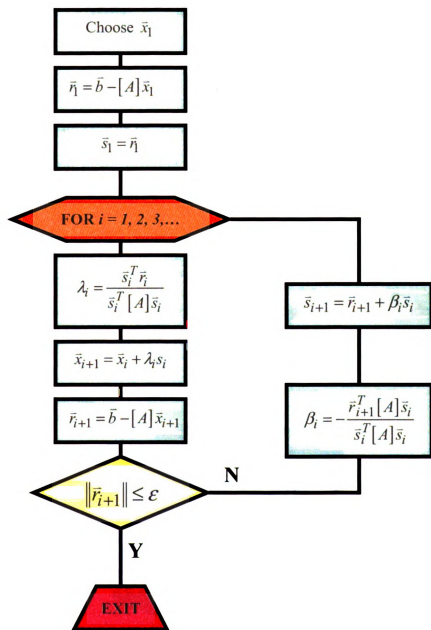


Figure 2.12: Conjugate gradient method flowchart

CHAPTER 3

ENGINE OPERATING PARAMETERS

3.1 Introduction

This chapter introduces the engine operating parameters used in this work. The derivation of time step, piston position, piston speed, and piston acceleration is achieved from the engine geometry and engine operating conditions. The theory developed in this chapter is from Reference [25].

Figure 3.1 shows the terminology used in this work when referring to different piston areas: the crown, the ring-pack area, the skirt, the pinhole, and the underside.

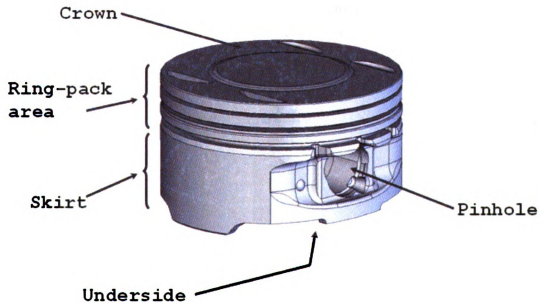


Figure 3.1: Piston terminology

3.2 Time Step

Given a an engine operating at N revolutions per minute (rpm) then the time step, Δt , between successive crank angles is given as,

$$\frac{1}{\Delta t} = N \left[\frac{\text{rev}}{\text{min}} \right] \times \frac{360 \text{ deg}}{1 \text{ rev}} \times \frac{1 \text{ min}}{60 \text{ s}} \quad (3.1)$$

thus,

$$\Delta t = \frac{1}{6N} \quad (3.2)$$

3.3 Angular Speed

Given a an engine operating at N revolutions per minute then the angular speed, ω , is given by

$$\omega = N \left[\frac{\text{rev}}{\text{min}} \right] \times \frac{2\pi}{1 \text{ rev}} \times \frac{1 \text{ min}}{60 \text{ s}} \quad (3.3)$$

thus,

$$\omega = \frac{\pi N}{30} \quad (3.4)$$

3.4 Piston Motion

Given the piston assembly shown in Figure 2.1, the piston position, velocity and acceleration can be readily derived. r is the crankshaft radius, l is the connecting rod length, d is the piston pin offset; θ is the engine crank angle, ω is the angular speed, and ϕ is the angle the connecting rod makes with the piston axis. When $\theta = 0$ the piston is at the top dead centre (TDC) at the beginning of the intake stroke. A four-stroke engine requires

720 deg. for a cycle, where a cycle has four strokes: intake, compression, expansion and exhaust.

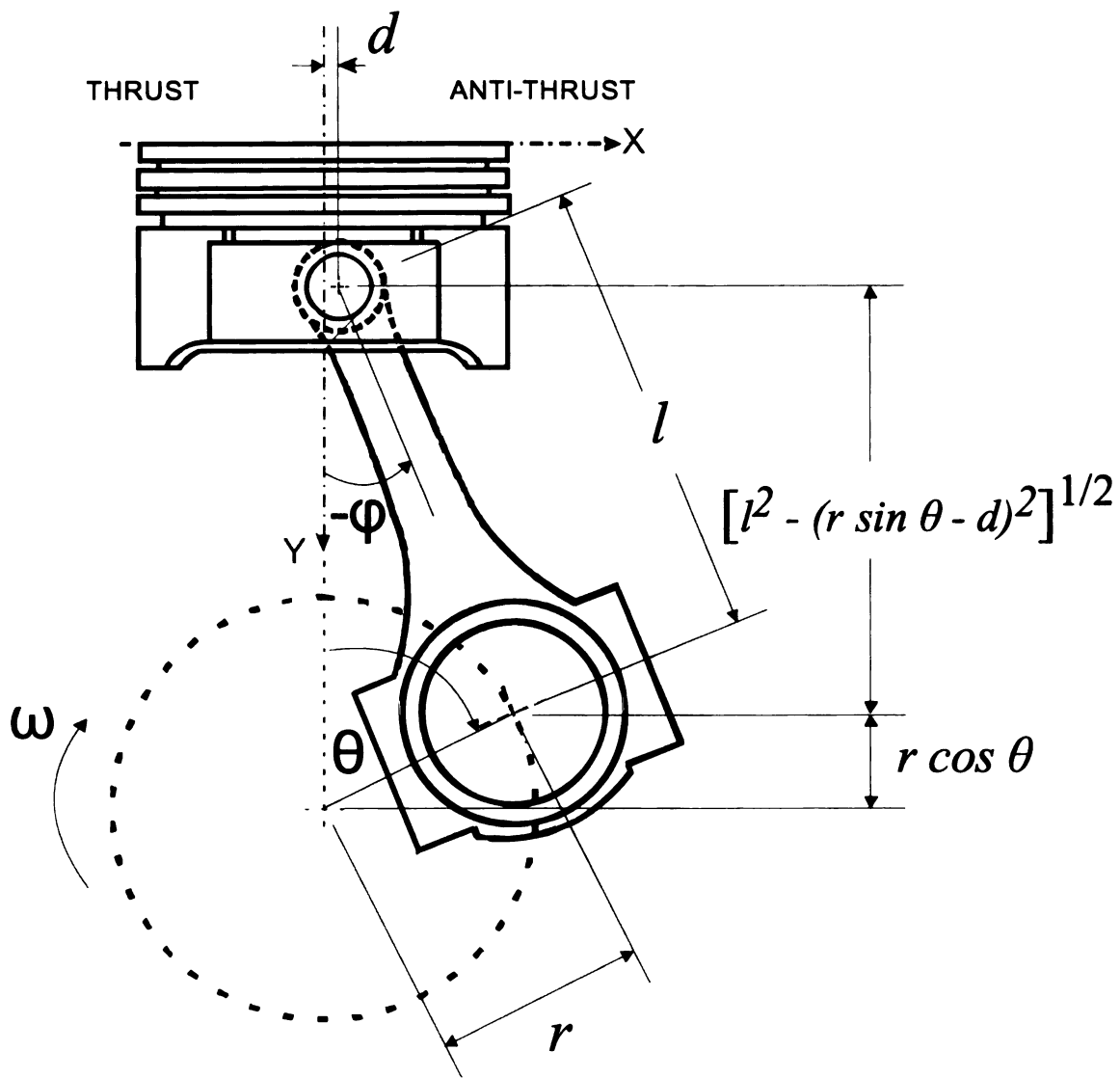


Figure 3.2: Piston assembly

Figure 3.3 shows a schematic of a piston confined within the cylinder bore. The piston position at TDC and bottom dead centre (BDC) can be seen. C is the nominal piston to cylinder bore clearance.

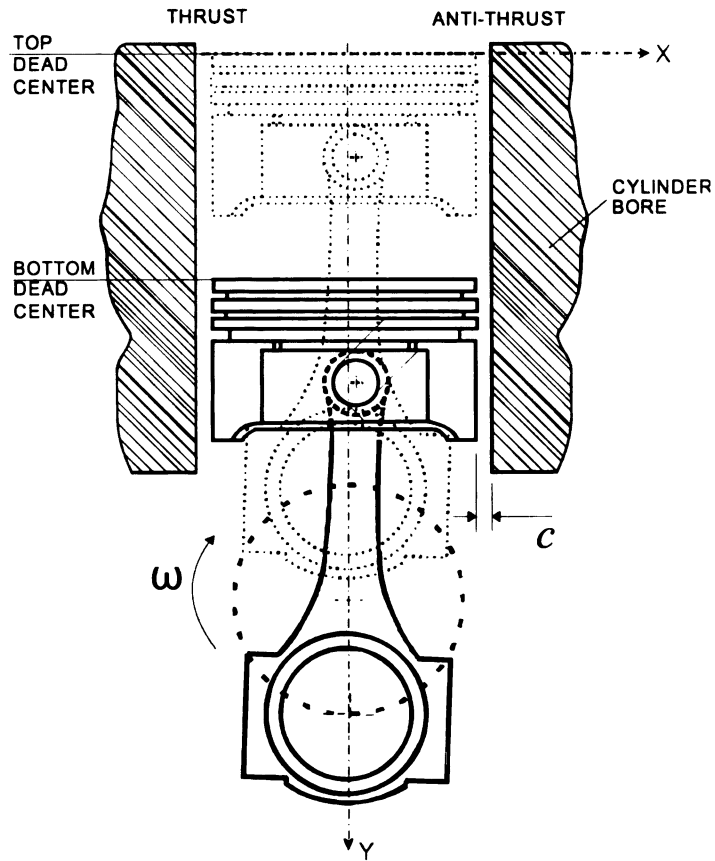


Figure 3.3: Piston position extremities: bottom dead center and top dead center

Now let

$$\theta = \omega t \quad (3.5)$$

so that

$$\frac{d\theta}{dt} = \omega \quad (3.6)$$

The piston position y_p is given by

$$y_p = \sqrt{l^2 - d^2} + r \left(1 - \cos \theta - \frac{l}{r} \sqrt{1 - \left(\frac{r}{l}\right)^2 \left(\sin \theta - \frac{d}{r}\right)^2} \right) \quad (3.7)$$

Eq. (3.7) forces y_p to be zero when the piston is at TDC. It can be easily modified to set y_p to be zero at either mid-stroke or BDC.

The piston speed, v_p , is given by

$$v_p = \frac{dy_p}{d\theta} \cdot \frac{d\theta}{dt}$$

$$= r\omega \left(\sin\theta + \frac{r \cos\theta (\sin\theta - d/r)}{l \sqrt{1 - (r/l)^2 (\sin\theta - d/r)^2}} \right)$$
(3.8)

The piston acceleration, a_p , is given by

$$a_p = \frac{dv_p}{d\theta} \cdot \frac{d\theta}{dt}$$

$$= r\omega^2 \left(\cos\theta + \left(\frac{r}{l}\right)^3 \frac{\cos^2\theta (\sin\theta - d/r)^2}{\left(1 - (r/l)^2 (\sin\theta - d/r)^2\right)^{3/2}} + \left(\frac{r}{l}\right) \frac{\cos^2\theta - \sin\theta (\sin\theta - d/r)}{\sqrt{1 - (r/l)^2 (\sin\theta - d/r)^2}} \right)$$
(3.9)

The angle φ can also be readily derived. From Figure 3.2,

$$l \sin\varphi = r \sin\theta - d$$
(3.10)

thus

$$\varphi = \sin^{-1} \left(\frac{r \sin\theta - d}{l} \right)$$
(3.11)

3.4.1 Sample results

Given the engine geometry and operating conditions of Table 3.1, Figure 3.4 to Figure 3.7 show typical plots of piston position, piston velocity, piston acceleration and angle φ respectively.

Table 3.1: Engine geometry and operating conditions

| | |
|------------------------------|----------|
| Crankshaft radius, r : | 90.60 mm |
| Connecting rod length, l : | 133 mm |
| Piston pin offset, d : | -0.4 mm |
| Engine Speed, N : | 1000 rpm |

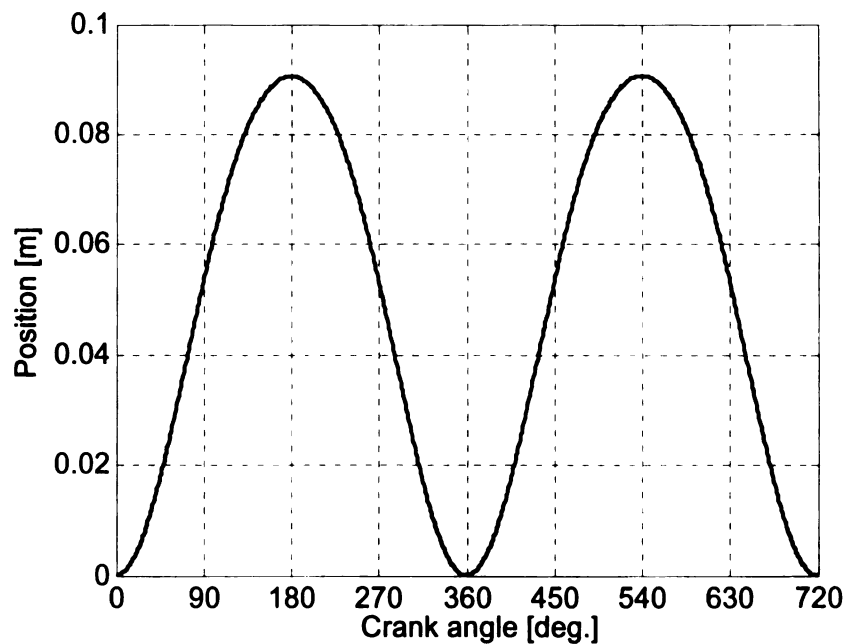


Figure 3.4: Piston position

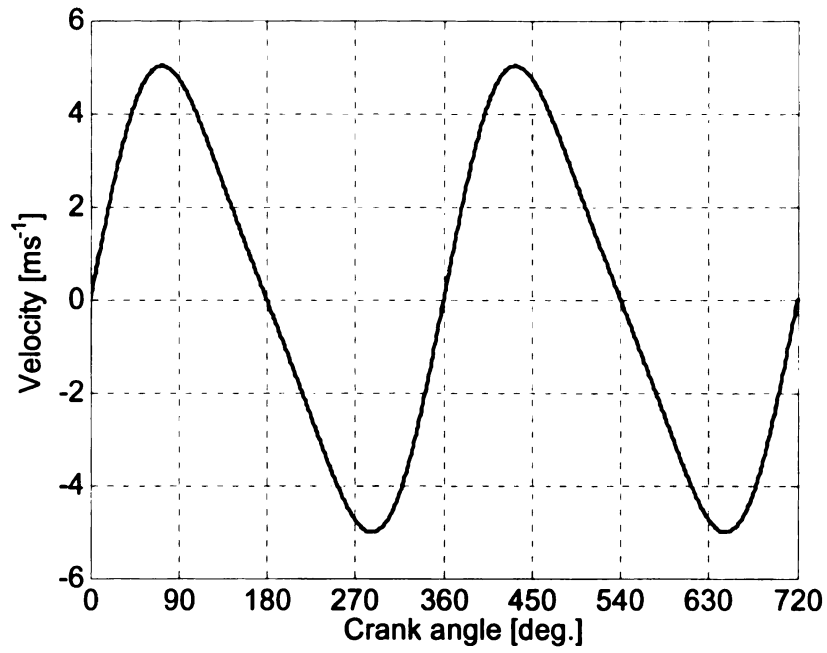


Figure 3.5: Piston velocity

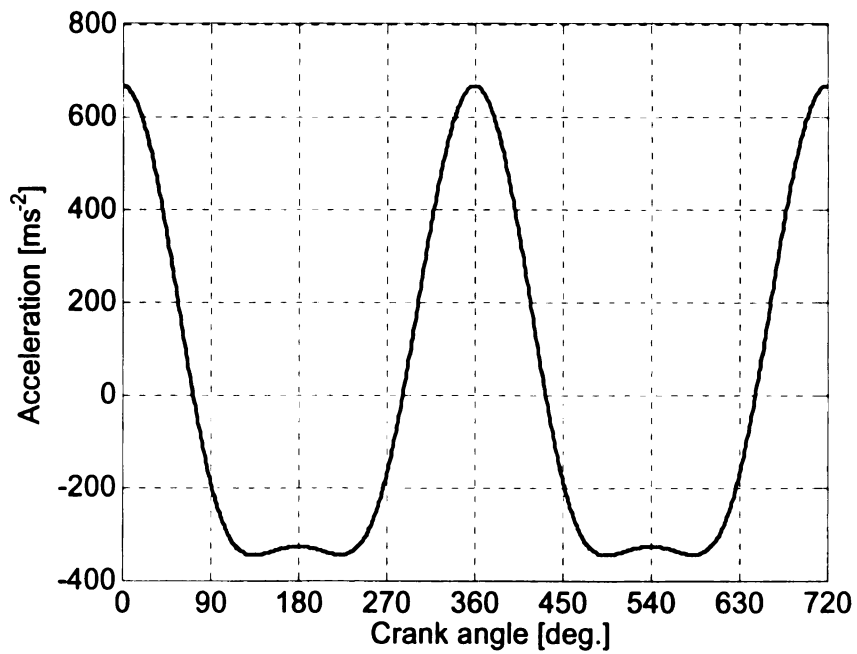


Figure 3.6: Piston acceleration

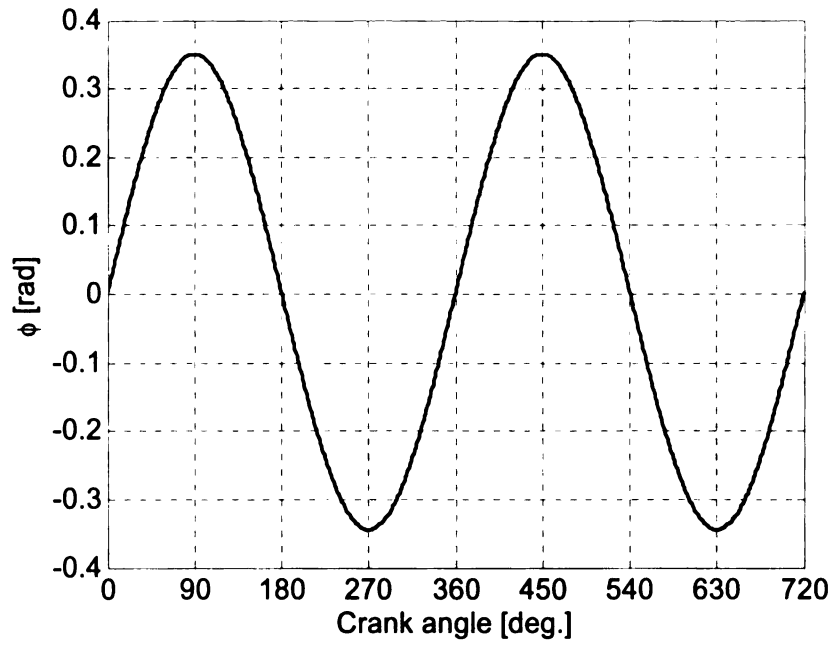


Figure 3.7: Angle ϕ

CHAPTER 4

PARAMETERIZATION AND FEA APPROACH FOR THE ASSESSMENT OF PISTON CHARACTERISTICS

4.1 Introduction

Elastohydrodynamic lubrication, piston dynamics and friction are important characteristics determining the performance and efficiency of an internal combustion engine. This chapter presents a finite element analysis on a production piston of a gasoline engine performed using commercial software, the COSMOSDesignSTAR, and a comprehensive cylinder-kit simulation software, CASE, to demonstrate the advantages of using a reduced, parameterized model analysis in the assessment of piston design characteristics. The full piston model is parameterized according to the CASE specifications. The two are analyzed and compared in the COSMOSDesignSTAR, considering thermal and mechanical loads. The region of interest is the skirt area on the thrust and anti-thrust sides of the piston. The results are compared with the CASE results and a discussion follows on how the piston model simplification approach can help significantly reduce computation time without losing valuable information on piston performance. The piston characteristics are evaluated with the reduced model, thus allowing for a faster analysis and optimization than would be possible with a complete FEA piston model. The results demonstrate that the simplified model agrees qualitatively and quantitatively with the full model; the maximum temperature and calculated distortions on the skirt face are comparable. Computation time difference between the full model and simplified model is not significant for a single analysis; however it

becomes very significant when a cyclical analysis is performed at every crank angle degree.

4.2 Piston model FE analysis

The finite element analysis is performed in COSMOSDesignSTAR, for both full and parameterized piston models. The generated mesh uses tetrahedral elements; Figure 4.1 shows mesh for the full model. A finite element analysis is performed in the CASE as well. It generates a mesh for the parameterized piston using hexahedral and pentahedral elements (Figure 4.2). The parameterization of the piston model is shown in Figure 4.3 and Table 4.1.



Figure 4.1: Full piston model mesh in COSMOSDesignSTAR, (a) top side, (b) underside

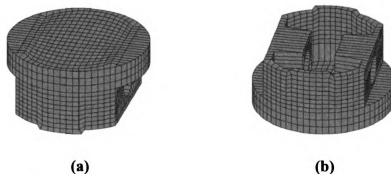


Figure 4.2: Parameterized piston model mesh in CASE, (a) top side, (b) underside

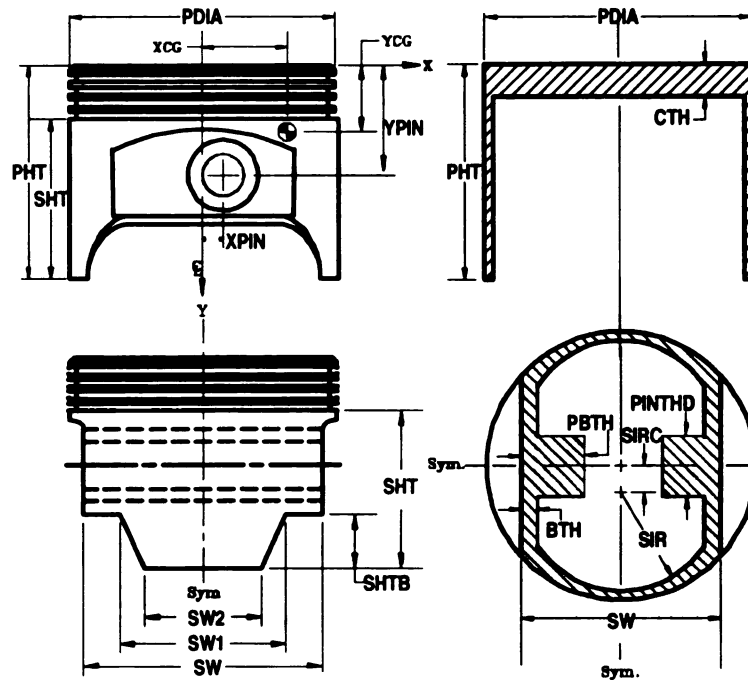


Figure 4.3: Parameterized piston dimensions

Table 4.1: Parameterized piston model feature labels

| | |
|---------|-----------------------------------|
| PDIA: | piston diameter |
| PHT: | piston height |
| SHT: | skirt height |
| CTH: | crown thickness |
| XPIN: | x-coordinate of pin location |
| YPIN: | y-coordinate of pin location |
| XCG: | x-coordinate of center of gravity |
| YCG: | y-coordinate of center of gravity |
| SHTB: | tab height |
| SW: | skirt width |
| SW1: | lower tab width |
| SW2: | upper tab width |
| BTH: | boss thickness |
| PBTH: | pin boss thickness |
| PINTHD: | pin boss width |
| SIR: | inner skirt radius |
| SIRC: | inner skirt radius center |

4.2.1 Thermal Loading

The engine modeled in CASE is a motored optically accessible engine used for experimental oil film thickness measurements. The engine uses a production piston with a sapphire cylinder wall.

The engine was first modeled in Ricardo WAVE to obtain the heat transfer above the piston crown. Figure 4.4 shows pressure traces for the engine, both experimental and from the WAVE model. The engine was run at 1500 rpm with 2 psi boost. The two pressure traces have strong agreement except where the exhaust valve opens. The most crucial part however is at the compression and power strokes. Thus the results from the WAVE model can be considered reliable. Figure 4.5 shows the temperature of the air in the cylinder over one cycle. Figure 4.6 shows the heat transfer coefficient above the piston crown. The heat transfer coefficient is obtained using an advanced combustion module, the IRIS Model in the WAVE.

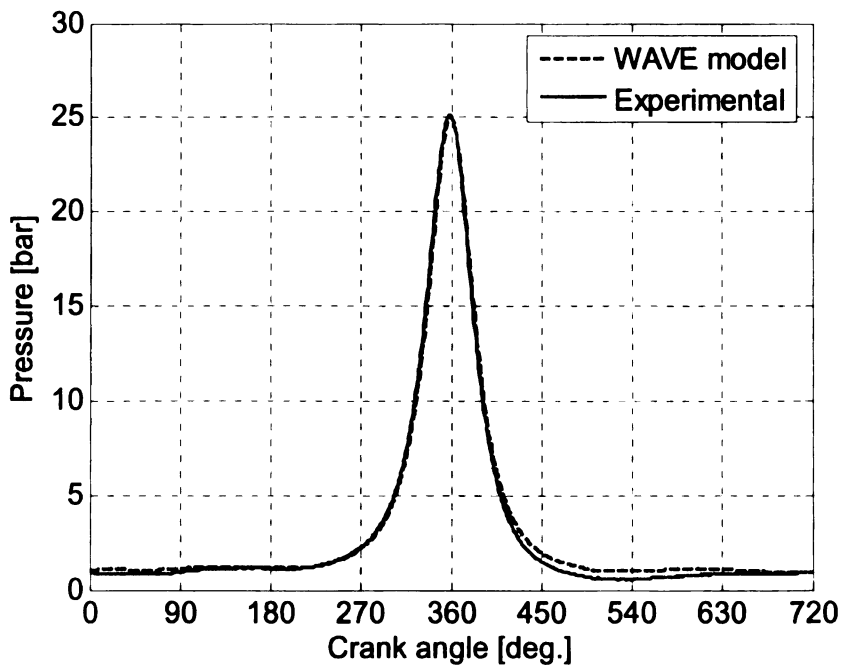


Figure 4.4: Pressure trace of optical engine

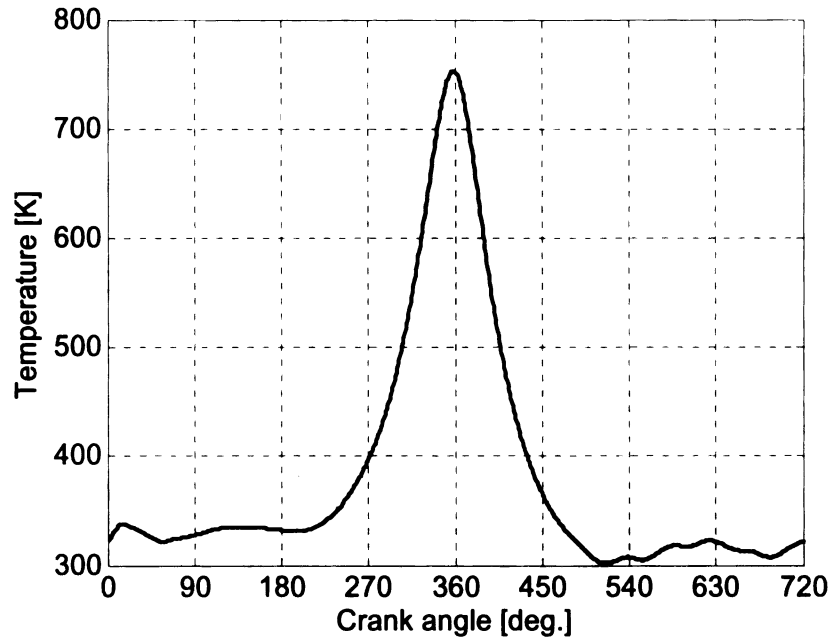


Figure 4.5: In-cylinder air temperature for optical engine

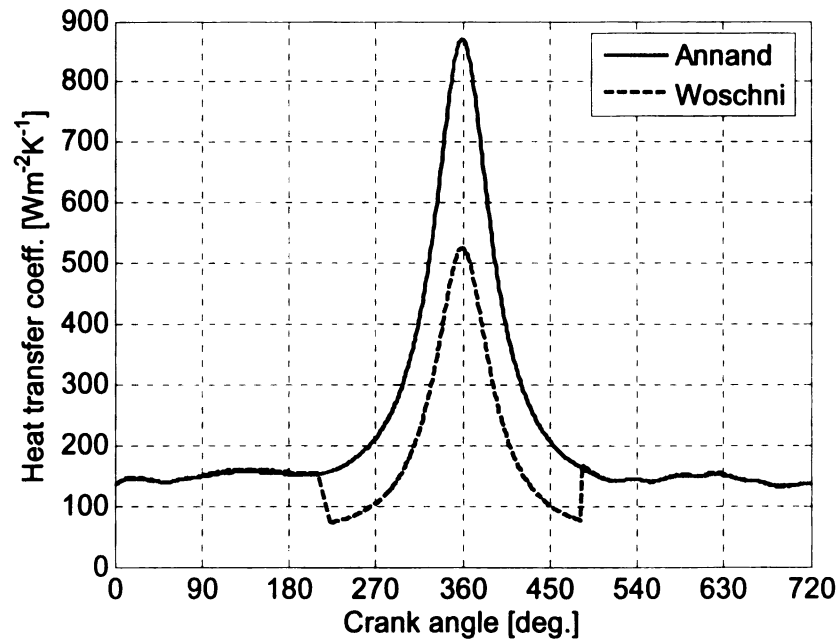


Figure 4.6: Heat transfer coefficient above piston crown using Annand and Woschni correlations

WAVE calculates the heat transfer coefficient using both Annand's [1] and Woschni's [55] correlations. Averaging over the cycle, Eq. (4.1), Annand's correlation suggests a heat transfer coefficient of 230 W/m²K. Similarly Woschni's correlation suggests a value of 170 W/m²K. The average of the two correlations is chosen to be used as the heat transfer coefficient above the piston crown. The mean temperature, Eq. (4.2), is found to be 470 K.

$$\bar{h}_g = \frac{1}{4\pi} \int_0^{4\pi} h_g d\theta \quad (4.1)$$

$$\bar{T}_g = \frac{1}{4\pi \bar{h}_g} \int_0^{4\pi} h_g T_g d\theta \quad (4.2)$$

Woschni [56] solved for the heat transfer coefficients governing a piston using numerical method and the electrolytic tank analog. His results suggest an average heat transfer coefficient of 460 W/m²K above the crown, in the range of 1000 – 1900 W/m²K in the ring groove area, 220 – 930 W/m²K at the land area, 550 – 720 W/m²K at the piston skirt and 100 – 1300 W/m²K on the piston underside. Similar values are used by Li [35].

In the study of the parameterized piston, the heat transfer coefficients are assumed constant in each area and within Woschni's range (Figure 4.7) and having values as in Table 4.2.

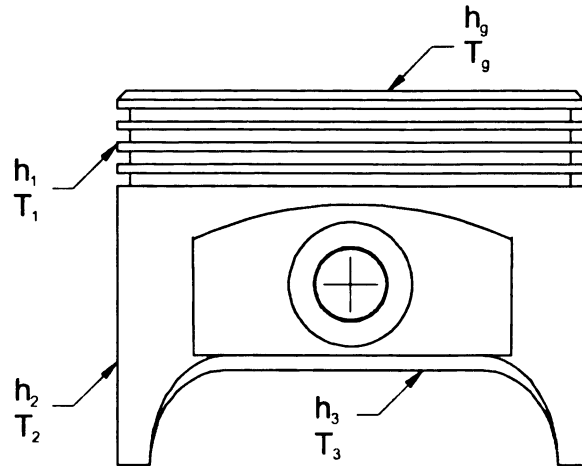


Figure 4.7: Heat transfer coefficients for parameterized piston

Table 4.2: Heat transfer coefficient and ambient temperature values for parameterized piston

| | |
|------------------------------------|-----------------------|
| $h_g = 200 \text{ W/m}^2\text{K}$ | $T_g = 470 \text{ K}$ |
| $h_l = 1000 \text{ W/m}^2\text{K}$ | $T_l = 314 \text{ K}$ |
| $h_2 = 700 \text{ W/m}^2\text{K}$ | $T_2 = 310 \text{ K}$ |
| $h_3 = 250 \text{ W/m}^2\text{K}$ | $T_3 = 303 \text{ K}$ |

The same values are used for the full model analysis with the addition of a heat transfer coefficient at the land area as well as at the pinhole of $400 \text{ W/m}^2\text{K}$ and $800 \text{ W/m}^2\text{K}$ respectively.

The thermal analysis was performed using three different sets of heat transfer coefficients: the ones of Table 4.2, an increase by 15% and a decrease them by 15%. This was done to assess the sensitivity of the piston to changes in the heat transfer coefficients. The full piston model temperature distributions for the three cases are shown in Figure 4.8, Figure 4.9, and Figure 4.10 respectively.

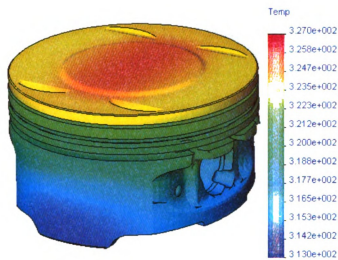


Figure 4.8: Full piston model temperature distribution with boundary conditions of Table 4.2 (temperature in Kelvin)

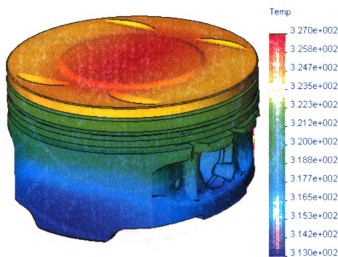


Figure 4.9: Full piston model temperature distribution with heat transfer coefficient values increased by 15% (temperature in Kelvin)

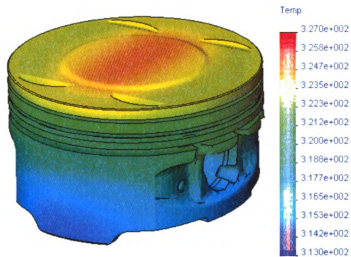


Figure 4.10: Full piston model temperature distribution with heat transfer coefficient values decreased by 15% (temperature in Kelvin)

Performing the thermal analysis on the parameterized piston model, it can be seen that the temperature distribution follows a very similar pattern as the full piston model (Figure 4.11, Figure 4.12, and Figure 4.13).

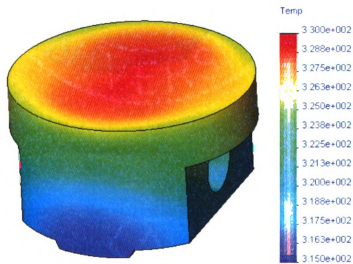


Figure 4.11: Parameterized piston model temperature distribution with boundary conditions of Table 4.2 (temperature in Kelvin)

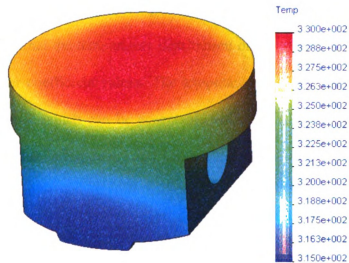


Figure 4.12: Parameterized piston model temperature distribution with heat transfer coefficient values increased by 15% (temperature in Kelvin)

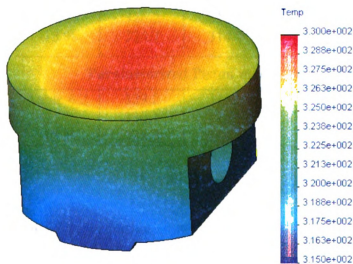


Figure 4.13: Parameterized piston model temperature distribution with heat transfer coefficient values decreased by 15% (temperature in Kelvin)

Table 4.3 summarizes the maximum and minimum temperatures for each of the above cases. The trends are the same for both models. The parameterized piston model, though, has less surface area exposed to convection than the full piston model. Consequently it has a maximum temperature of about 4 K higher than the full model.

Also the minimum temperature of the parameterized model is about 2 K higher. These results demonstrate that the temperature distribution on the piston is not greatly affected by the heat transfer coefficient values. The temperature difference of nodal values is in the range of 2 – 4 K which can be acceptable since the complexity of piston thermal loading is simplified as in Figure 4.7 and Table 4.2. Thus the assumed values of Table 4.2 can be considered valid.

Table 4.3: Maximum and minimum temperature for the three sets of heat transfer coefficients

| h | T_{max} (K) | T_{min} (K) | ΔT (K) |
|-----------------------------------|----------------------------|----------------------------|---------------|
| Full Piston Model | | | |
| Table 4.2 | 325.5 | 314.2 | 11.3 |
| +15 % | 326.2 | 313.6 | 12.6 |
| -15 % | 324.7 | 314.7 | 10.0 |
| Parameterized Piston model | | | |
| Table 4.2 | 329.2 | 315.9 | 13.3 |
| +15 % | 330.1 | 315.3 | 14.8 |
| -15 % | 328.3 | 316.6 | 11.7 |

4.2.2 Thermal Loading Deformation

The temperature distribution on the piston causes thermal strains which consequently deform the body. Considering only deformation due to thermal strains (Figure 4.14 and Figure 4.15), the two models are not in strong agreement quantitatively; but qualitatively they both deform outwards, away from the center axis. The full model has a maximum deformation of 102 μm at the tab edge and the parameterized 78 μm at the same location. However, considering the entire skirt face, the average deformation is

58 μm for the full model and 57 μm for the parameterized. Thus on a mean basis the two models have a strong agreement.

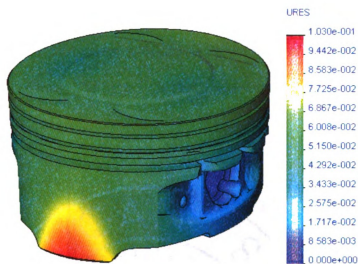


Figure 4.14: Full piston model deformation due to thermal loading (URES: resultant deformation in mm, deformation scale 1:50)

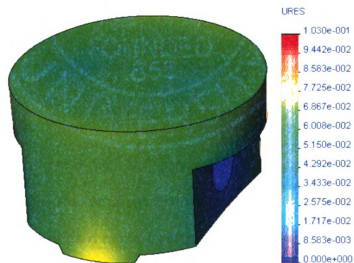


Figure 4.15: Parameterized piston model deformation due to thermal loading (URES: resultant deformation in mm, deformation scale 1:50)

4.2.3 Mechanical Loading

The piston experiences mechanical loads that force it to deform. In the analysis three loads are considered as well as a constraint. Ambient pressure (100 kPa) is applied above the crown to simulate the effects of combustion gases, and on the piston skirt to simulate the effects of lubrication pressure. A body load of 9.81 ms^{-2} is applied to account for inertial effects. The pinhole is restrained (Figure 4.16). The same loads are applied to the parameterized piston model.

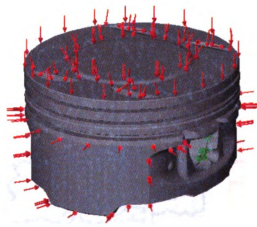


Figure 4.16: Mechanical loading, red arrows: atmospheric pressure, green arrows: constraint, body load not shown

Figure 4.17 and Figure 4.18 show the deformation due to mechanical loading for both the full piston model and the parameterized model respectively. The two demonstrate exactly the same behavior. The full model has a maximum deformation of $5.98 \mu\text{m}$, and the parameterized model deforms $6.04 \mu\text{m}$ towards the piston center axis. The two models have a strong agreement both quantitatively and qualitatively.

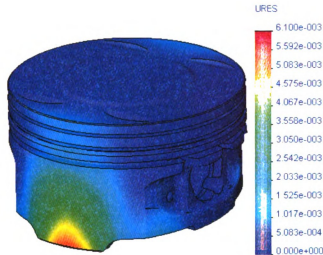


Figure 4.17: Full piston model deformation due to mechanical loading
(URES: resultant deformation in mm, deformation scale 1:50)

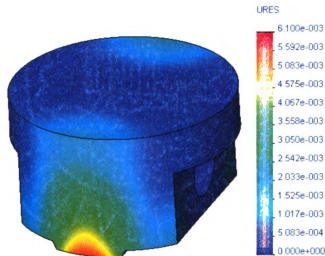


Figure 4.18: Parameterized piston model deformation due to mechanical loading
(URES: resultant deformation in mm, deformation scale 1:50)

4.2.4 Combined Thermal and Mechanical Loading

This section examines the effects on piston skirt deformation of both thermal and mechanical loads applied together. Since the lubrication pressure on the skirt is not

always uniform, influenced by piston tilting, piston lateral motion and bore distortion, different skirt load cases are considered in examining the overall skirt behavior.

- Case 1: Uniform normal pressure on skirt (Figure 4.19a)
- Case 2: Directional uniform pressure on skirt (Figure 4.19b). Pressure is in the z-direction
- Case 3: Stepped uniform normal pressure on skirt (Figure 4.19c). Maximum pressure is at the top of the thrust side.
- Case 4: Stepped uniform normal pressure on skirt (Figure 4.19d). Minimum pressure is at the top of the thrust side.
- Case 5: Stepped uniform normal pressure on skirt (Figure 4.19e). Maximum pressure is at the center of the skirt.
- Case 6: Stepped uniform normal pressure on skirt (Figure 4.19f). Maximum pressure is at the right half part of the piston, looking at it from the thrust side.

The rest of the loads and constraints are as in Figure 4.16.

In Figure 4.20 to Figure 4.31, the deformation results are shown for each of the above load cases. The thrust side is shown. The resultant deformation (URES) is in mm. The deformation scale is 1:50.

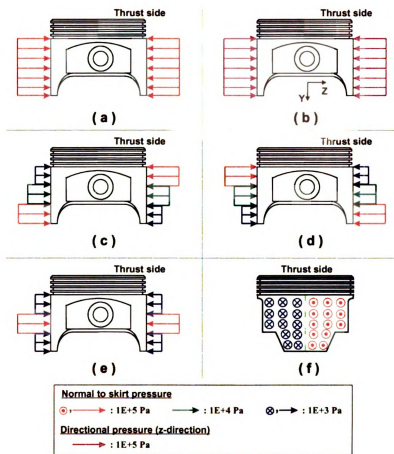


Figure 4.19: Pressure loads on skirt

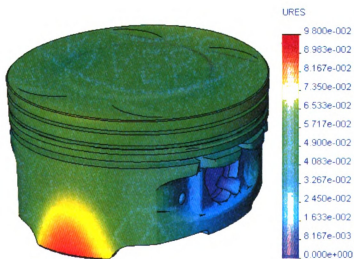


Figure 4.20: Full piston model deformation due to load case 1

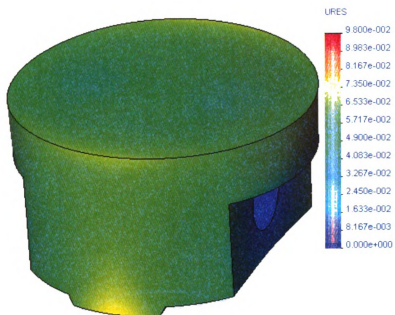


Figure 4.21: Parameterized piston model deformation due to load case 1

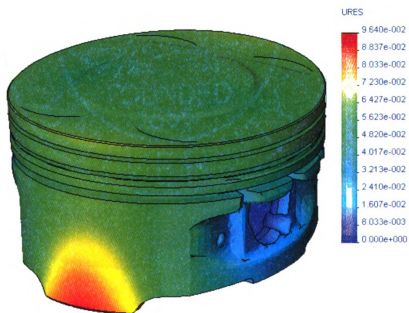


Figure 4.22: Full piston model deformation due to load case 2

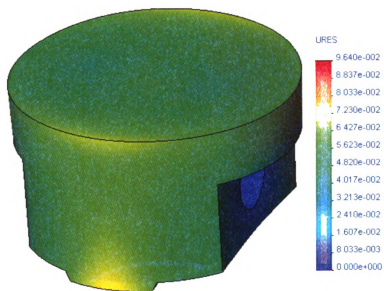


Figure 4.23: Parameterized piston model deformation due to load case 2

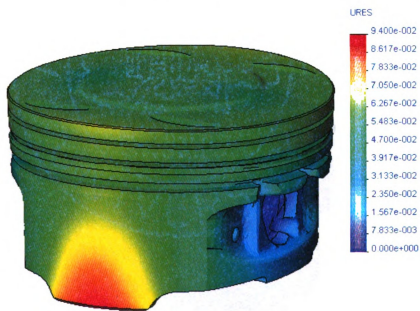


Figure 4.24: Full piston model deformation due to load case 3

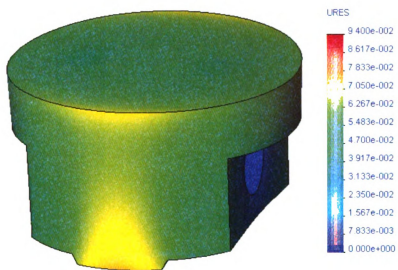


Figure 4.25: Parameterized piston model deformation due to load case 3

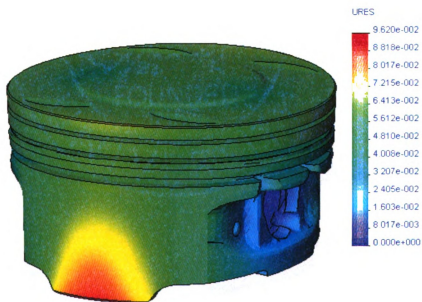


Figure 4.26: Full piston model deformation due to load case 4

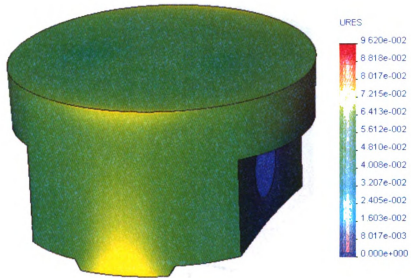


Figure 4.27: Parameterized piston model deformation due to load case 4

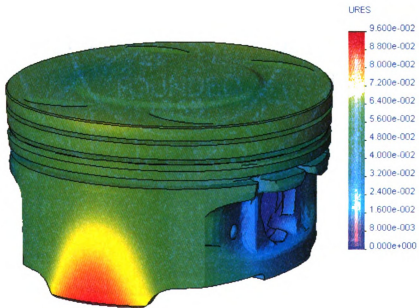


Figure 4.28: Full piston model deformation due to load case 5

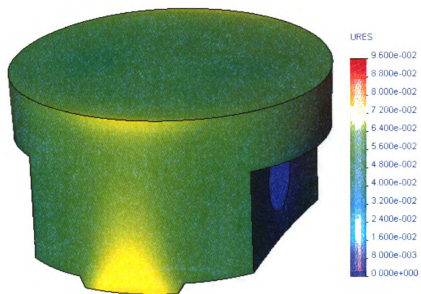


Figure 4.29: Parameterized piston model deformation due to load case 5

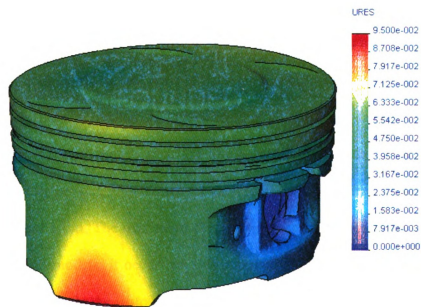


Figure 4.30: Full piston model deformation due to load case 6

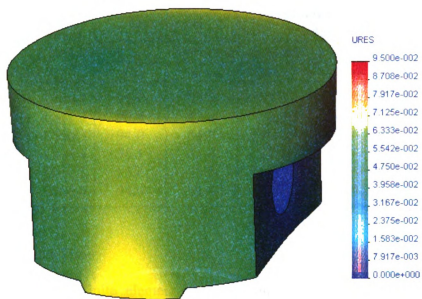


Figure 4.31: Parameterized piston model deformation due to load case 6

Considering Figure 4.21 to Figure 4.31 and Table 4.4, it can be concluded that the deformation on both the full model and the parameterized model follows the same trends. The two models have a qualitative agreement for all six load cases. The maximum deformation occurs around the tab area. The thermal strains, as discussed earlier, lead to a poor quantitative agreement, about $2\ \mu\text{m}$ for each load case. The mean deformation has a difference of about $1\ \mu\text{m}$. The maximum deformation occurs at the tab edge of the anti-thrust side for both models. It occurs on this side because the pin offset is towards the thrust side. Consequently the restrained nodes, at the pinhole, are further from the anti-thrust side, which allows it higher deformation.

Table 4.4: Maximum and mean deformations on skirt

| Skirt Load | Full Model | | Parameterized Model | |
|------------|-------------------------------|------|---------------------|------|
| | Deformation (μm) | | | |
| | Max | Mean | Max | Mean |
| Case 1 | 97.0 | 53.0 | 73.8 | 51.9 |
| Case 2 | 96.4 | 52.9 | 72.9 | 51.7 |
| Case 3 | 94.0 | 51.7 | 76.2 | 52.6 |
| Case 4 | 96.1 | 51.4 | 77.2 | 52.3 |
| Case 5 | 95.6 | 51.6 | 76.9 | 52.6 |
| Case 6 | 94.6 | 51.4 | 75.9 | 52.4 |

4.2.5 Computation Time

An independent finite element solver running under MATLAB was used to compare computation time between the full model and the parameterized model (Table 4.5). The mesh (4-node tetrahedral elements) was imported from COSMOS for both models. The analysis was run on a Pentium 4 3.0 GHz.

Table 4.5: Mesh and computation time comparison

| Parameter | Full Model | Parameterized Model |
|--|------------|---------------------|
| No. of Elements | 25270 | 6590 |
| No. of Nodes | 6339 | 1959 |
| Thermal Loading CPU Time (sec.) | 30.17 | 3.76 |
| Mechanical Loading CPU Time (sec.) | 489.55 | 17.03 |

In the case of the thermal loading analysis the solution time for the full model is greater by a factor of 8, compared to the parameterized model. Similarly in the case of the mechanical loading analysis the full model solution is slower by a factor of 29. Consequently running a full model analysis for one complete cycle would require 97.9

hours compared to 3.4 hours for the parameterized model. Thus the parameterized model is more cost-effective. Also it allows for a faster optimization of the design characteristics.

The mesh generated in CASE (pentahedral and hexahedral elements) for the parameterized model has 1620 elements with 6169 nodes. CASE uses a FORTRAN based finite element solver which required approximately 20 seconds for the solution of the thermal loading and the mechanical loading analyses.

4.3 CASE Analysis

4.3.1 Finite Element Analysis

Figure 4.32 shows the FEA results obtained from CASE for thermal loading. The temperature distribution ranges from 318 K to 337 K. It is slightly higher than the COSMOS result; the CASE uses a coarser mesh, also the solvers used are different. The COSMOS uses iterative solvers, whereas the CASE uses Gauss elimination.

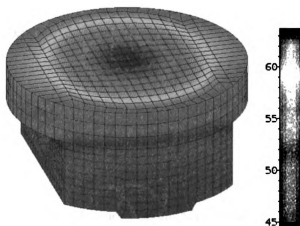


Figure 4.32: Parameterized piston model temperature distribution from CASE (temperature in degrees Celsius)

Figure 4.33 shows the FEA results obtained from CASE for the combined mechanical and thermal loading. These results, though, do not include the ambient pressure loading on the piston skirt. CASE adds pressure loads on the skirt during the cyclic analysis when there is a lubrication pressure. The deformation distribution follows the same pattern as the COSMOS results with a maximum deformation of 125 μm .

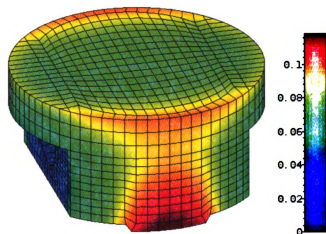


Figure 4.33: Parameterized piston model deformation obtained from CASE (deformation in mm)

4.3.2 Piston Characteristics

This section demonstrates some of the capabilities of CASE. Only some of the results are shown here: oil film thickness, friction force and piston dynamics.

Oil Film Thickness

Figure 4.34 and Figure 4.35 show the oil film thickness distribution on the skirt at 33 deg. on the thrust and anti-thrust sides respectively. From these, the piston orientation can be deduced. At 33 deg., the top part of the piston tilts towards the thrust side and the

bottom part towards the anti-thrust. The oil film thickness distribution follows the pattern of the deformed skirt profile as in Figure 4.20. Also it is in the range of 500 μm , which is the clearance between the nominal bore diameter and nominal piston diameter. Nominal clearances are usually in the range of 50-70 μm . Here, the clearance is very large because of the specifically built sapphire cylinder.

Friction Force

Figure 4.36 shows the friction force between piston and cylinder wall. A positive value designates contact with cylinder on the anti-thrust side and negative value designates contact on the thrust side. The four contact points considered are shown in Figure 4.37. When the friction force is zero, the piston is floating in the cylinder.

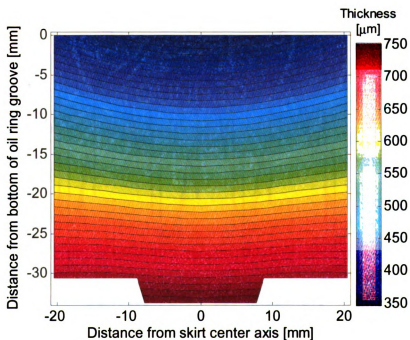


Figure 4.34: Skirt oil film thickness on thrust side at 33 CAD

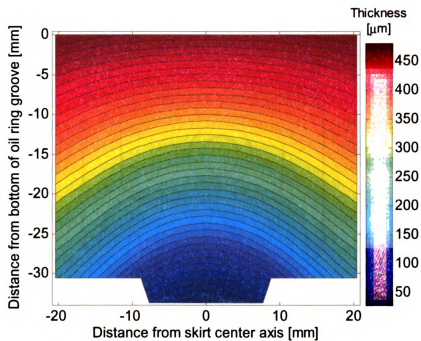


Figure 4.35: Skirt oil film thickness on anti-thrust side at 33 CAD

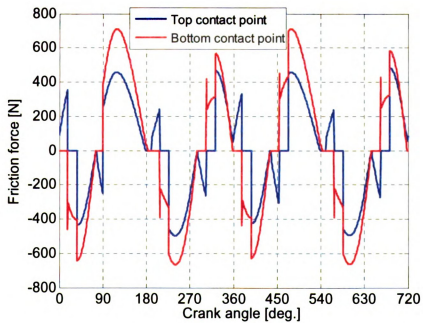


Figure 4.36: Friction force between piston and cylinder liner

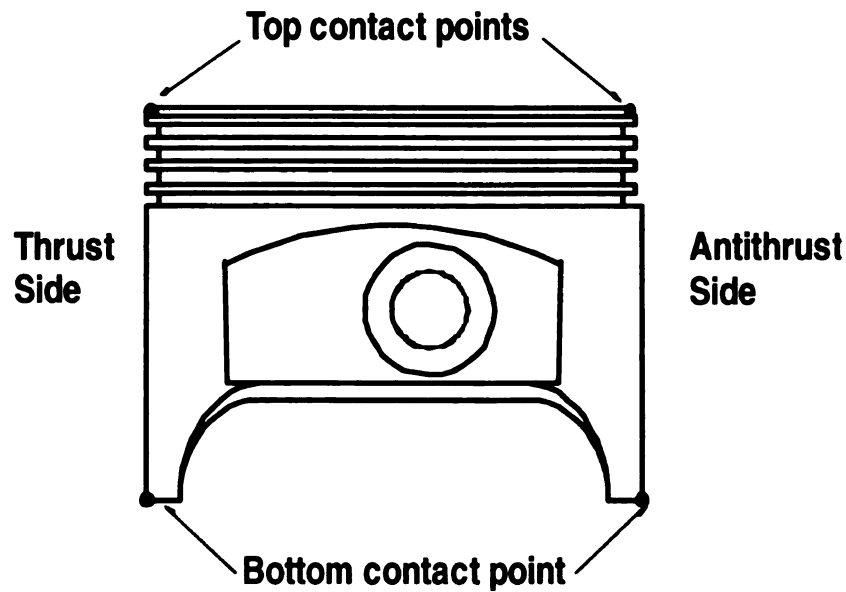


Figure 4.37: Contact points of piston with cylinder wall

Piston Dynamics

Figure 4.38 shows the piston rotation over a cycle. At 33 deg. the piston has a negative rotation, which means that the top part of the piston tilts towards the thrust side. This agrees with the oil film thickness distribution.

Figure 4.39 shows the piston pin lateral motion. A positive value designates movement of the piston pin towards the anti-thrust side. Negative values show movement towards the thrust side. Piston pin lateral motion affects contact forces. Considering Figure 4.36 and Figure 4.39, it can be seen that when the pin lateral position is at the maximum the friction force peaks.

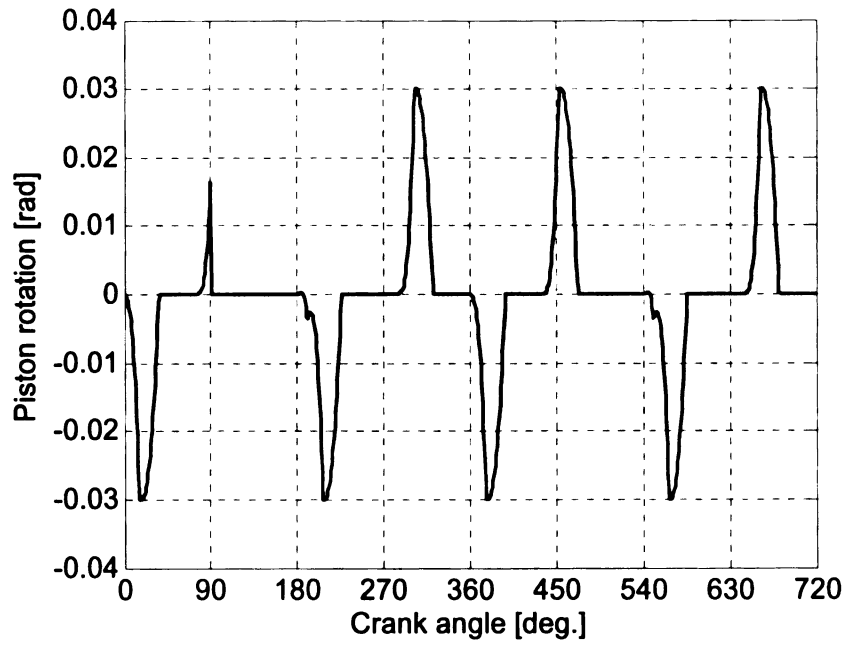


Figure 4.38: Cyclic piston rotation about pin

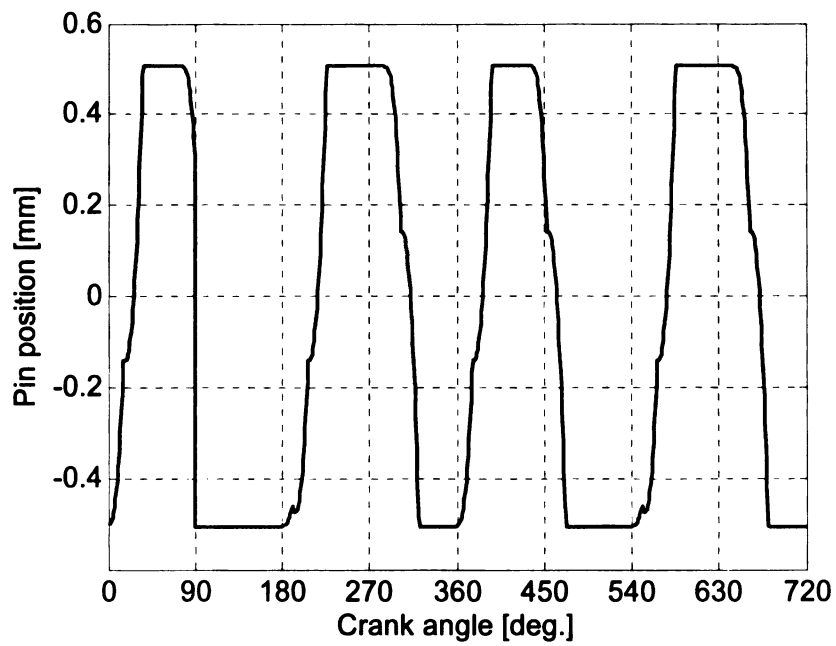


Figure 4.39: Cyclic piston pin lateral motion

4.4 Experimental Results

The experimental results¹ for oil film thickness from the motored sapphire bore engine are inconclusive. Very few results are available and although they demonstrate a qualitative agreement with the simulated results they do not agree quantitatively. The experimental results are obtained using the laser induced fluorescence method. Figure 4.40 shows the experimental oil film thickness measurement at the TDC of the intake stroke. Figure 4.41 shows the predicted oil film thickness by CASE at the same stroke and location. Both experimental and simulated results show a thicker oil film near the oil ring groove, which gets thinner away from it and towards the piston central axis. The quantitative discrepancy can be attributed to three factors.

At this preliminary stage the thermoelastic and lubrication behavior of the sapphire cylinder is still not well understood to be applied accurately to the piston model. In the CASE simulation a fully flooded elastohydrodynamic model is assumed, however experimental results show some irregularities which indicate the potential existence of the partially flooded condition. Finally in the specific simulation the piston-to-bore clearance is independent of the elastohydrodynamic behavior of the piston. The piston-to-bore clearance is calculated from the cold-stage piston skirt profile rather than the crank angle dependent deformed skirt profile which leads to bigger clearances. Consequently these factors are under consideration and together with the acquisition of more experimental results will be presented at a later stage.

¹ Experimental oil film thickness measurements were provided by Andrew Fedewa of Mid-Michigan Research sponsored by the US Army.

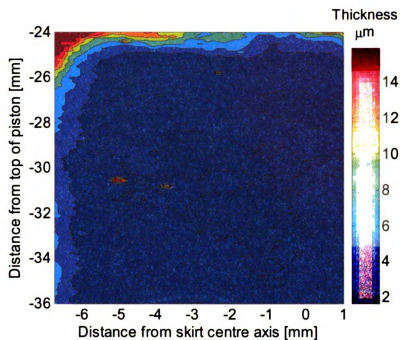


Figure 4.40: Experimental oil film thickness measurement at TDC of intake stroke

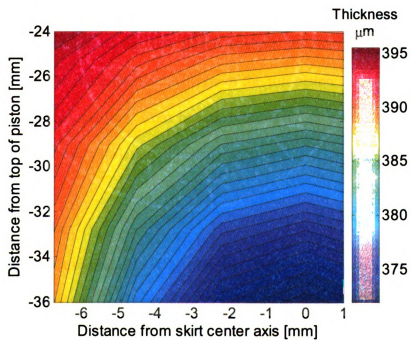


Figure 4.41: Simulated oil film thickness prediction at TDC of intake stroke

CHAPTER 5

PISTON FINITE ELEMENT ANALYSIS: THE FULL MODEL APPROACH

5.1 Introduction

As was shown in the last chapter, a parameterized piston model can be used as guidance in assessing the piston characteristics. Once that guide line is obtained, what can be done with it? The answer is proposed in this chapter. The goal is to develop a piston program that will supplement the existing one in CASE. The new program will be able to perform an analysis for a full piston model. The optimal design characteristics for the piston obtained from the parameterized model analysis would be used to modify the computer aided design (CAD) model of the full piston. The optimized full model then would be analyzed to ensure for optimal piston characteristics.

The first module of the new piston analysis program is introduced here. This module performs the finite element analysis of the full piston over the cycle, thus called piston finite element analysis, from hereon referred to as *π -fea*. The Greek letter ' π ' appears from the Greek translation of piston, '*πιστόνι*'.

5.2 Preprocessing

Unlike the existing PISTON program in CASE, *π -fea* is not a standalone program; some preprocessing is required for the full piston model.

5.2.1 CAD Model

The current version of *π -fea* requires the piston model to be oriented as shown in Figure 5.1.

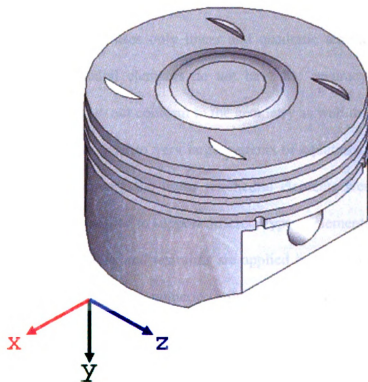


Figure 5.1: Piston orientation

The *x*-axis should pass through the skirt face with the anti-thrust side being in the positive *y-z* plane. The *y*-axis should be parallel to the piston axis and the *z*-axis should be parallel to the pinhole axis. The origin of the piston's global coordinate system should be at the centre of the crown. The orientations of the piston can be very easily changed in any CAD software. For this work SolidWorks is the software of choice.

5.2.2 Mesh and boundary conditions

The next step is to mesh the model and apply the boundary conditions for both the thermal and static analysis. The current version of *π -fea* supports mesh data files created in COSMOSDesignSTAR.

COSMOSDesignSTAR uses only linear and quadratic tetrahedral elements for meshing. The linear tetrahedral elements do not have the accuracy of the quadratic tetrahedral elements as they do not conform to the geometry as well due to their linearity. Quadratic elements however, lead to very large systems of equations. Thus considering limitations in computer memory, the linear tetrahedral elements were chosen for this study. *π -fea* can be easily modified to support different type of elements.

The boundary conditions and restraints are applied in COSMOSDesignSTAR as well. Rather than applying the numeric value of the boundary condition in COSMOSDesignSTAR, the piston faces affected by a specific boundary are flagged. This allows for *π -fea* to recognize faces and apply the right boundary condition. Also the user can run different simulations with different boundary conditions without having to go back to COSMOSDesignSTAR.

Table 5.1 shows the flags used for the thermal analysis. A convective boundary is applied to the faces. The heat transfer coefficient value is assigned as a flag for each area.

Table 5.1: Flags for thermal analysis

| <i>Piston area</i> | <i>COSMOSDesignSTAR Flag</i> |
|---|--------------------------------------|
| Crown | $h = 1 \text{ Wm}^{-2}\text{K}^{-1}$ |
| Ring-pack area | $h = 2 \text{ Wm}^{-2}\text{K}^{-1}$ |
| Skirt area (thrust and anti-thrust sides) | $h = 3 \text{ Wm}^{-2}\text{K}^{-1}$ |
| Underside | $h = 4 \text{ Wm}^{-2}\text{K}^{-1}$ |

Table 5.2 shows the flags used for the static analysis. A uniform pressure flag is assigned to the crown, thrust and anti-thrust sides faces. A fixed restraint is applied to the pinhole and a body force in the positive y -direction is applied to the whole piston.

Table 5.2: Flags for static analysis

| <i>Piston area</i> | <i>COSMOSDesignSTAR Flag</i> |
|-------------------------------|---|
| Crown | $P = 1 \text{ Pa}$ |
| Skirt area (thrust side) | $P = 2 \text{ Pa}$ |
| Skirt area (anti-thrust side) | $P = 3 \text{ Pa}$ |
| Pinhole | Restraint = Fixed |
| Body | Body force: $y\text{-dir} = 9.81 \text{ ms}^{-2}$ |

COSMOSDesignSTAR outputs two data files, one for the thermal analysis and one for the static analysis. Each data file contains the nodal coordinates, the connectivity matrix, and the boundary conditions. The format of the data files is described in reference [8].

5.3 Piston Finite Element Analysis (π -*fea*) program

After the piston model is preprocessed the π -*fea* program takes over to perform the cyclic analysis. Figure 5.2 shows an overview of the π -*fea* program flow. Detailed flowcharts of the π -*fea* program and of its subroutines are shown in Appendix A.

The π -*fea* program starts by loading the mesh data files exported from COSMOSDesignSTAR. Then it loads the file that contains the piston material properties, engine geometry, boundary conditions and pressure trace. After that it calculates the piston motion as described in Section 3.4. Following this it calls the *FEMmeshread* subroutine. Here the mesh data files are read. This subroutine returns the nodal coordinates, connectivity matrix, and arrays containing the boundary conditions with

their associated faces. Then it calls the *FEMthermal* subroutine. Here the thermal finite element analysis is performed as described in Section 2.4.1.

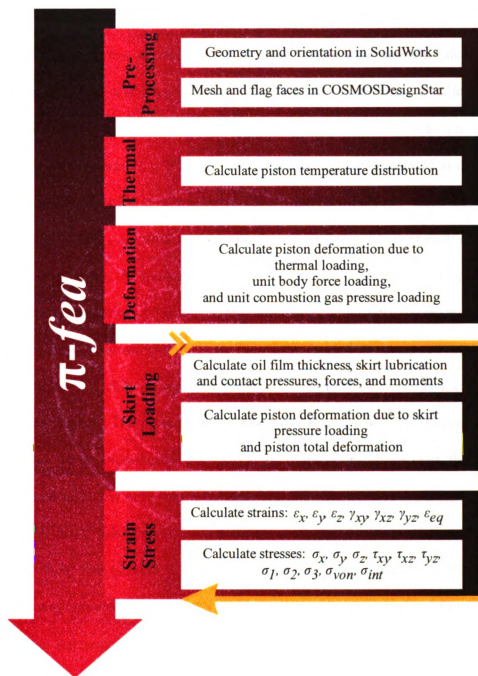


Figure 5.2: Overview of the π -fea program flow

FEMthermal returns an array containing the nodal temperatures, as well as an array containing the element characteristics, that is, volume and shape function derivatives. This element characteristic array is used by the rest of the subroutines that require element characteristics information in the calculations.

This speeds up the whole program as element characteristics are calculated only once. Following the *FEMthermal* subroutine the *FEMstatic* subroutine is called. Here the deformations due to the thermal strains, d_t , due to a body force, $b_l = 9.81 \text{ ms}^{-2}$, d_{bu} , and due to a uniform pressure, $P_u = 100 \text{ kPa}$, on the crown, d_{gu} , are calculated as described in Section 2.4.2. Deformation is assumed to vary linearly with body force and pressure loading thus d_{bu} and d_{gu} are used to calculate the actual deformation at each crank angle over the cyclic analysis. *FEMstatic* also returns the connectivity matrix for both the skirt thrust and anti-thrust sides. After this, *π -fea* prepares an array with the node numbers of the nodes on the skirt in ascending order. This array is used as an input for *FEMGuyan* subroutine where the skirt compliance matrix is calculated as well as the coordinate transformation matrix. The method is described in Section 2.4.5. The Guyan reduction method allows for the reduction of the system just to the nodes on the skirt, thus allowing for a faster solution. The next step is to transform the skirt surface (bearing area) of the thrust and anti-thrust sides from the three-dimensional global coordinate system to a two-dimensional local one (Figure 5.3). This is done under the assumption that the skirt curvature is negligible compared to the skirt circumferential length, thus allowing for the solution of the Reynolds equation as described in Section 2.4.3.

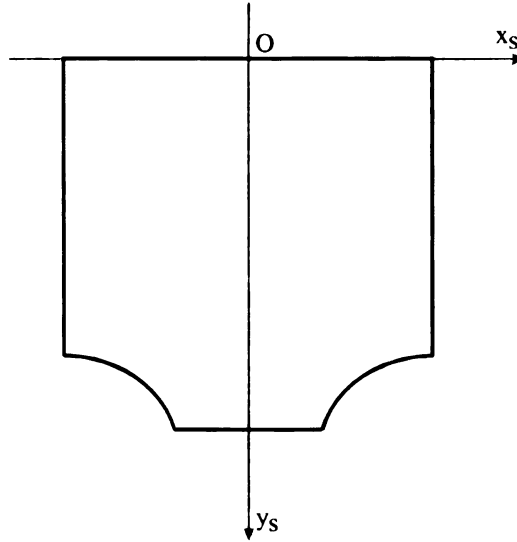


Figure 5.3: 2D skirt profile

Now, with all these prepared, the cyclic analysis begins. The time step is set at one crank angle and is controlled by the external loop. The deformations due to combustion gas pressure, Eq. (5.1), and piston axial acceleration, Eq. (5.2), are calculated.

$$d_g(x, y, z, t) = \frac{P_g(t)}{P_u} d_{gu}(x, y, z) \quad (5.1)$$

$$d_b(x, y, z, t) = \frac{a_p(t)}{b_l} d_{bu}(x, y, z) \quad (5.2)$$

Following this an iterative loop starts, the internal loop, to calculate the total pressure on the skirt. An initial guess for the total pressure is required at $t = 0$. To make the initial guess simple it is suggested to start from zero pressure, $P_t(t = 0) = 0$. Within the internal loop the *FEMstaticLUB* subroutine is called, where the load vector due to pressure loading on the skirt is built. Using the reduced stiffness matrix form *FEMGuyan*

subroutine the deformation on the skirt due to hydrodynamic pressure loading, d_{sh} , is calculated. Having all these, the total deformation on the skirt, d_s , is calculated.

$$d_{s,m}(x, y, z, t) = d_{t,m}(x, y, z) + d_{b,m}(x, y, z, t) + d_{g,m}(x, y, z, t) + d_{sh,m}(x, y, z, t) \quad (5.3)$$

where,

$$m = \begin{cases} 1 & \text{thrust side} \\ 2 & \text{anti-thrust side} \end{cases} \quad (5.4)$$

Given the piston orientation described in Section 5.2.1 the lubricant film thickness can be well approximated by,

$$h_m(t) = C + \left(R - \left\| d_{s,m}(x, y = \text{const}, z, t) \right\| \right) \quad (5.5)$$

where C is the nominal clearance between cylinder bore and piston, R is the piston radius, and $\left\| d_{s,m}(x, y = \text{const}, z, t) \right\|$ is the magnitude of the deformation vector evaluated from $x = 0$, $z = 0$ and at constant y . The squeeze film is given by

$$\dot{h}_m(t) = \frac{h_m(t) - h_m(t-1)}{\Delta t} \quad (5.6)$$

If the lubricant film thickness, h_m , becomes smaller than the skirt waviness, Ω , then wavy contact occurs between the cylinder wall and the skirt. The wavy deformation, δ_m , is given by

$$\delta_m = \begin{cases} \Omega - h_m, & \text{if } h_m < \Omega \\ 0, & \text{if } h_m > \Omega \end{cases} \quad (5.7)$$

Zhu et al [58, 59] , using Johnson's model (1985) for a blunt wedge against a plane, proposed a formula for the mean solid-to-solid contact pressure between an aluminum alloy piston and a cast iron cylinder wall:

$$P_{c,m} = (5.464 \times 10^{13}) \delta_m^{1.0552} \quad (5.8)$$

This relation is used in this work.

Following this the *ReEq* subroutine is called. Here the Reynolds lubrication equation is solved for the hydrodynamic pressure, P_h , on the skirt area as described in Section 2.4.3. $P_h = 0$ is used as the boundary condition for the Reynolds equation. Once the hydrodynamic pressure is calculated, the half-Sommerfeld condition, Eq. (5.9), is applied as conventional lubricants cannot withstand negative pressures and cavitate [32].

$$P_{h,m} = P_{h,m} \cdot \chi(P_{h,m}) \quad (5.9)$$

where $\chi(P_{h,m})$ is a switch function,

$$\chi(P_{h,m}) = \begin{cases} 1, & \text{if } P_{h,m} \geq 0 \\ 0, & \text{if } P_{h,m} < 0 \end{cases} \quad (5.10)$$

The total pressure, P_t , can then be calculated:

$$P_{t,m} = P_{h,m} + P_{c,m} \quad (5.11)$$

The program checks for pressure convergence. The pressure residual, P_{res} , is calculated by,

$$P_{res} = \frac{\sum |P_t^i - P_t^{i-1}|}{\sum |P_t^i|} \quad (5.12)$$

where i is the internal loop iteration number. If the pressure residual between successive internal loop iterations goes below a predefined tolerance (usually 10^{-3}), then the internal loop exits to the external loop. Otherwise the pressure is modified using underrelaxation:

$$P_t^i = P_t^{i-1} + \omega_r (P_t^i - P_t^{i-1}) \quad (5.13)$$

where ω_r is the underrelaxation factor. ω_r begins at 0.5 and if successive pressure residuals increase, then ω_r is decreased by 0.1 up to 0.1. P_h and P_c are very sensitive to the deformations thus numerical stability becomes more difficult to achieve as the lubricant film thickness decreases.

Once the pressure is converged, the hydrodynamic, contact and friction forces and moment acting on the piston can be calculated (Figure 5.4).

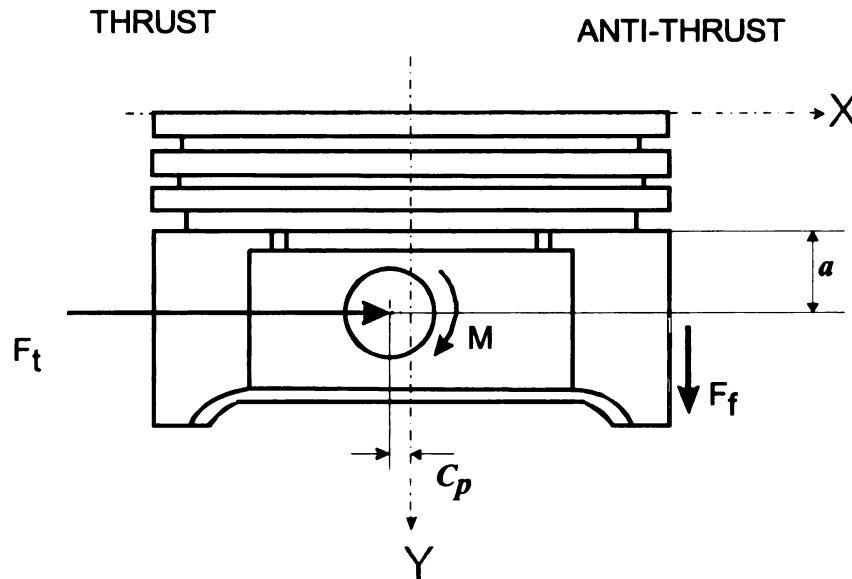


Figure 5.4: Forces and moments acting on piston

The hydrodynamic force is given by integrating the hydrodynamic pressure over the two-dimensional skirt area (Figure 5.3),

$$F_{h,m} = \iint_{A_{s,m}} P_{h,m}(x_{s,m}, y_{s,m}) dx_{s,m} dy_{s,m} \quad (5.14)$$

Similarly the hydrodynamic moment about the wrist pin is given by,

$$M_{h,m} = \iint_{A_{s,m}} P_{h,m}(x_{s,m}, y_{s,m}) \cdot (a - y_{s,m}) dx_{s,m} dy_{s,m} \quad (5.15)$$

The total hydrodynamic force F_h is given by,

$$F_h = F_{h,1} - F_{h,2} \quad (5.16)$$

and the total hydrodynamic moment, M_h , is given by,

$$M_h = M_{h,1} - M_{h,2} \quad (5.17)$$

The shear stress acting on the skirt can be expressed as,

$$\tau_m = -\frac{\mu v_p}{h_m} + \frac{h_m}{2} \frac{\partial P_{h,m}}{\partial y_{s,m}} \quad (5.18)$$

The hydrodynamic friction and its moment about the wrist can be calculated as follows:

$$F_{fh,m} = \iint_{A_{s,m}} \tau_m(x_{s,m}, y_{s,m}) dx_{s,m} dy_{s,m} \quad (5.19)$$

$$M_{fh,m} = \iint_{A_{s,m}} \tau_m(x_{s,m}, y_{s,m}) \cdot (x_{s,m} - C_p) dx_{s,m} dy_{s,m} \quad (5.20)$$

The total hydrodynamic friction, F_{fh} , and total hydrodynamic moment, M_{fh} , are expressed as follows

$$F_{fh} = F_{fh,1} + F_{fh,2} \quad (5.21)$$

$$M_{fh} = M_{fh,1} - M_{fh,2} \quad (5.22)$$

In a similar way the total contact force, F_c , and total contact moment, M_c , are calculated:

$$F_{c,m} = \iint_{A_{s,m}} P_{c,m}(x_{s,m}, y_{s,m}) dx_{s,m} dy_{s,m} \quad (5.23)$$

$$M_{c,m} = \iint_{A_{s,m}} P_{c,m}(x_{s,m}, y_{s,m}) \cdot (a - y_{s,m}) dx_{s,m} dy_{s,m} \quad (5.24)$$

$$F_c = F_{c,1} - F_{c,2} \quad (5.25)$$

$$M_c = M_{c,1} - M_{c,2} \quad (5.26)$$

Given a friction coefficient μ_f , between the cylinder liner and the piston skirt, then the contact friction force, F_{fc} , and contact friction moment, M_{fc} , are expressed as follows:

$$F_{fc,m} = -\frac{|v_p|}{v_p} \iint_{A_{s,m}} \mu_f P_{c,m}(x_{s,m}, y_{s,m}) dx_{s,m} dy_{s,m} \quad (5.27)$$

$$M_{fc,m} = \frac{|v_p|}{v_p} \iint_{A_{s,m}} \mu_f P_{c,m}(x_{s,m}, y_{s,m}) \cdot (x_{s,m} - C_p) dx_{s,m} dy_{s,m} \quad (5.28)$$

$$F_{fc} = F_{fc,1} + F_{fc,2} \quad (5.29)$$

$$M_{fc} = M_{fc,1} - M_{fc,2} \quad (5.30)$$

Now the total normal force on the piston due to hydrodynamic and contact pressures is given by,

$$F_t = F_h + F_c \quad (5.31)$$

the total friction is given by,

$$F_f = F_{fh} + F_{fc} \quad (5.32)$$

and the total moment, M , is given by,

$$M = M_h + M_c + M_{fh} + M_{fc} \quad (5.33)$$

Following this the total deformation of the piston is calculated. Using the coordinate transformation matrix (Section 2.4.5), $[T]$, the deformation for the whole piston, d_h , due to the pressure loading on the skirt is calculated. The total piston deformation, d , is given by,

$$\begin{aligned} d(x, y, z, t) = & d_t(x, y, z) + d_b(x, y, z, t) \\ & + d_g(x, y, z, t) + d_h(x, y, z, t) \end{aligned} \quad (5.34)$$

The resultant deformation, d_r , is expressed as,

$$d_r(x, y, z, t) = \|d(x, y, z, t)\| \quad (5.35)$$

Now that the program has calculated total piston deformation, the *FEMstrain* subroutine is called. Here the strains for each element are calculated, as well as the stresses at each node. The strain vector is calculated according to Eq. (2.93), and the stress vector according to Eq. (2.96). Some further calculations are performed within the *FEMstrain* subroutine. The equivalent or effective strain, ϵ_{eq} , is calculated as,

$$\epsilon_{eq} = 2\sqrt{\frac{\epsilon_1 + \epsilon_2}{3}} \quad (5.36)$$

where,

$$\begin{aligned} \epsilon_1 &= \frac{1}{2} \left[(\epsilon_x - \epsilon_a)^2 + (\epsilon_y - \epsilon_a)^2 + (\epsilon_z - \epsilon_a)^2 \right] \\ \epsilon_2 &= \frac{1}{4} \left[(\gamma_{xy})^2 + (\gamma_{xz})^2 + (\gamma_{yz})^2 \right] \\ \epsilon_a &= \frac{1}{3} (\epsilon_x + \epsilon_y + \epsilon_z) \end{aligned} \quad (5.37)$$

The von Mises stress component, σ_{von} , is calculated from the stress components as,

$$\sigma_{von} = \left[\frac{1}{2} \left[(\sigma_x - \sigma_y)^2 + (\sigma_x - \sigma_z)^2 + (\sigma_y - \sigma_z)^2 \right] + 3 \left[(\sigma_{xy})^2 + (\sigma_{xz})^2 + (\sigma_{yz})^2 \right] \right]^{1/2} \quad (5.38)$$

The principal stresses, σ_1 , σ_2 , and σ_3 are given by the eigenvalues of the stress tensor:

$$\begin{bmatrix} \sigma_1 & 0 & 0 \\ 0 & \sigma_2 & 0 \\ 0 & 0 & \sigma_3 \end{bmatrix} = eig \left\{ \begin{bmatrix} \sigma_x & \sigma_{xy} & \sigma_{xz} \\ \sigma_{xy} & \sigma_y & \sigma_{yz} \\ \sigma_{xz} & \sigma_{yz} & \sigma_z \end{bmatrix} \right\} \quad (5.39)$$

The stress intensity, σ_{int} , is calculated from the difference of the maximum and minimum principal stresses. Given that $\sigma_1 > \sigma_2 > \sigma_3$ then,

$$\sigma_{int} = \sigma_1 - \sigma_3 \quad (5.40)$$

After all these calculations are made, the data is saved and the outer loop moves to the next crank angle. The final converged solution of the hydrodynamic and contact pressures will be periodic and will not depend on the initial guess for the total pressure.

$$P_h(t) = P_h \left(t + \frac{4\pi}{\omega} \right), \quad (5.41)$$

$$P_c(t) = P_c \left(t + \frac{4\pi}{\omega} \right)$$

It is observed that a periodic solution is usually achieved after the second cycle. Convergence of pressure, however, is greatly dependent on clearance. A high clearance will tend to converge up to ten times faster than a low clearance.

5.4 π -fea Verification

As π -fea is a newly developed program, its predictions for both, the temperature and the deformation are compared with COSMOSDesignSTAR's predictions for verification. A piston is considered with the thermal loads of in Table 4.2. A 100 kPa uniform pressure is applied to the crown and the skirt, Also a body load of 9.81 ms^{-2} is applied.

Figure 5.5 shows the nodal temperature as predicted by π -fea and COSMOSDesignSTAR. The two predictions are in excellent agreement.

Figure 5.6 shows the prediction for the nodal resultant deformation. This deformation is caused by both the thermal and mechanical loads. For the π -fea prediction the contribution to the deformation due to the skirt loading is calculated via the Guyan reduction technique (Section 2.4.5). The two predictions are also in excellent agreement.

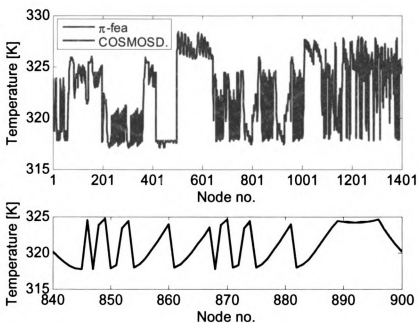


Figure 5.5: Nodal temperature as predicted by π -*fea* and COSMOSDesignSTAR

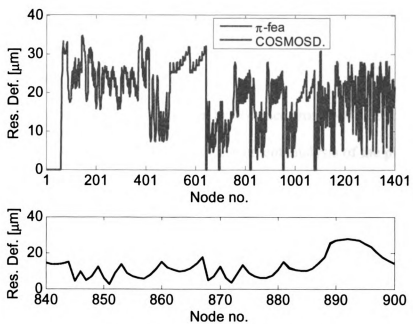


Figure 5.6: Nodal resultant deformation as predicted by π -*fea* and COSMOSDesignSTAR

CHAPTER 6

RESULTS

6.1 Introduction

This chapter presents results that can be obtained from π -*fea*. It should be recalled that this version of π -*fea* only performs a finite element analysis of the piston to calculate piston deformation and piston skirt loading, assuming no secondary motion of the piston. Consequently the results are not typical for a real operating piston as secondary dynamics greatly influence piston behavior.

6.2 Engine geometry and operating conditions

The engine geometry used for this simulation is the optical engine of Chapter 4. Table 6.1 shows the required inputs for the engine geometry and operating conditions. Figure 6.1 shows the pressure trace used for the simulation.

Table 6.1: Engine geometry and operating conditions

| Parameter | Value |
|-----------------------|---|
| Engine speed | 1000 RPM |
| Bore diameter | Simulation I: 90.2 mm Simulation II: 90.1 mm |
| Stroke | 90.6 mm |
| Connecting rod length | 133 mm |
| Oil viscosity | 0.02 Pa-s |
| Friction coefficient | 0.15 |

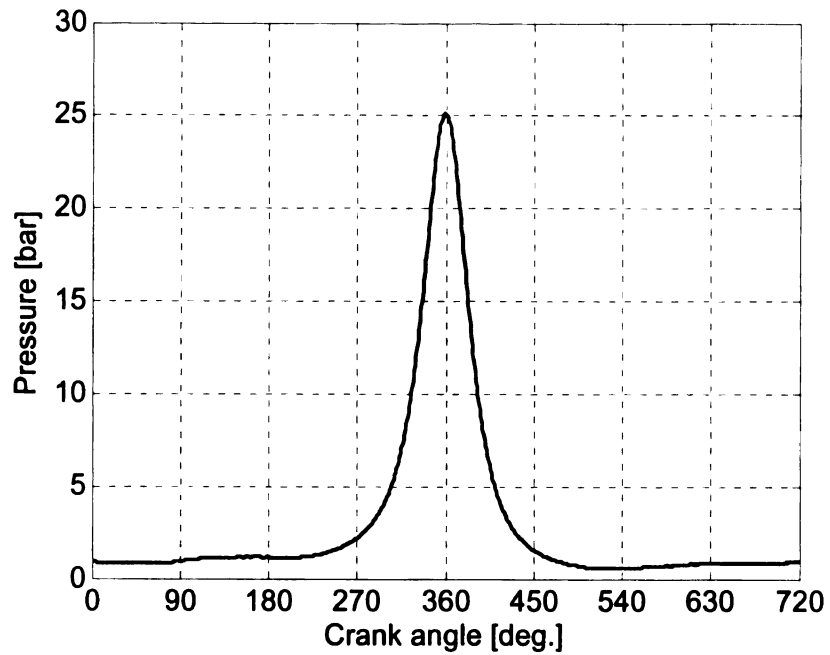


Figure 6.1: Pressure trace used for simulation

6.3 Piston geometry and properties

The piston used for this simulation is a generic piston, designed to comply with the engine geometry of Section 6.2. Table 6.2 shows the piston properties and Figure 6.2 shows the piston CAD model used for the simulation.

Table 6.2: Piston properties

| Parameter | Value |
|---|--------------------|
| Mass | 0.4536 kg |
| Diameter | 90 mm |
| Pin offset | -0.4 mm |
| Distance from top of skirt to centre of pin | 14.5 mm |
| Skirt waviness | 3.50 μm |

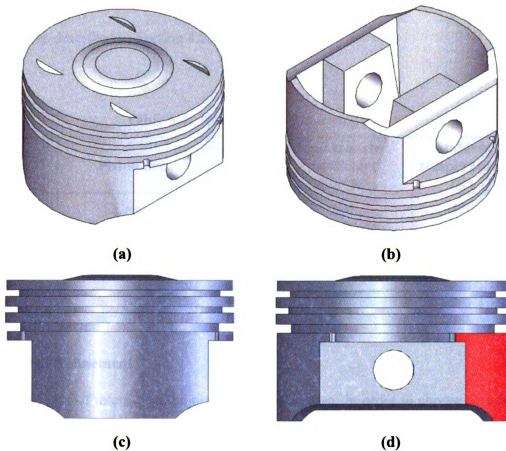


Figure 6.2: Piston CAD model, (a) isometric view, anti-thrust side shown, (b) underside, (c) front view, anti-thrust side shown, (d) side view, red: thrust side

The material used for the piston is aluminum alloy 1345. Its material properties are shown in Table 6.3.

Table 6.3: Material properties for aluminum alloy 1345

| Property | Value |
|----------------------------------|-------------------------------------|
| Modulus of Elasticity | 69 GPa |
| Tensile yield strength | 82.72 MPa |
| Poisson's ratio | 0.33 |
| Density | 2700 kgm^{-3} |
| Coefficient of thermal expansion | $2.4 \times 10^{-5} \text{ K}^{-1}$ |
| Thermal conductivity | $200 \text{ Wm}^{-1}\text{K}^{-1}$ |

The thermal boundary conditions for the piston are shown in Table 6.4. The values are as described in Section 4.2.1.

Table 6.4: Thermal boundary conditions

| Piston area | Heat transfer coefficient (Wm⁻²K⁻¹) | Ambient temperature (K) |
|---|--|------------------------------------|
| Crown | 200 | 470 |
| Ring-pack area | 1000 | 314 |
| Skirt area (thrust and anti-thrust sides) | 700 | 310 |
| Underside | 250 | 303 |

6.4 Mesh Refinement

The area of interest on the piston is the skirt area. In order to choose an adequate element size for the mesh a mesh refinement study was performed. Figure 6.3 shows the imported piston meshed geometry into *π-fea*. The global element size is 9.2502 mm. The skirt area though is meshed using an element size of 3 mm (Figure 6.4). Five different meshes were tested as of Table 6.5, varying the element size on the skirt.

To assess the quality of each mesh the hydrodynamic force on thrust and anti-thrust sides as well as the total friction force were checked. On the thrust (Figure 6.5) side meshes I, II, and III are in good agreement. Meshes IV and V give a slightly higher force at each crank angle, with the maximum difference being at about 3 N. This implies an error of about 6%. On the anti-thrust side (Figure 6.6) only meshes I and II are in very good agreement. The maximum difference in this case is about 6 N. The total hydrodynamic friction is in very good agreement for all five cases. This implies that the velocity of the piston, Eq. (5.18), dominates in the evaluation of friction. Considering the

above mentioned results and mesh sizes (Table 6.5), mesh III was chosen for this study as it is only a demonstrative study and high accuracy is not required.

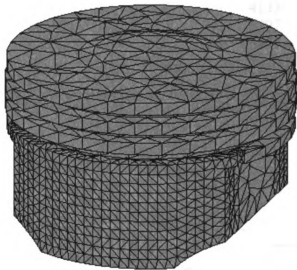


Figure 6.3: Imported piston meshed geometry, global element size: 9.2502 mm, skirt element size: 3 mm

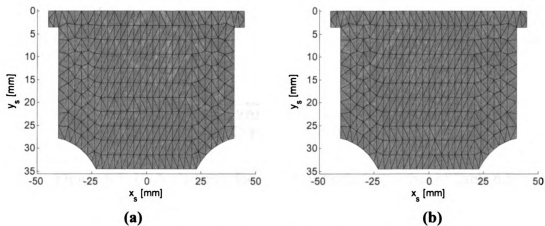


Figure 6.4: Skirt mesh, (a) thrust side, (b) anti-thrust side

Table 6.5: Mesh sizes

| Mesh | Global element size (mm) | Skirt element size (mm) | No. of elements | No. of nodes |
|------|--------------------------|-------------------------|-----------------|--------------|
| I | 9.2502 | 5 | 3808 | 1273 |
| II | 9.2502 | 4 | 4133 | 1398 |
| III | 9.2502 | 3 | 4997 | 1728 |
| IV | 9.2502 | 2.5 | 6097 | 2119 |
| V | 9.2502 | 2 | 8034 | 2791 |

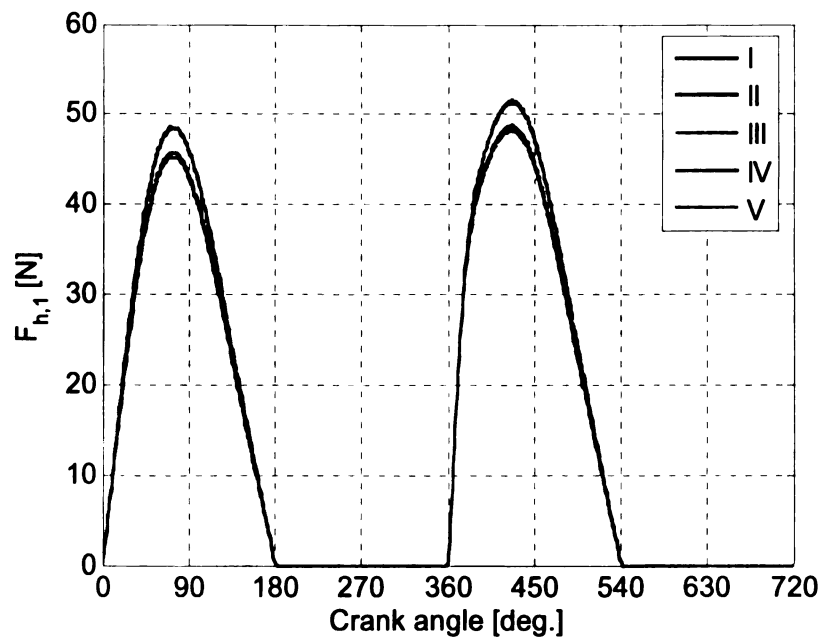


Figure 6.5: Hydrodynamic force on thrust side for meshes of Table 6.5

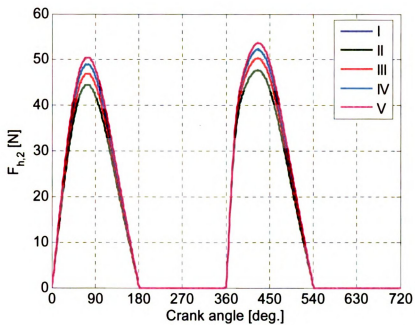


Figure 6.6: Hydrodynamic force on anti-thrust side for meshes of Table 6.5

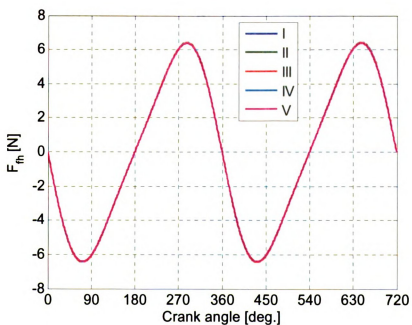


Figure 6.7: Total hydrodynamic friction force for meshes of Table 6.5

6.5 Periodicity and convergence

As an initial guess for the hydrodynamic pressure is required to start the simulation, it is evident that the solution after one cycle will not represent the actual one. Consequently the simulation needs to be run for more than one cycle until the solution is periodic. It has been observed for all the cases tested, that periodicity occurs after the second cycle. This can be seen in Figure 6.8 and Figure 6.9 where the total hydrodynamic force on the piston is shown for the first three cycles for a piston-to-bore clearance of 100 μm and 50 μm respectively.

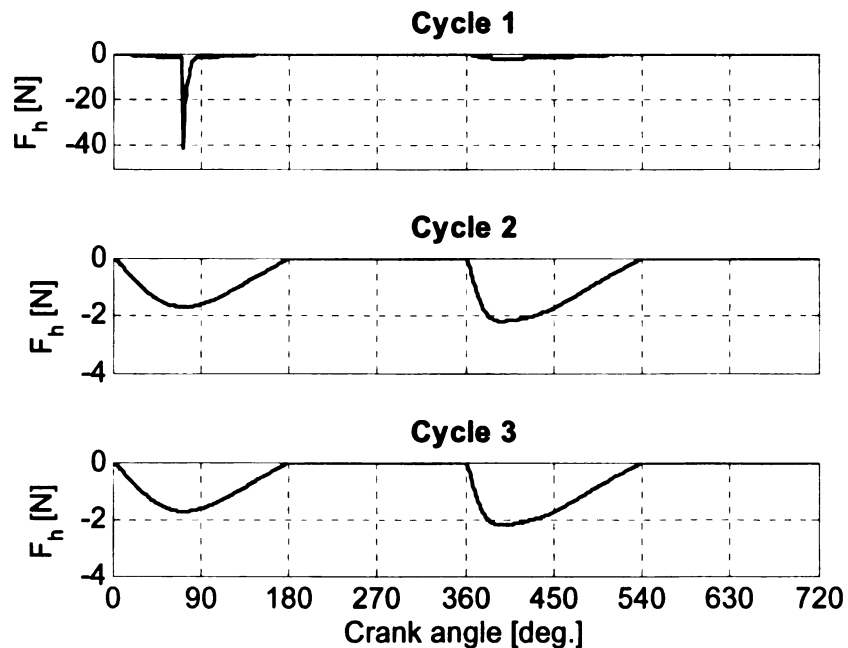


Figure 6.8: Hydrodynamic force over three cycles, $C = 100 \mu\text{m}$

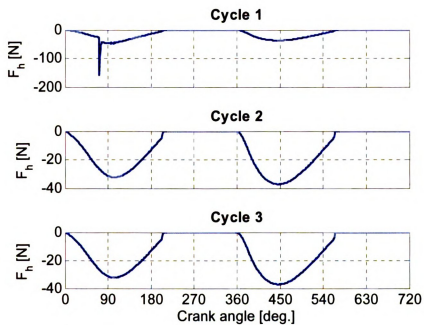


Figure 6.9: Hydrodynamic force over three cycles, $C = 50 \mu\text{m}$

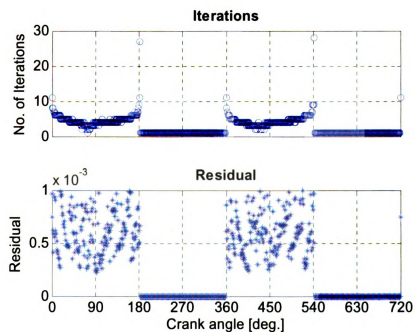


Figure 6.10: Hydrodynamic pressure convergence at 3rd cycle, $C = 100 \mu\text{m}$

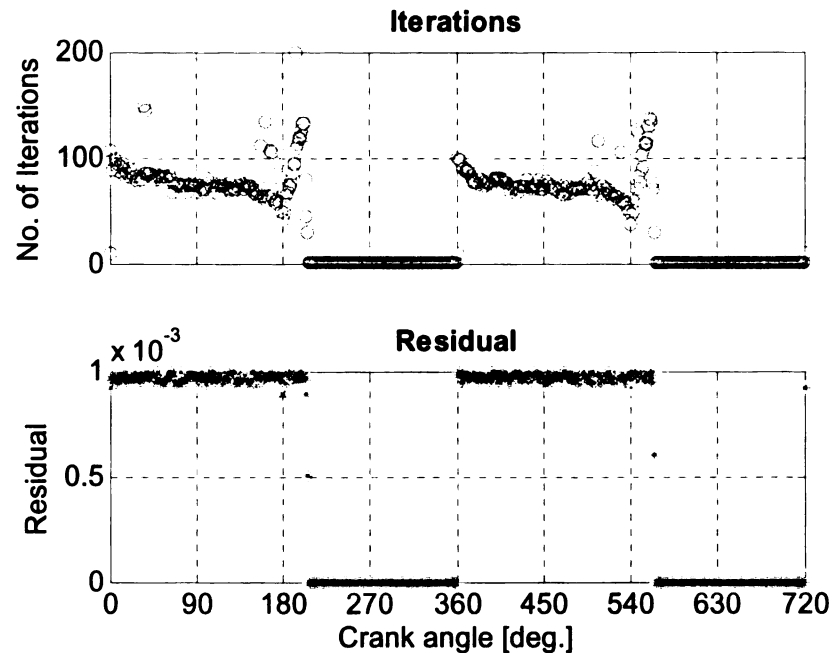


Figure 6.11: Hydrodynamic pressure convergence at 3rd cycle, $C = 50 \mu\text{m}$

Figure 6.10 and Figure 6.11 show the convergence of pressure. The number of iterations required and the residual are shown for clearance of $100 \mu\text{m}$ and $50 \mu\text{m}$. For a tolerance of 10^{-3} , the hydrodynamic pressure for the case of $50 \mu\text{m}$ converges about ten times slower than the $100 \mu\text{m}$ clearance case.

6.6 Simulation Results

In the interest of space not all simulation results can be shown here. Appendix B shows all the outputs of $\pi\text{-fea}$ for one crank angle for the simulation with clearance of $100 \mu\text{m}$. The chosen crank angle is at 365 degrees where the combustion gas pressure is still relatively high, and the motion of the piston allows for the buildup of hydrodynamic lubrication pressure. Some selected results are discussed below.

6.6.1 Temperature

Figure 6.12 shows the temperature distribution of the piston. As discussed earlier, given sufficient operating time of the engine, the piston is assumed to be at steady state over the cycle as temperature fluctuations occur on the outer layer of the piston about 2 mm thick. As expected the temperature is higher on the crown because of the combustion gases, and it decreases moving towards the bottom of the skirt. Most of the heat is lost at the ring-pack area where the heat transfer coefficient is highest.

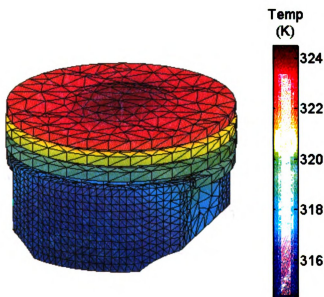


Figure 6.12: Temperature distribution

6.6.2 Deformation

Figure 6.13 shows the x -component of the piston deformation at 405 degrees for both 100 μm and 50 μm of clearance. It can be seen that the latter clearance causes a higher pressure buildup, which pushes the piston skirt more towards the piston center axis (Figure 6.13b) than the 100 μm clearance, (Figure 6.13a).

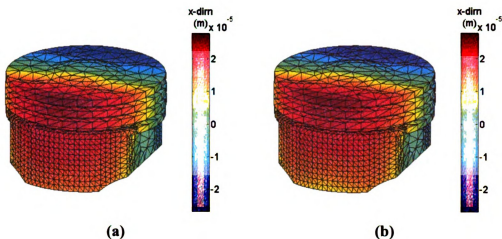


Figure 6.13: Deformation at 405 deg.: x-component, (a) $C = 100 \mu\text{m}$, (b) $C = 50 \mu\text{m}$

6.6.3 Strain

Figure 6.14 shows the equivalent strain at 405 degrees for the clearance of 100 μm . The whole piston is in the low range up to 300 microns. The high strain occurs around the pinhole. This is because the restraint for the static finite element analysis is put at the pinhole. The nodes there cannot move relative to their neighboring ones. Thus a high strain arises at that area.

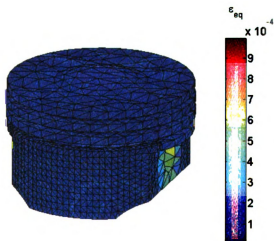


Figure 6.14: Equivalent strain at 405 deg., $C = 100 \mu\text{m}$

6.6.4 Stress

Since the stress is a function of strain, the area with high stress is around the pinhole (Figure 6.15). Considering the maximum distortion energy theory and applying the 3D von Mises yield criterion [53] to the piston (Figure 6.16), it can be seen that a few nodes fall outside the cylinder. (The radius of the cylinder is defined by the yield strength of the material.) According to the von Mises criterion failure would occur at the pinhole, however in real operating conditions the pinhole surface slides on the piston pin.

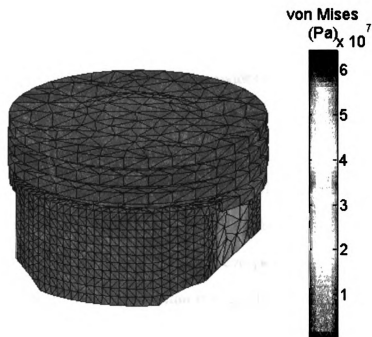


Figure 6.15: von Mises stress at 405 deg., $C = 100 \mu\text{m}$

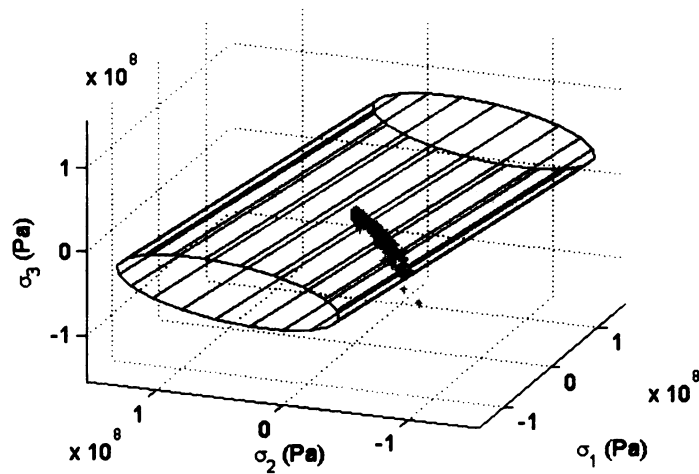


Figure 6.16: 3D von Mises yield criterion at 405 deg., $C = 100 \mu\text{m}$

6.6.5 Lubrication Pressure

Lubrication or hydrodynamic pressure provides support for the piston within the cylinder. Very high pressures are undesirable as they can deform the flexible piston skirt, and also sharp pressure gradients will increase friction. In this section the lubrication pressure as calculated by Eq. (2.114) is shown at two different crank angles, 315 degrees, mid-stroke of compression, and 405 degrees, mid-stroke of expansion. At 315 degrees (Figure 6.17 and Figure 6.18) the pressure is zero everywhere on the skirt. In the absence of piston secondary motion the squeeze film is negligible, thus the physical wedge term of the Reynolds equation dominates. However the velocity of the piston here is negative causing a positive relative velocity, Eq. (2.115), and thus a negative pressure, where with the application of the half-Sommerfeld condition it goes to zero. The opposite effect is seen at 405 degrees where the velocity of the piston is positive.

Comparing Figure 6.19 and Figure 6.20 with Figure 6.21 and Figure 6.22 respectively, it can be seen that halving the clearance creates a pressure about one order of magnitude higher.

A study of these pressure profiles over a cycle can help improve piston design and thus piston performance.

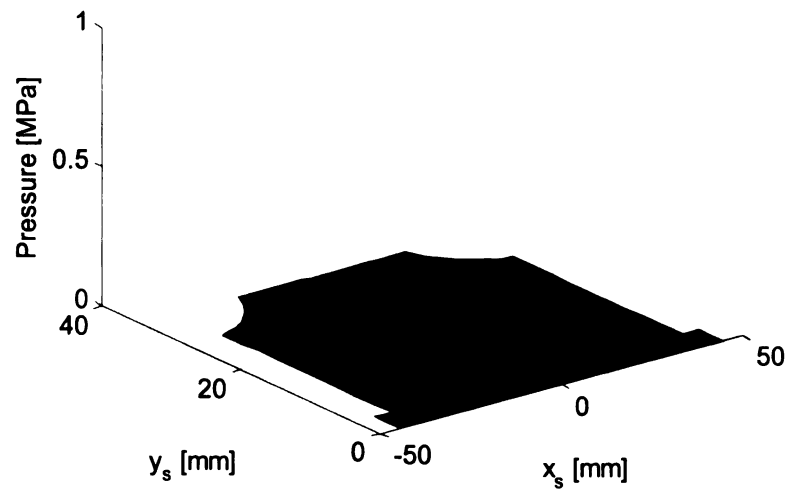


Figure 6.17: Hydrodynamic pressure on thrust side at 315 deg., $C = 100 \mu\text{m}$

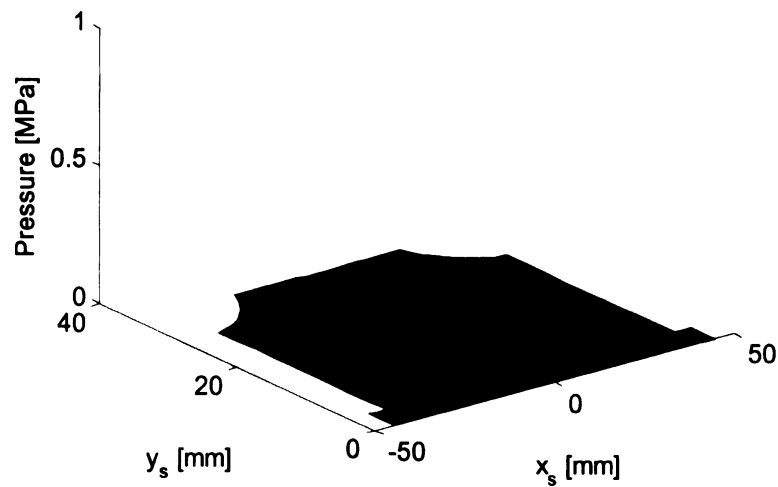


Figure 6.18: Hydrodynamic pressure on anti-thrust side at 315 deg., $C = 100 \mu\text{m}$

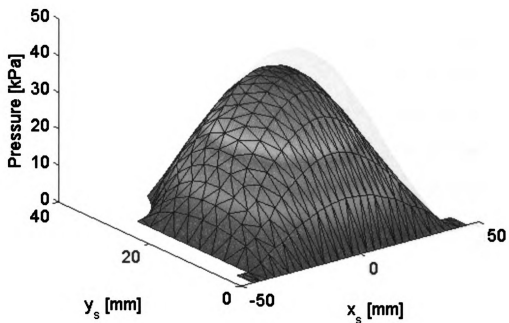


Figure 6.19: Hydrodynamic pressure on thrust side at 405 deg., $C = 100 \mu\text{m}$

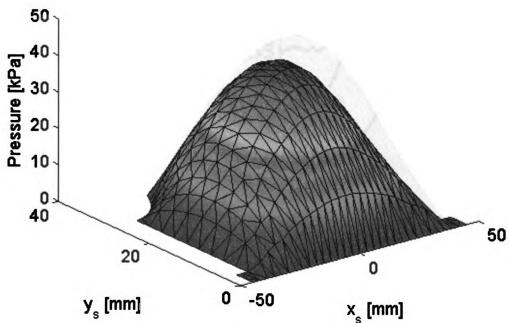


Figure 6.20: Hydrodynamic pressure on anti-thrust side at 405 deg., $C = 100 \mu\text{m}$

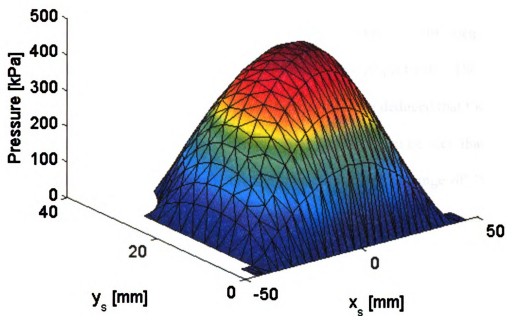


Figure 6.21: Hydrodynamic pressure on thrust side at 405 deg., $C = 50 \mu\text{m}$

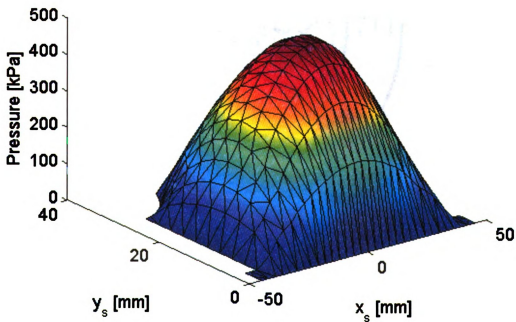


Figure 6.22: Hydrodynamic pressure on thrust side at 405 deg., $C = 50 \mu\text{m}$

6.6.6 Oil Film Thickness

Figure 6.23 and Figure 6.24 show the oil film thickness at 405 degrees for the clearance of 100 μm for the thrust and anti-thrust sides respectively. The simulation assumes fully flooded lubrication. From these figures it can be deduced that the flexibility of the skirt increases moving towards the bottom of it. Also it can be seen that the piston has suffered thermal expansion as the oil film thickness is in the range of 75 μm to 90 μm . Similar trends are observed at all crank angles.

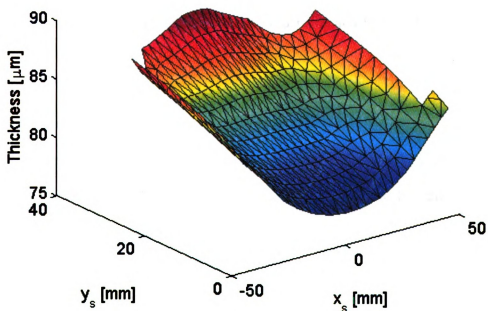


Figure 6.23: Oil film thickness on thrust side at 405 deg., $C = 100 \mu\text{m}$

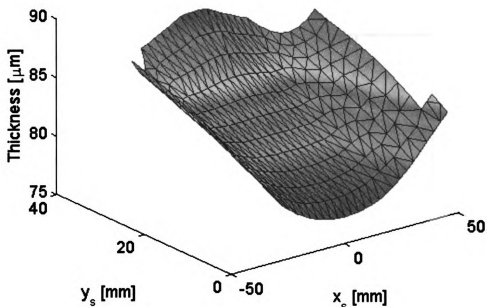


Figure 6.24: Oil film thickness on anti-thrust side at 405 deg., $C = 100 \mu\text{m}$

6.6.7 Forces and Moments

Figure 6.25 shows the total hydrodynamic force experienced by the piston over a cycle for both clearances, $100 \mu\text{m}$ and $50 \mu\text{m}$. As expected, the low clearance creates much higher force. The hydrodynamic force, Eq. (5.16), is negative for both cases, implying that the hydrodynamic force on the anti-thrust is higher. This is caused from the thermal strains in conjunction with the pin offset. As described earlier, the pin offset is towards the thrust side. Splitting the piston by a plane perpendicular to the pinhole axis and coincident with the piston center axis (Figure 6.26), the anti-thrust side half has slightly higher material volume. This allows for a higher thermal expansion on the anti-thrust side half, as the pinhole is restrained and thermal expansion occurs radially away from the pinhole.

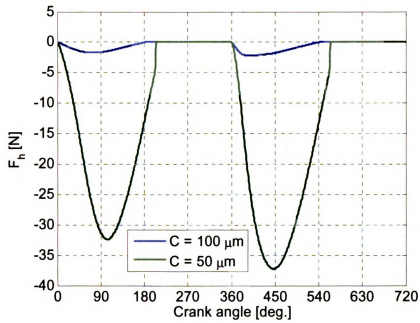


Figure 6.25: Total hydrodynamic force on piston

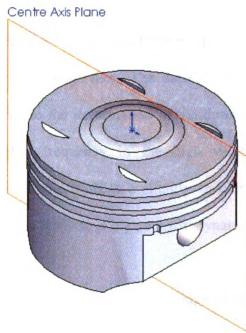


Figure 6.26: Plane parallel to pinhole axis and coincident with piston axis

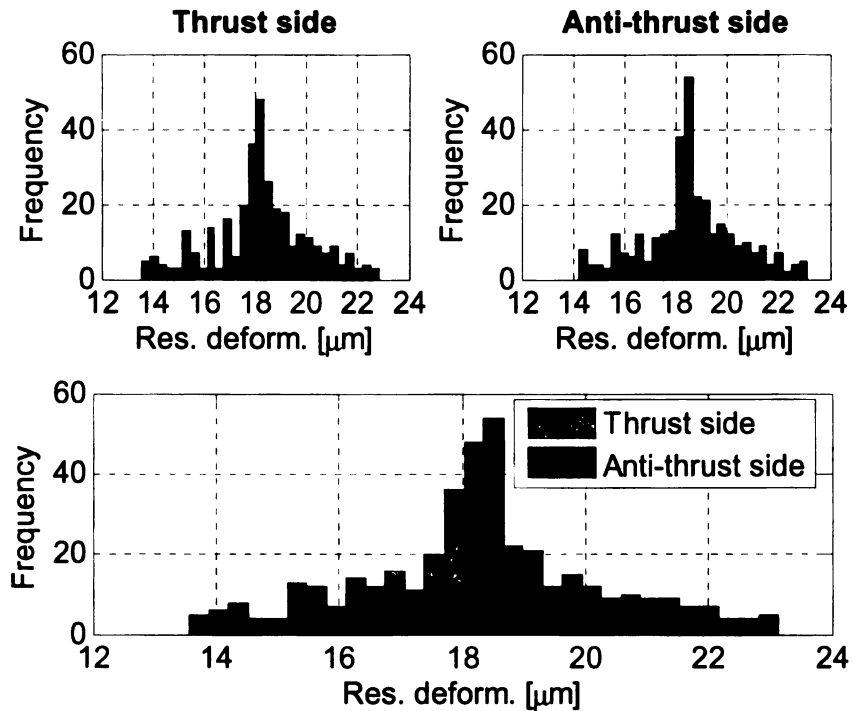


Figure 6.27: Histogram of resultant deformation on thrust and anti-thrust side due to thermal expansion only

Figure 6.27 considers the histograms of the resultant deformation on thrust and anti-thrust sides due to thermal expansion. The deformation of the anti-thrust side is shifted to the right compared to the deformation of the thrust side. Also the anti-thrust side deformation has higher frequency in the high values. This slightly higher deformation on the anti-thrust side leads to a slightly smaller gap and consequently a higher pressure buildup, which leads to a higher hydrodynamic force on the anti-thrust side.

Also it can be seen from Figure 6.25 that the high clearance creates a force only during the intake and expansion strokes. This is not the case for the low clearance. It creates a force for a few degrees after the beginning of the compression stroke as well as of the exhaust stroke. This happens because of the squeeze film effect (second term on

the right hand side of Reynolds equation). The high pressures have created enough deformation on the flexible skirt during the down-strokes, that at the beginning of the two up-strokes where the physical wedge has no effect, the squeeze film builds up pressure, as the piston skirt relaxes.

Figure 6.28 shows the total contact force. For these two cases no contact force occurs. This is expected in the absence of piston secondary motion, unless the piston experiences extremely high temperatures that will cause very high thermal expansion.

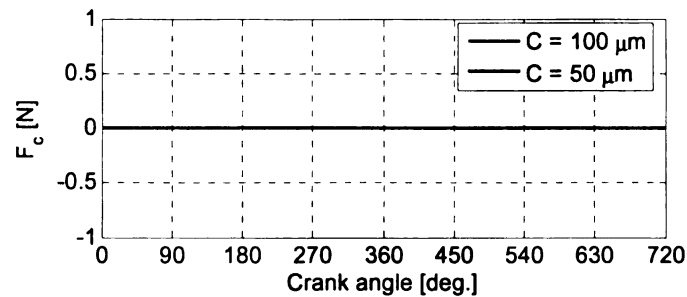


Figure 6.28: Total contact force on piston

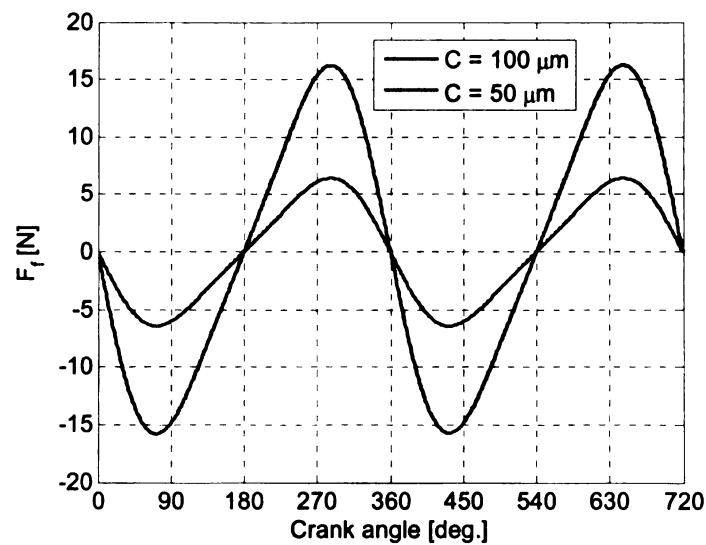


Figure 6.29: Total friction force on piston

Figure 6.29 shows the total friction force on the piston, Eq. (5.32). The low clearance causes a higher friction, as expected. It is evident from the figure that the piston velocity term dominates the value of friction. The friction profile looks like an inverted piston velocity profile (Figure 3.5), but of different magnitude. Lubrication pressure gradient has little effect on friction.

Figure 6.30 shows the total moment, Eq. (5.33), experienced by the piston. The moment is relatively small for both cases, as it depends on the piston skirt centroid relative to the pinhole center. Comparing the two, the low clearance creates a much higher moment on the piston.

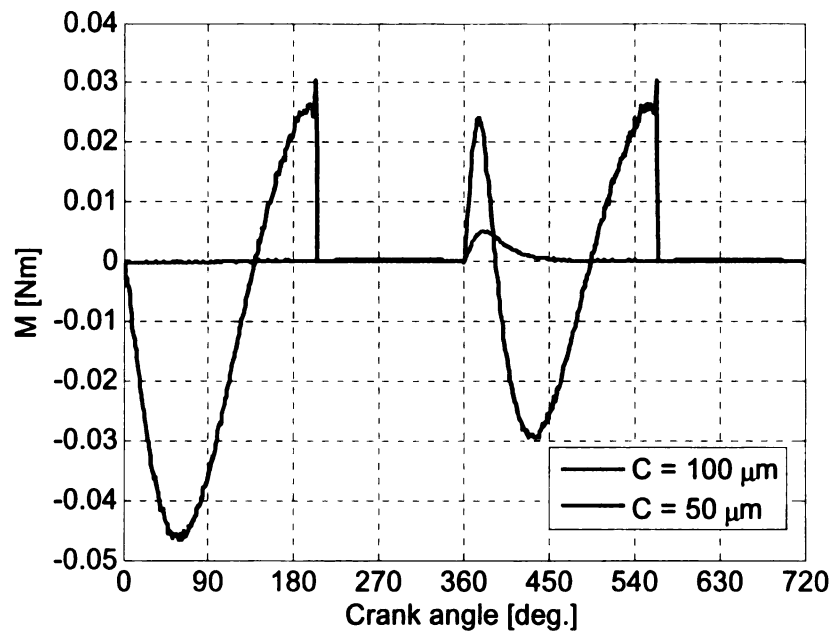


Figure 6.30: Total moment on piston

CHAPTER 7

CONCLUSIONS AND RECOMMENDATIONS

7.1 Conclusions

In this thesis two studies were conducted: an evaluation of the parameterized piston modeling method and development of a finite element program for the full piston model analysis.

The first study has demonstrated the advantage of using a parameterized piston model for evaluating the piston characteristics, elastohydrodynamic lubrication, dynamics, and friction. A careful parameterization of the full piston model lead to a reduced model which provided reasonable simulation results, with a significant reduction in computation time.

Parameterized piston analysis can be used as a guideline for optimal piston design. Optimization can be done on the parameterized piston automatically where design characteristics such as the skirt profile, the pin location, and the piston ovality can be varied to reconstruct a new model without the need of external solid modeling software. Computational time constraints would prohibit automatic optimization using a very detailed FE model.

Another advantage of the parameterized piston method is that it requires minimal FEM knowledge from the end user. The mesh is generated automatically. Also the convective boundary conditions, the pressure loads, the body load, and the restraints are applied automatically. Setting up a full model for a FE analysis can be a tedious job as

boundary conditions have to be applied to faces. For the piston presented in Chapter 4 the full model has 782 faces whereas the parameterized model only 29.

The piston skirt has a strong influence on piston performance, such as lubrication, dynamics and friction. It has been shown here that the parameterized piston demonstrates a qualitative good agreement with the full model at the skirt area. Under thermal loading they both deform away from the piston axis. Under mechanical loading they both deform towards the piston center axis. Under the combined effect of mechanical and thermal loading, they both deform away from the piston center axis.

There is a very good agreement between the effects of mechanical loading on the two models, both qualitatively and quantitatively. The qualitative agreement is maintained under the non-uniform skirt loading conditions. When the thermal expansion is combined with the mechanical loading, the deformation results exhibit more of qualitative agreement than quantitative. This disagreement on nodal deformation is caused by the thermal expansion. As the parameterized model has a smaller volume, 125505 mm^3 , compared to the full model, 130833 mm^3 , its thermal expansion is less than the full piston model. In the thermal analysis the piston is assumed to be at steady state over the entire cycle, the in-cylinder air temperature is averaged, and mean values are chosen for the heat transfer coefficients. Considering these assumptions the discrepancy caused by the thermal expansion can be considered acceptable. The goal to obtain the general behavior of the piston under both thermal loading and mechanical loading was achieved here.

In the CASE analysis the deformation due to in-cylinder gas pressure, lubrication pressure, and body load is evaluated at every crank angle. In this case the parameterized

piston demonstrates the same behavior as the full model. Thus the simulated characteristics, like skirt profile and piston pin offset, are considered reasonable and can be applied to the full model.

The second study has concentrated on the development of a finite element program, specially tailored to conduct a piston analysis over a full four-stroke cycle. The program couples heat transfer, solid mechanics, fluid mechanics and tribology under the umbrella of finite elements. The program is able to import the meshed geometry of a piston and perform a full cyclic piston analysis to predict the piston's temperature distribution, deformation, strains, and stresses. It also predicts skirt lubrication pressures, oil film thicknesses, and forces and moments.

All these results are not typical of a piston at real operating conditions. A major assumption was made, that the piston is moving along the center of the cylinder bore with no freedom to move transversely or tilt. Also lubricant viscosity was assumed to be constant along the length of the cylinder bore, and the cylinder bore was assumed rigid. Despite these assumptions some insights were obtained for the piston modeling approach and its behavior over a cycle.

The mesh size plays an important role in the accuracy of predicted results. Although linear tetrahedral elements were used, their size can be controlled to minimize error. For the assessment of the flexible skirt characteristics (forces and moments), a mesh size of 2.5 mm would be adequate as the difference from the 2 mm element size is very small. In the interest of computation time and since this was a demonstrative simulation an element size of 3 mm was chosen for the skirt area. The rest of the piston

can be meshed with a bigger element size as no crucial information is extracted from it consequently saving on computation time.

The internal combustion engine is a cyclic device. Thus a cyclic behavior is expected for the predicted parameters. As piston modeling is treated as an initial value problem, guessing an initial lubrication pressure, the simulation needs to be run for more than one cycle to fade out the error caused by the initial guess. It has been observed that cyclic behavior occurs after the second cycle. Thus a simulation needs to be run for at least two cycles for the predicted results to be considered valid.

Convergence of hydrodynamic pressure is directly affected by the nominal piston to cylinder bore clearance. As the clearance decreases, the pressure requires more iterations to converge. For all the cases studied the pressure never failed to converge. For some crank angles though, this required up to 200 iterations.

A small clearance creates a higher pressure, as expected. In such a case the piston skirt experiences less deformation. A small clearance, however, creates higher friction, which is undesirable. At this stage, in the absence of secondary piston motion, no conclusion can be made for the clearance size. From other efforts it has been shown that a high clearance causes piston slap, and a too small clearance high friction. Consequently there is a tradeoff between the two, as the hydrodynamic pressure is the one that supports the piston within the cylinder bore.

The simulations predict that the area around the pinhole is the most highly stressed area of the piston. The von Mises yield criterion even predicts failure at that area. However, in real operating conditions, this prediction does not hold as the pinhole area is

not restrained but slides on the piston pin. For the simulation it has to be restrained to provide sufficient boundary conditions for the solution of the static problem.

Finally it has been predicted that the piston pin offset affects lubrication pressure and thus hydrodynamic force. Due to the offset the skirt face furthest from the pinhole, in this case the anti-thrust side, experiences higher thermal expansion, creating a smaller gap and thus building up a higher pressure.

7.2 Recommendations

The parameterized piston model achieves its goal. It predicts the piston's general behavior under the studied loads. The parameterized model can be improved by incorporating the ring grooves, consequently bringing it closer to the full piston model.

π -fea can currently predict a majority of the parameters affecting piston performance. However, it needs further development before it can be confidently used in a real simulation. The present developments form the backbone of a reliable piston modeling program.

Secondary piston motion should be included in the program. The equations of secondary motion of the piston and the equations of motion of the connecting rod should be coupled with the deformation results and the Reynolds equation to predict piston secondary motion within the cylinder bore.

Also, an algorithm should be developed to monitor the position of the piston land areas, the areas between the ring grooves,. In the case of contact of any land with the cylinder bore, the secondary piston dynamics would be altered.

The Reynolds equation also needs improvement. The modified Reynolds equation developed by Patir and Cheng (1978) should be used to account for the effects of surface texture on hydrodynamic lubrication.

The half-Sommerfeld boundary condition for the hydrodynamic pressure used in this model violates mass conservation. The cavitation algorithm [17] should be used instead. It solves for the Reynolds equation for density variations and then calculates pressure, in the meantime accounting for mass conservation.

The asperity contact model should be improved as well. Currently the formula developed by Zhu et al. [59] for the contact of an aluminum piston with a cast iron cylinder bore is used. This limits the model to just these two materials. The Greenwood-Tripp model [19], which accounts for the contact of two nominally flat rough surfaces, is recommended.

A flexible cylinder bore should also be included in the model, as in real operating conditions the combustion gas pressure, lubrication pressure, and temperature gradients deform the cylinder bore. Finally the lubricant viscosity should be modeled to vary with temperature as this is the case with conventional lubricants. The cylinder bore is at different temperatures along its length as well as the piston skirt. These affect the lubricant viscosity in real operating conditions.

In conclusion, the parameterized piston model demonstrates a similar thermal and mechanical behavior as the full piston model. The *π -fea* program can import the meshed geometry of a full piston model and perform an analysis over a four-stroke cycle to predict piston deformation, strains and stresses, as well as hydrodynamic and contact forces.

APPENDIX A

APPENDIX A

FLOWCHARTS OF THE π -*fea* PROGRAM AND OF ITS SUBROUTINES

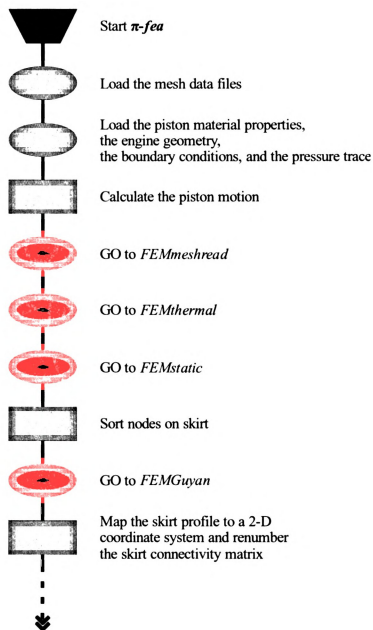


Figure A.1: Flow chart for the main program of π -*fea* (Part 1 of 2)

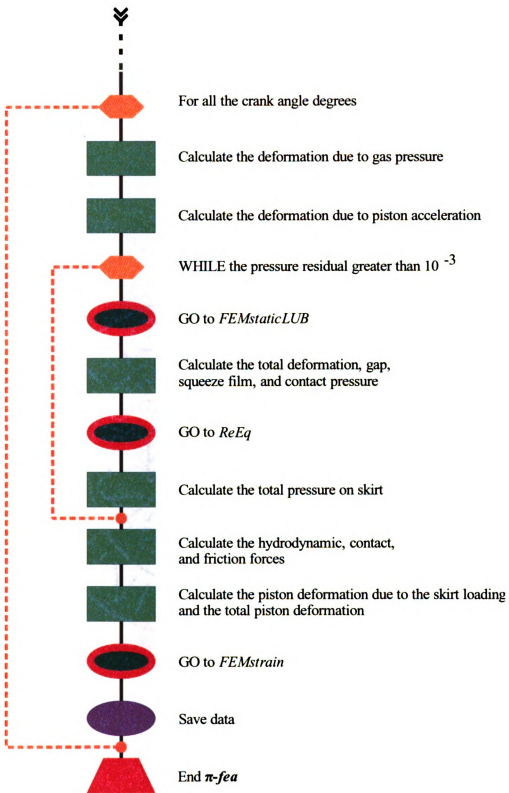


Figure A.2: Flow chart for the main program of *pi-fea* (Part 2 of 2)

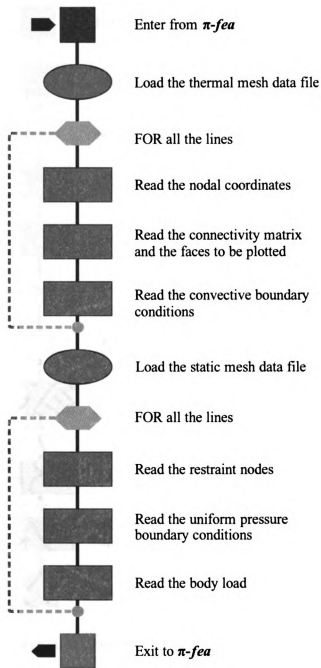


Figure A.3: Flowchart for *FEMmeshread* subroutine

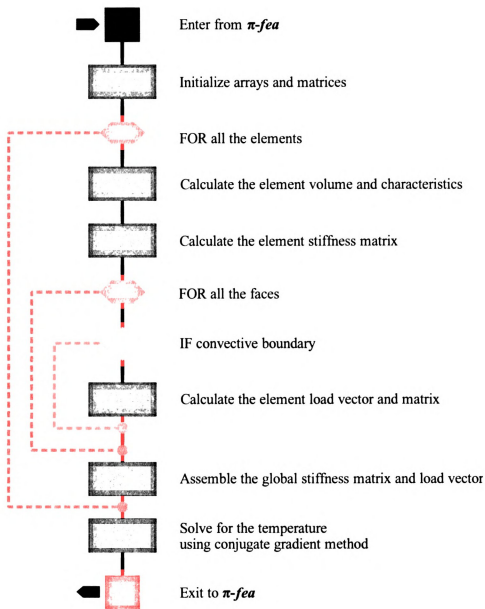


Figure A.4: Flowchart for *FEMthermal* subroutine

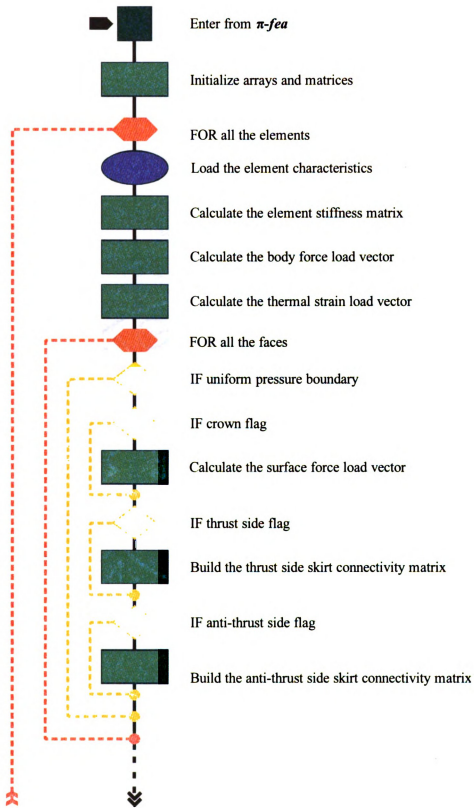


Figure A.5: Flowchart for *FEMstatic* subroutine (Part 1 of 2)

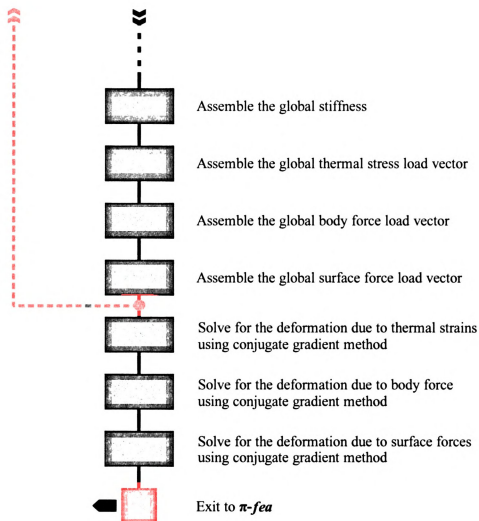


Figure A.6: Flowchart for *FEMstatic* subroutine (Part 2 of 2)

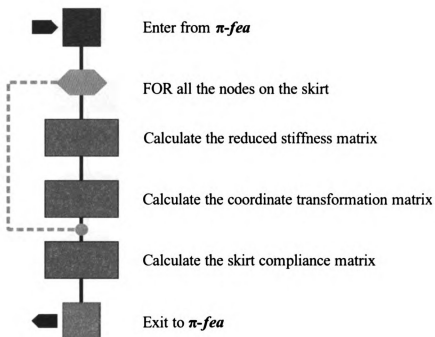


Figure A.7: Flowchart for *FEMGuyan* subroutine

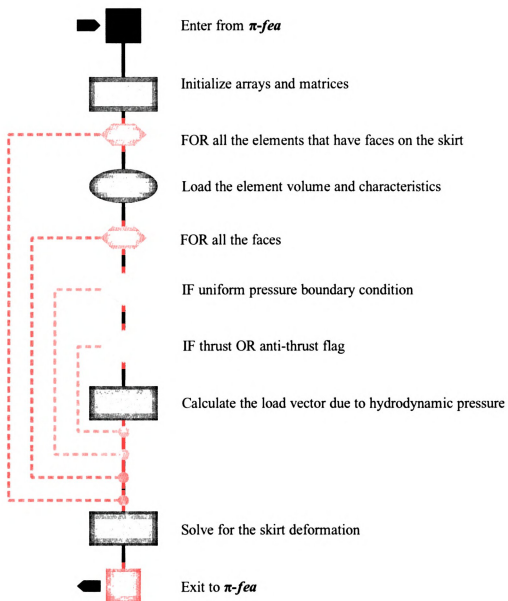


Figure A.8: Flowchart for *FEMstaticLUB* subroutine

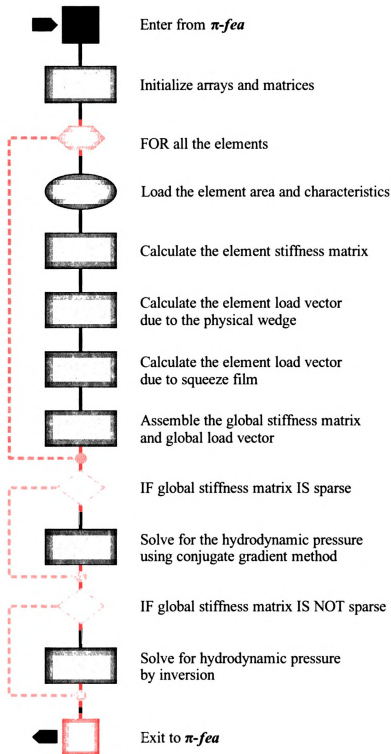


Figure A.9: Flowchart for *ReEq* subroutine

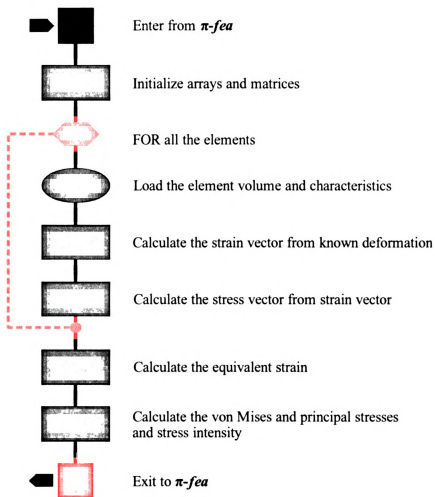


Figure A.10: Flowchart for *FEMstrain* subroutine

APPENDIX B

APPENDIX B

SIMULATION RESULTS

The simulation results shown in this appendix are for the engine and piston described in Chapter 6. All the results shown are at 365 crank angle degrees, 5 degrees after the expansion stroke. This crank angle was chosen because the combustion gas pressure is still very high and the motion of the piston allows for hydrodynamic pressure to be built. All these results are available for each crank angle, which make it feasible to create animations to visualize piston deformation, stress, lubrication pressure or oil film thickness over a cycle.

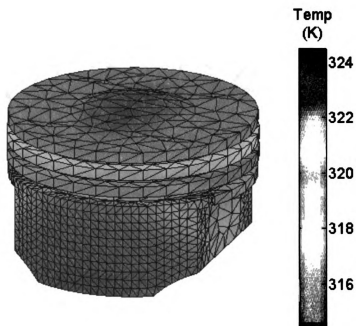


Figure B.1: Temperature distribution

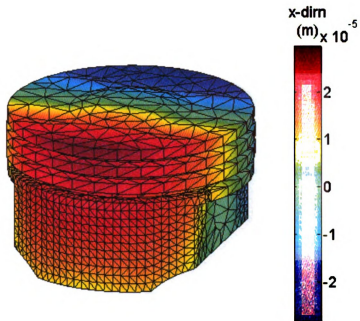


Figure B.2: Deformation: x-component

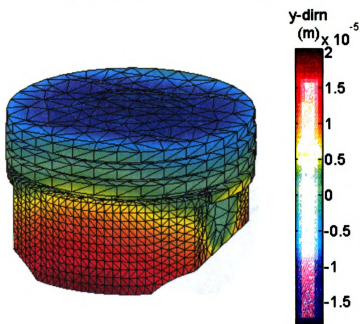


Figure B.3: Deformation: y-component

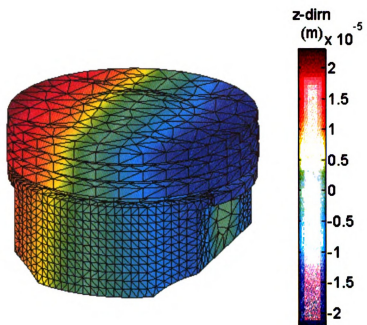


Figure B.4: Deformation: z-component

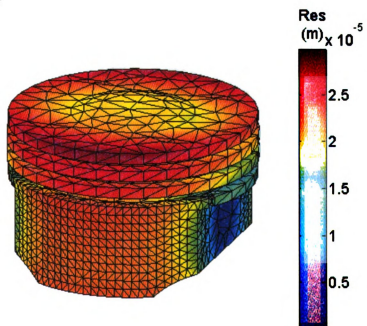


Figure B.5: Deformation: resultant

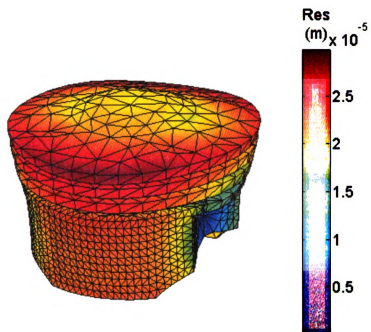


Figure B.6: Deformation: resultant, scale 1:800

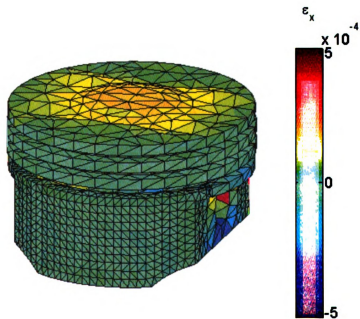


Figure B.7: Normal strain: x-component

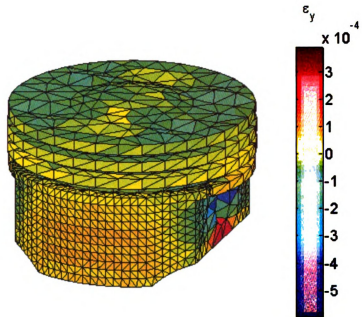


Figure B.8: Normal strain: y-component

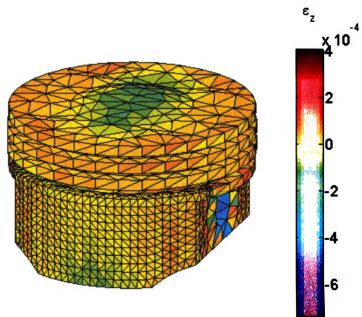


Figure B.9: Normal strain: z-component

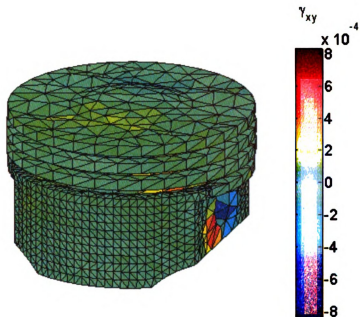


Figure B.10: Shear strain: xy -component

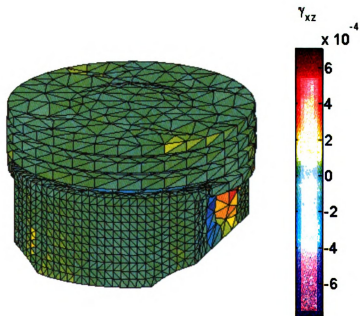


Figure B.11: Shear strain: xz -component

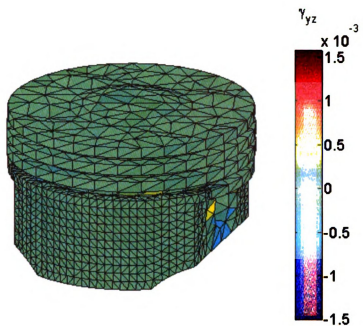


Figure B.12: Shear strain: yz-component

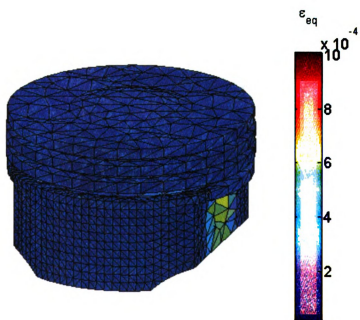


Figure B.13: Equivalent strain

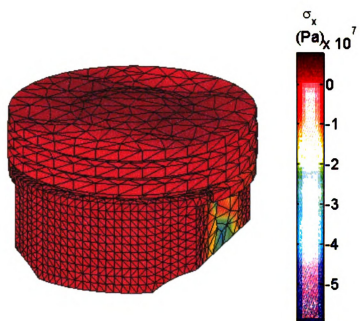


Figure B.14: Normal stress: x-component

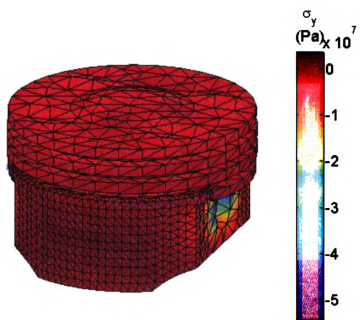


Figure B.15: Normal stress: y-component

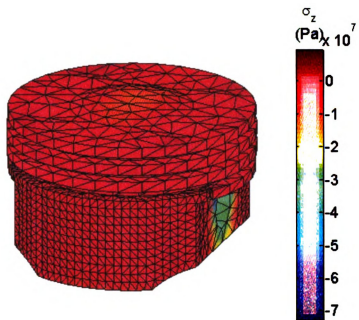


Figure B.16: Normal stress: z-component

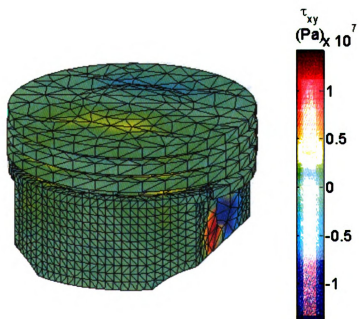


Figure B.17: Shear stress: xy-component

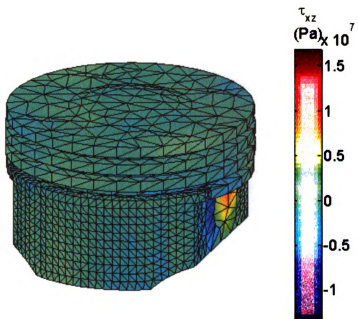


Figure B.18: Shear stress: xz-component

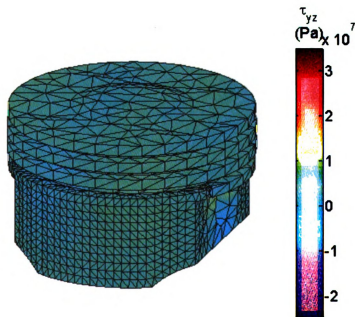


Figure B.19: Shear stress: yz-component

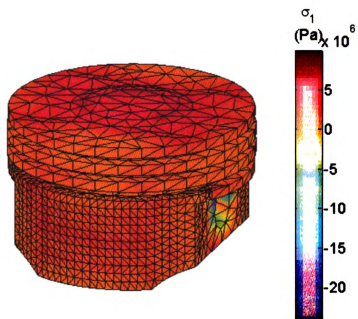


Figure B.20: Principle stress: 1st principal direction

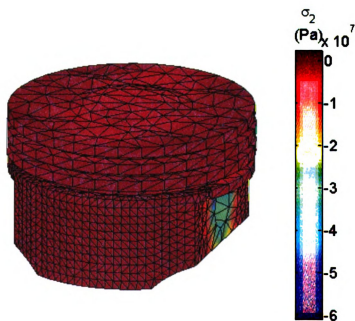


Figure B.21: Principle stress: 2nd principal direction

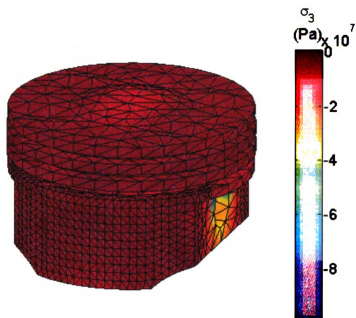


Figure B.22: Principle stress: 3rd principal direction

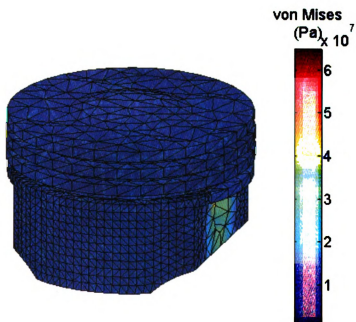


Figure B.23: von Mises stress

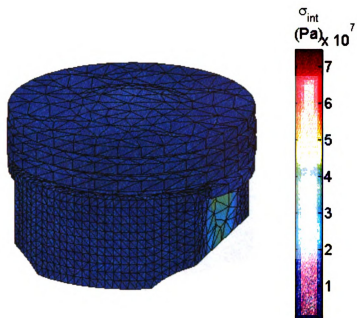


Figure B.24: Stress intensity

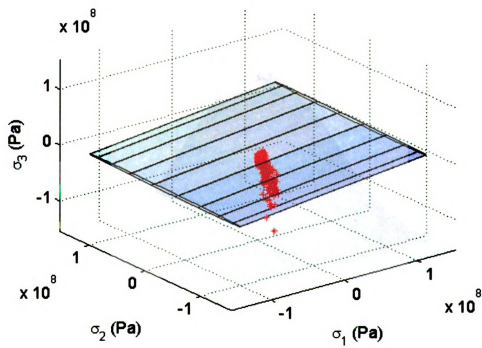


Figure B.25: 3D von Mises yield criterion

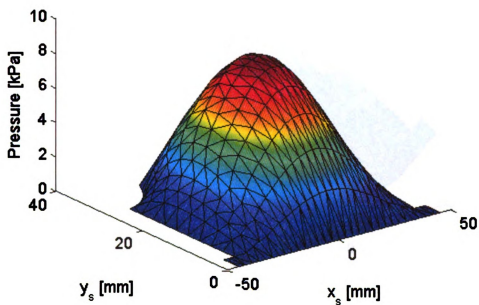


Figure B.26: Hydrodynamic pressure: thrust side

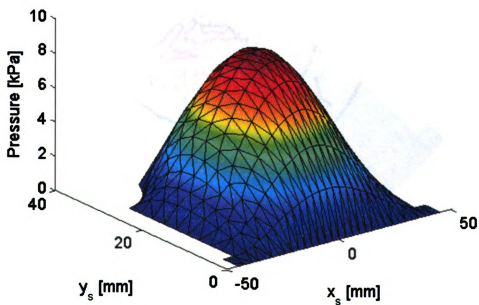


Figure B.27: Hydrodynamic pressure: anti-thrust side

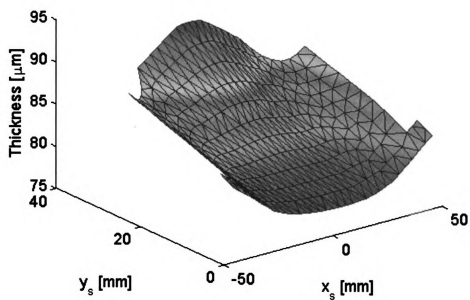


Figure B.28: Oil film thickness: thrust side

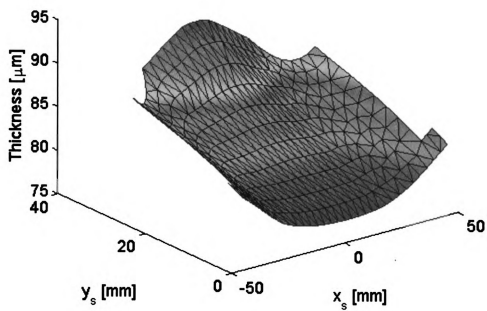


Figure B.29: Oil film thickness: anti-thrust side

REFERENCES

REFERENCES

1. Annand, W. J. D., 1963, "Heat Transfer in the Cylinders of Reciprocating Internal Combustion Engines," *Proceedings of the Institution of Mechanical Engineers*, Vol. 177, pp. 973-990.
2. Beer, F. P., Johnston, R. E., DeWolf, J. T., *Mechanics of Materials*, McGraw-Hill Higher Education, New York, 2002.
3. Bejan, A., *Advanced Engineering Thermodynamics*, John Wiley & Sons, Inc., 1997.
4. CASE Theoretical Manual, 2005, Mid Michigan Research, Okemos, Michigan.
5. Cheney, W., Kincaid, D., *Numerical Mathematics and Computing*, Brooks/Cole Publishing Company, New York, 1999.
6. Chui, B.K., Schock, H.J., 2002, "Computational Analysis of Piston-Ring Wear and Oil Consumption for An Internal Combustion Engine," ASME *ICE*, Paper No.: ICEF2002-529.
7. Chui, B.K., Schock, H.J., Fedewa, A.M., Richardson, D.E., Shaw, T., 2005, "Coupled Model of Partially Flooded Lubrication and Oil Vaporization in an Internal Combustion Engine", ASME *ICE*, Paper No.: ICES2005-1077.
8. COSMOSM 2.95 Electronic Documentation, Structural Research and Analysis Corporation, 2005.
9. Dursunkaya, Z., Keribar, R., 1992, "Simulation of Secondary Dynamics of Articulated and Conventional Piston Assemblies," SAE Paper 920484.
10. Dursunkaya, Z., Keribar, R., Ganapathy, V., 1994, "A Model of Piston Secondary Motion and Elastohydrodynamic Skirt Lubrication," *Journal of Tribology*, Vol. 116, pp. 777-785.
11. Duyar, M., Bell, D., Perchanok, M., 2005, "A Comprehensive Piston Skirt Lubrication Model Using a Mass Conserving EHL Algorithm," SAE Paper 2005-01-1640.
12. Ejakov, M.A., 2001, "Modeling of Axial and Circumferential Ring Pack Lubrication," ASME *ICE*, Paper No.: 2001-ICE-433.
13. Ejakov, M.A., Diaz, A.R., and Schock, H.J., 1999, "Numerical Optimization of Ring-Pack Behavior," SAE Paper 1999-01-1521.

14. Ejakov, M.A., Schock, H.J and Brombolich, L.J., 1998, "Ring Twist Modeling for an IC Engine," SAE Paper 982693.
15. Ejakov, M.A., Schock, H.J., Brombolich, L.J., Carlstrom, C.M. and Williams, R.L., 1997, "Simulation Analysis of Inter-Ring Gas Pressure and Ring Dynamics and Their Effect on Blow-by," ASME *ICE*, Paper No.: 97-ICE-50.
16. Ejakov, M.A., Yeager, D.A., and Kayupov, M., 2003, "Reliability and Robustness Analysis of Engine Ring-pack Performance," SAE Paper 2003-01-1221.
17. Elrod, H. G., 1981, "A Cavitation Algorithm," *Journal of Tribology*, Vol. 103, pp. 350-354.
18. Goenka, P. K. and Meemik, P. R., 1992, "Lubrication Analysis of Piston Skirts," SAE Paper 920490.
19. Greenwood, J. A., Tripp, J. H., 1971, "The Contact of Two Nominally Flat Rough Surfaces," *Proceedings of the Institution of Mechanical Engineers*, Vol. 185, pp. 625-633.
20. Guyan, R. J., 1965, "Reduction of Stiffness and Mass Matrices," *AIAA Journal*, Vol. 3, No. 2, p. 380.
21. Guzella, L., Onder, C. H., *Introduction to Modeling and Control of Internal Combustion Engine Systems*, Springer, New York, 2004.
22. Harrison, H. R., Nettleton, T., *Advanced Engineering Dynamics*, John Wiley & Sons, Inc., New York, 1997.
23. Heinrich, J. C., Pepper, D. W., *Intermediate Finite Element Method: Fluid Flow and Heat Transfer Applications*, Taylor & Francis, Philadelphia, 1999.
24. Herbst, M. H., Pribsch, H. H., 2000, "Simulation of Piston Ring Dynamics and Their Effect on Oil Consumption," SAE Paper 2000-01-0919.
25. Heywood, J. B., *Internal Combustion Engine Fundamentals*, McGraw Hill, Inc., New York, 1988.
26. Hibbeler, R. C., *Engineering Mechanics: Dynamics*, Prentice Hall PTR, Upper Saddle River, 2001.
27. Incropera, F. P., DeWitt, D. P., *Introduction to Heat Transfer*, John Wiley & Sons, Inc., New York, 2002.
28. Kaliakin, V. N., *Introduction to Approximate Solution Techniques, Numerical Modeling, and Finite Element Methods*, Marcel Dekker, Inc., New York, 2002.

29. Kays, W. M., *Convective Heat and Mass Transfer*, McGraw-Hill Higher Education, Boston, 2005.
30. Keribar, R., Dursunkaya, Z., 1992, "A Comprehensive Model of Piston Skirt Lubrication," SAE Paper 920483.
31. Keribar, R., Dursunkaya, Z., Ganapathy, V., 1993, "An Integrated Design Analysis Methodology to Address Piston Tribological Issues," SAE Paper 930793.
32. Khonsari, M. M., Booser, E. R., *Applied Tribology: Bearing Design and Lubrication*, John Wiley & Sons, Inc., New York, 2001.
33. Kiusalaas, J., *Numerical Methods in Engineering with MATLAB*, Cambridge University Press, Cambridge, 2005.
34. Kreyszig, E., "*Advanced Engineering Mathematics*," John Wiley & Sons, Inc., New York, 2005.
35. Li, C. H., 1982, "Piston Thermal Deformation and Friction Considerations," SAE Paper 820086.
36. Li, C. H., 1986, "Thermoelastic Behavior of an Aluminum Diesel Engine Piston," SAE Paper 860136.
37. Li, D. F., Rohde, S. M., Ezzat, H. A., 1982, "An Automotive Piston Lubrication Model," *ASLE Transactions*, Vol. 26, pp. 151-160.
38. Ludema, K. C., *Friction, Wear, Lubrication: A Textbook in Tribology*, CRC Press, Inc., New York, 1996.
39. Moran, M. J., Shapiro, H. N., *Fundamentals of Engineering Thermodynamics*, John Wiley & Sons, Inc., New York, 2004.
40. Oh, K. P., Li, C. H. and Goenka, P. K., 1987, "Elastohydrodynamic Lubrication of Piston Skirts," *Journal of Tribology*, Vol. 109, pp. 356-362.
41. Oppenheim, A. K., *Combustion in Piston Engines: Its Technology, Evolution, Diagnosis, and Control*, New York, Springer, 2004.
42. Panayi, A., Schock, H., Chui, B.K., Ejakov, M., 2006, "Parameterization and FEA Approach for the Assessment of Piston Characteristics," SAE Paper 2006-01-429.
43. Panton, R. L., *Incompressible Flow*, John Wiley & Sons, Inc., New York, 1996.

44. Pepper, D. W., Heinrich, J. C., *The Finite Element Method: Basic Concepts and Applications*, Hemisphere Publication Corp., Washington, 1992.
45. Perchanok, M., 2000, "Modeling of Piston-Cylinder Lubrication with a Flexible Skirt and Cylinder Wall," SAE Paper 2000-01-2804.
46. Pope, S. B., *Turbulent Flows*, Cambridge University Press, New York, 2000.
47. Rao, S. S., *Applied Numerical Methods for Engineers and Scientists*, Prentice Hall PTR, Upper Saddle River, 2005.
48. Rao, S. S., *The Finite Element Method in Engineering*, Butterworth-Heinemann, Boston, 1999.
49. Reddi, M. M., 1969, "Finite-Element Solution of the Incompressible Lubrication Problem," *Journal of Lubrication Technology*, Vol. 91, pp. 524-533.
50. Reddy, J. N., *An Introduction to the Finite Element Method*, McGraw-Hill, Inc., New York, 1993.
51. Reddy, J. N., Gartling, D.K., *The Finite Element Method in Heat Transfer and Fluid Dynamics*, CRC Press, Inc., Boca Raton, 1994.
52. Thompson, E. G., *Introduction to the Finite Element Method, Theory, Programming, and Applications*, John Wiley & Sons, Inc., New York, 2005.
53. Ugural, A. C., Fenster, S. K., *Advance Strength and Applied Elasticity*, Prentice Hall PTR, Englewood Cliffs, 2003.
54. Wong, V.W., Tian, T., Lang, H., Ryan, J.P., Sekiya, Y., Kobayashi, Y., Aoyama, S., 1994, "A Numerical Model of Piston Secondary Motion and Piston Slap in Partially Flooded Elastohydrodynamic Skirt Lubrication," SAE Paper 940696.
55. Woschni, G., 1967, "Universally Applicable Equation for the Instantaneous Heat Transfer Coefficient in the Internal Combustion Engine," SAE Paper 670931.
56. Woschni, G., 1979, "Determination of Local Heat Transfer Coefficients at the Piston of a High Speed Diesel Engine by Evaluation of Measured Temperature Distribution," SAE Paper 790834.
57. Wu, H., Chiu, C., 1986, "A Study of Temperature Distribution in a Diesel Piston – Comparison of Analytical and Experimental Results," SAE Paper 861278.
58. Zhu, D. Cheng, H.S., Arai, T. Hamai, K., 1992, "A Numerical Analysis for Piston Skirts in Mixed Lubrication - Part I: Basic Modeling," *Journal of Tribology*, Vol. 114, pp. 553-562.

59. Zhu, D. Hu, Y., Cheng, H.S., Arai, T., amai, K., 1993, "A Numerical Analysis for Piston Skirts in Mixed Lubrication - Part II: Deformation Considerations," *Journal of Tribology*, Vol. 115, pp. 125-133.

MICHIGAN STATE UNIVERSITY LIBRARIES



3 1293 02736 8632